Atomic layer deposition of aluminum oxide on crystalline silicon:

Fundamental interface properties and application to solar cells

von

Dipl.-Phys. Florian Werner

geboren am 27.02.1983 in Konstanz

2014

Abstract

In der vorliegenden Arbeit wird die Anwendung der Atomlagenabscheidung (*atomic layer deposition, ALD*) einer amorphen Aluminiumoxid (Al_2O_3) Schicht auf Siliziumsolarzellen untersucht. Für die neuartige und mit industriellen Anforderungen kompatible *spatial*-ALD-Methode werden ausgezeichnete Passivierergebnisse erzielt, welche mit herkömmlichen Methoden vergleichbar sind. Somit kann die Eignung dieser Technologie zur Anwendung auf zukünftige industriell gefertigte Hocheffizienz-Solarzellen belegt werden.

Erstmalig wird ein umfassendes Modell der c-Si/Al_2O_3 Grenzfläche entwickelt, welches die chemische Zusammensetzung der abgeschiedenen Schicht sowie die Rekombination an der c-Si/Al_2O_3 Grenzfläche erklärt. Die exzellente Passivierqualität kann auf eine hohe negative feste Ladungsdichte, welche sich innerhalb 1 nm von der Grenzfläche befindet, und auf eine moderate Grenzflächenzustandsdichte zurückgeführt werden. Es wird gezeigt, dass die elektrischen Eigenschaften der c-Si/Al_2O_3 Grenzfläche hauptsächlich von einer dünnen SiO_x Zwischenschicht und einer mehrere Nanometer ausgedehnten, sehr sauerstoffreichen Übergangszone zwischen SiO_x und Al_2O_3 bestimmt werden.

Eine detaillierte Analyse der Rekombination an Al_2O_3-passivierten p- und n-Typ Si Oberflächen wird vorgestellt. Drei dominante Defektzentren und deren jeweilige Rekombinationseigenschaften werden identifiziert. Eine Kombination dieser drei Defektzentren erklärt sowohl die Energieabhängigkeit der gemessenen Einfangsquerschnitte, als auch die Injektionsabhängigkeit der über einen weiten Bereich von Oberflächenladungsdichten gemessenen Rekombinationsgeschwindigkeiten sehr gut.

Ausgehend von Lebensdauermessungen, welche die bisher akzeptierte Parametrisierung der intrinsischen Lebensdauern in Silizium überschreiten, wird eine verbesserte Parametrisierung der intrinsischen Lebensdauer vorgestellt, welche die Coulomb-verstärkte Auger-Rekombination und die Coulomb-verstärkte strahlende Rekombination einschließt.

Eine durch die Ladungen im Al_2O_3 hervorgerufene Inversionsschicht

wird erstmalig als löchersammelnder Emitter in Inversionsschichtsolarzellen auf Basis von n-Typ Silizium angewandt. Es wird gezeigt, dass die Löchermobilität im Inversionskanal nahe der Siliziumoberfläche von der hohen Ladungsdichte im Al_2O_3 unbeeinflusst ist und dass der effektive Schichtwiderstand der Inversionsschicht unter Beleuchtung oder Ladungsträgerinjektion stark abnimmt. Es wird gezeigt, dass die neuartigen Al_2O_3-induzierten Inversionsschichtsolarzellen auf n-Typ Silizium unter Berücksichtigung der Rekombination an den Solarzellenkontakten Effizienzen bis zu 26.3 % und offene Klemmspannungen bis zu 735 mV erlauben. Werden Abschattungs- und Rekombinationsverluste an den Kontakten vernachlässigt, steigt das Wirkungsgradpotential auf 27.8 % und das Potential der offenen Klemmspannung auf über 780 mV.

Abstract

In the present thesis, the application of atomic layer deposition (*ALD*) of amorphous aluminum oxide (Al_2O_3) dielectric layers to silicon solar cells is investigated. A novel spatial ALD process, which is compatible with industry demands, is demonstrated to provide an excellent level of surface passivation comparable to conventional ALD techniques, and to be well suited for future generations of industrial high-efficiency silicon solar cells.

A comprehensive model of the c-Si/Al_2O_3 interface is developed for the first time, which describes the chemical composition of the deposited film and the recombination at the c-Si/Al_2O_3 interface. We identify both field-effect passivation due to a high negative fixed charge density located within $1\,nm$ of the Si/Al_2O_3 interface, and chemical passivation due to a moderate interface state density. The electrical properties of the c-Si/Al_2O_3 interface are shown to be largely dominated by a thin interfacial layer of SiO_x in combination with a highly oxygen-rich transition region between SiO_x and Al_2O_3, which extends over a depth of several nanometers.

A detailed analysis of recombination at Al_2O_3-passivated *p*- and *n*-type Si surfaces is presented. We identify three dominant defect peaks and their respective recombination parameters. A combination of these three defect types describes the energy dependence of the measured capture cross sections and the injection dependence of the measured effective surface recombination velocities over a wide range of surface charge densities very well.

Based on lifetime measurements exceeding the previously established parameterization of intrinsic lifetimes in silicon, an improved parameterization of the intrinsic lifetime of *n*- and *p*-type crystalline silicon at $300\,K$ is derived, which accounts for Coulomb-enhanced Auger recombination as well as Coulomb-enhanced radiative recombination.

An Al_2O_3-induced hole inversion layer (*IL*) is used for the first time as hole-collecting emitter in IL solar cells made on *n*-type silicon. The IL

hole mobility near the silicon surface is shown to be unaffected by the high density of fixed charges in the Al_2O_3 layers, and the effective IL sheet resistance is shown to decrease significantly under illumination or carrier injection. The novel Al_2O_3-induced IL solar cells on n-type silicon are shown to allow efficiencies up to $26.3\,\%$ and open-circuit voltages up to $735\,mV$, including contact recombination. Neglecting optical shading and recombination losses at the contacts increases the efficiency limit further to $27.8\,\%$ and the open-circuit voltage limit to above $780\,mV$.

Contents

1 Introduction

In a silicon solar cell under illumination, excess carriers are generated by the absorption of photons with energies above the silicon bandgap. Before reaching the electrical contacts of the solar cell, and hence contributing to the power generation of the solar cell, these excess carriers may recombine. In silicon, which features an *indirect* bandgap, recombination for most devices mainly occurs via defects in the silicon bulk or at the silicon surface. In order to significantly increase the solar cell power conversion efficiency further, control over the various recombination channels is indispensable. With the trend towards higher power conversion efficiencies and thinner solar cell wafers, mainly recombination due to the locally high defect density at the silicon surface poses an increasingly crucial limitation to the solar cell performance. Recombination losses at the silicon surface can be significantly reduced by the deposition of a dielectric *surface passivation layer* onto the silicon. Previously, mainly thermally grown silicon dioxide (SiO_2), and silicon nitride (SiN_x) deposited by plasma-enhanced chemical vapor deposition (*PECVD*), have been employed with great success. Thermally grown silicon dioxide provides an excellent surface passivation on all silicon surfaces due to an efficient saturation of surface defects. However, the high-temperature growth process at above $1000\,^{\circ}\mathrm{C}$ is expensive and time-consuming, and is not applicable to all solar cell processes and materials. The plasma-enhanced chemical vapor deposition of silicon nitride, where the temperature is typically in the range of $300 - 400\,^{\circ}\mathrm{C}$, avoids both of these disadvantages. Accordingly, silicon nitride has become the most widely used passivating dielectric in silicon solar cell research and industry.

Silicon nitride, however, contains positive charges, which cause several disadvantages in the passivation of *p*-type doped silicon: In conjunction with surface-near damage caused by the plasma deposition process,

these positive charges provoke a reduced surface passivation quality with reduced illumination intensity. This leads to a reduction of the power conversion efficiency in a photovoltaic module operating under realistic outdoor illumination conditions. Moreover, the electron concentration at the silicon surface is increased due to the presence of positive charges, which might lead to parasitic shunting on p-type silicon, and reduces the passivation quality of p^+-type emitters, which are required for solar cells based on n-type silicon.

Hence, especially for the industrially highly relevant topics of rear side passivation of standard screen-printed p-type silicon solar cells and the emitter passivation of highly efficient n-type silicon solar cells, no adequate low-temperature passivation scheme has been available so far. In this thesis, the atomic layer deposition (ALD) of aluminum oxide (Al_2O_3) as alternative surface passivation layer will be investigated.

Aluminum oxide as low-temperature passivation layer was already proposed in the 80's by Hezel and Jaeger [1]. Already back then the high negative fixed charge density in the Al_2O_3 layers was identified. Despite the interesting material properties, however, research towards the application of Al_2O_3 in silicon solar cells did not continue for more than two decades. In 2006, Agostinelli *et al.* [2] demonstrated a well passivating Al_2O_3 layer by means of atomic layer deposition. The surface passivation was shown to be temperature-stable and laterally homogeneous over a large area ($> 300\,cm^2$). Further research was conducted by Hoex *et al.*, who attributed the excellent passivation quality of Al_2O_3 layers to a combination of a high negative fixed charge density and a low interface defect density [3–5]. Both Agostinelli and Hoex reported that a (low-temperature) post-deposition annealing was indispensable to fully "activate" the passivation quality. Aluminum oxide layers have also been investigated intensively in the semiconductor industry as promising high-k dielectric (overview and references are given in Ref. 4). Here, the fixed charge density in the Al_2O_3 was found to be negative independent of deposition technique, as long as the Al_2O_3 layers were subjected to a

post-deposition anneal. The formation of the negative fixed charge density was suggested to be related to a thin interfacial silicon oxide layer between silicon and aluminum oxide [4].

In 2008, for the first time the excellent passivation quality of Al_2O_3 deposited by ALD was successfully applied to highly-doped p^+ emitters [6] and transfered to laboratory-type solar cells. Efficiencies of up to 20.6% were obtained for p-type solar cells with a diffused front side n^+ emitter and an Al_2O_3-based rear side passivation [7]. Using Al_2O_3 to passivate a boron-diffused p^+ emitter of an n-type solar cell resulted in an efficiency as high as 23.2% [8]. In addition, the feasibility of various deposition techniques, such as plasma-assisted and thermal atomic layer deposition (*ALD*) [2, 5, 9, 10], plasma-enhanced chemical vapor deposition (*PECVD*) [10, 11], and rf-sputtering [12], has been explored.

Within the scope of this thesis, several Al_2O_3 deposition techniques have been compared. So far the best passivation quality was obtained using ALD, where both plasma-assisted and thermal ALD led to surface recombination velocities below $10\,cm/s$ and the films were shown to be temperature stable during a typical contact firing process. The present thesis focuses on the application of atomic layer deposition of amorphous Al_2O_3 dielectric layers to silicon solar cells as well as fundamental studies on the c-Si/Al_2O_3 interface properties. **Chapter 2** describes the fundamental principle of atomic layer deposition of Al_2O_3 on crystalline silicon (*c-Si*), and fundamental properties of the deposited Al_2O_3 layers are presented. Although Al_2O_3 is an ideal choice for the rear surface passivation of silicon solar cells [7], its integration into industrial solar cells is hampered by a low throughput. Hence, the surface passivation with Al_2O_3 based on a novel spatial ALD concept, which allows significantly higher deposition rates, is investigated. We demonstrate that spatial ALD provides the means to integrate Al_2O_3 passivation layers into industrial solar cells.

Chapter 3 presents a detailed review of the theoretical description of the charge densities and potentials near the silicon surface, which is

essential for an in-depth look at the c-Si/Al$_2$O$_3$ interface. Based on the presented equations, the characterization methods employed in this thesis are introduced.

A central aim of this thesis is the development of a consistent physical model of the c-Si/Al$_2$O$_3$ interface. Furthermore, the optimization of photovoltaic devices toward higher energy conversion efficiencies profits substantially from numerical device simulations, which rely on experimental data and empirical models to quantify the relevant loss mechanisms in the device. A detailed knowledge of the energy-dependent electron-hole recombination parameters at the c-Si/Al$_2$O$_3$ interface enables highly predictive simulations of the interface recombination processes at the Al$_2$O$_3$-passivated solar cell surface, and hence would be of great benefit for the development and improvement of novel highly efficient solar cells. **Chapter 4** presents detailed studies of the structural and chemical properties of the interfacial region. Based on experimental results, a physical model for the c-Si/Al$_2$O$_3$ interface is derived, and the origin of the negative fixed charge is addressed. The energy-dependent recombination parameters at the Al$_2$O$_3$-passivated c-Si surface are presented in **Chapter 5**. Numerical simulations of the effective surface recombination velocity based on these recombination parameters show a good agreement with experimental surface recombination velocities over a wide range of excess carrier and surface charge densities.

Due to the excellent level of surface passivation provided by Al$_2$O$_3$, effective charge carrier lifetimes exceeding the intrinsic lifetime limit according to an empirical parametrization, which was widely accepted prior to this work [13], have been measured. **Chapter 6** presents a re-evaluation of Auger recombination in silicon based on the improved surface passivation provided by Al$_2$O$_3$.

An inversion layer forming at the surface of an n-type Si wafer passivated with an Al$_2$O$_3$ film offers the opportunity to avoid a boron diffusion in the fabrication of n-type solar cells, as the inversion layer may act as hole-collecting emitter in a novel n-type inversion layer solar cell. The

charge transport of holes in such a p^+ inversion layer is investigated in **Chapter 7**. The efficiency potential of Al_2O_3-based inversion layer solar cells on n-type silicon is investigated by numerical device simulations based on experimental input parameters and first proof-of-principle devices are presented.

2 Atomic layer deposition (ALD) of aluminum oxide thin films

2.1 Principle of atomic layer deposition
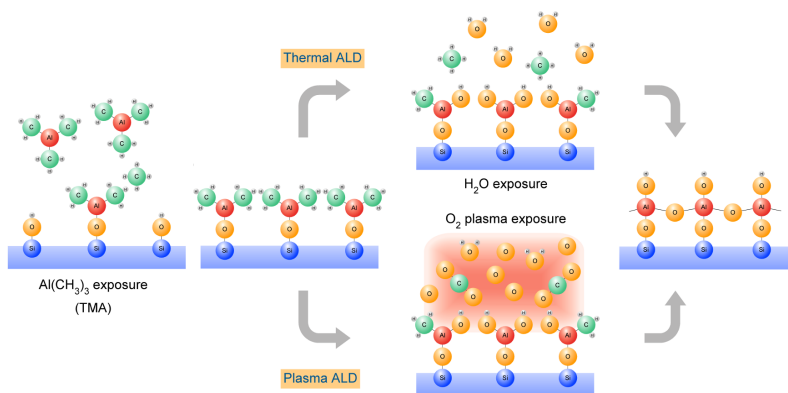
Figure 2.1: Schematic representation of one cycle of a water-based *thermal* and an oxygen-based *plasma-assisted* atomic layer deposition (ALD) process. Each cycle consists of two half-reactions: first, the trimethyl aluminium (TMA) molecules react with the hydroxyl groups attached to the silicon surface; second, the molecules are oxidized by H_2O (thermal ALD) or oxygen radicals created in an O_2 plasma (plasma ALD).

In the atomic layer deposition (ALD) [14] of Al_2O_3, a highly conformal and pin-hole free monolayer-by-monolayer coating is achieved by two alternating self-limiting half-reactions of the precursor molecules. One monolayer of Al_2O_3 grows during each cycle, and cycles are repeated until the desired thickness of the Al_2O_3 layer is reached. The deposition

of one monolayer of Al_2O_3 in an ideal conventional ALD process consists of the following four steps, as depicted in Fig. 2.1:

1. In the first half-reaction, trimethyl-aluminum ($[Al(CH_3)_3]_2$, *TMA*) molecules react with hydroxyl (OH) groups attached to the surface. Al bonds to the oxygen at the growth surface and methane (CH_4) is released. The reaction stops when no more hydroxyl groups are available as reaction sites.

2. The surface is saturated with methyl (CH_3) groups. Excess precursor molecules and by-products of the chemical reaction in the reaction chamber are removed by purging with an inert or oxygen gas and/or pumping the vacuum chamber.

3. In the second half-reaction, aluminum in the $Al-CH_3$ groups at the surface is oxidized by water vapor or ozone (*thermal ALD*) or by oxygen radicals created in an O_2 plasma (*plasma-assisted ALD*), to form aluminum oxide. The reaction by-products depend on the oxidant, but commonly include methane, carbon dioxide, or water [15]. The reaction stops when no more methyl groups are available as reaction sites.

4. The aluminum oxide layer is terminated by hydroxyl groups, which serve as reaction sites for the first half-reaction of the next cycle. Excess precursor molecules and by-products are again removed in a purging/pumping step.

On a real c-Si surface, this simple sequence does not always hold true. If the two half-reactions which form the ALD process were indeed perfectly selective, Al_2O_3 could only be deposited by ALD on OH- or CH_3-terminated surfaces. In all other cases, neither of the precursor molecules would be able to attach to the surface, and no Al_2O_3 film would be deposited. In a real world experiment, the c-Si surface is typically either covered by a thin native oxide after storage in atmosphere, or is terminated by hydrogen after a short dip in hydrofluoric (HF) acid as last step of a standard "Radio Corporation of America" (*RCA*) [16] cleaning se-

quence. The experimental observation that Al_2O_3 films can nevertheless be deposited on non-ideal c-Si surfaces shows that a suitable nucleation surface is formed during the deposition itself, and that deposition of Al_2O_3 on RCA-cleaned c-Si surfaces does not constitute a true ALD process. This topic is addressed in more detail in Chapter 4. In addition, it should be noted that the desposited Al_2O_3 films are *amorphous*, not crystalline as suggested by the simplified representation in Fig. 2.1.

In a conventional ALD process, the separation of the half-reactions is implemented by alternate dosing of the process gases (*sequential ALD*) into a vacuum deposition chamber. To prevent parasitic chemical vapor deposition (*CVD*) and ensure a true ALD process, pumping times of the order of a few seconds are required [17], which severely limits the growth rate to approximately 2 nm/min and makes single-wafer sequential ALD unsuitable for high-throughput industrial manufacturing of silicon solar cells. Nevertheless, sequential ALD has proven to be a reliable tool for laboratory-scale experiments and is extensively used throughout this thesis, mainly in the form of plasma-assisted ALD (*PA-ALD*). Sequential ALD is discussed in Sec. 2.2. Note that sequential water- or ozone-based thermal ALD has been successfully employed in batch-type reactors in order to deposit Al_2O_3 layers on a large number of wafers in parallel, greatly increasing the wafer throughput compared to a single-wafer tool. This technique, however, will not be covered in this thesis, as initial tests with this techniques were unsuccessful.

In a *spatial ALD* process, both half-reactions are spatially separated and sealed off by gas curtains formed by a flow of pressurized nitrogen, thus eliminating the need for intermediate pumping steps. Thus, any unintentional interaction of the process gases is prevented and the deposition can be performed under atmospheric conditions. Al_2O_3 films deposited by spatial ALD have been characterized in detail in this study for the first time. The spatial ALD concept is discussed in Sec. 2.3.

2.2 Sequential atomic layer deposition

2.2.1 Deposition parameters and sample preparation

A commercial OXFORD INSTRUMENTS FLEXAL deposition tool is applied in this study, which allows plasma-enhanced and thermal ALD in the same chamber. Figure 2.2 shows a schematic drawing of the reactor design. Sources of liquid TMA and de-ionized water are connected to the system by means of fast-switching valves. Due to the high vapor pressure of TMA and H_2O, and the small volume of the deposition chamber, these liquid sources provide a sufficient supply of gaseous precursor molecules already at room temperature. A remote inductively coupled plasma (*ICP*) source is used to create an oxygen plasma in the plasma-assisted ALD process, which means that the oxygen plasma is not in direct contact with the silicon wafer during Al_2O_3 deposition. This type of remote-plasma deposition technique is expected to create almost no plasma damage at the surface, and is hence well suited for an excellent silicon surface passivation. Although evidence for severe damage to the c-Si/Al_2O_3 interface during plasma-assisted ALD has been reported [18], the excellent passivation quality can be recovered by a short annealing process.

A separation of the two half-reactions (steps 2 and 4 in Fig. 2.1) is conventionally implemented by alternate dosing of the process gases combined with an intermediate purging and pumping of the vacuum deposition chamber (*sequential ALD*). Exposure times of only a few milliseconds are sufficient to ensure complete saturation of the growth surface [17, 19]. In between both precursor doses, however, the reactor chamber is purged by a non-reactive gas, in our case O_2 gas, and subsequently pumped to remove the residual process gases and reaction products. To prevent parasitic CVD processes and ensure a true ALD process, pumping times of the order of a few seconds are required [17]. Figure 2.3 shows the process sequence used in this study for plasma-assisted and thermal ALD, respectively. The duration of one ALD cycle of 3.9 s (plasma-assisted
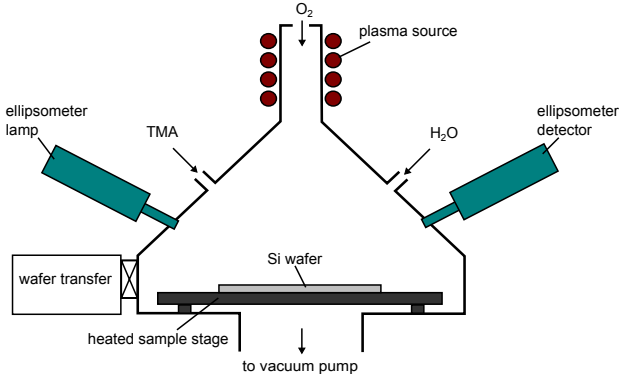
Figure 2.2: Schematic drawing of the OXFORD INSTRUMENTS FLEXAL deposition tool applied in this study. The locations of the Si wafer, process gas inlets, and plasma source are shown. A built-in spectral ellipsometer allows an in-situ optical characterization of the deposited Al_2O_3 layers.

ALD) and 5.6 s (thermal ALD), respectively, is clearly dominated by the long purge/pump steps. Accordingly, the growth rate is typically limited to $< 2\,\mathrm{nm/min}$.
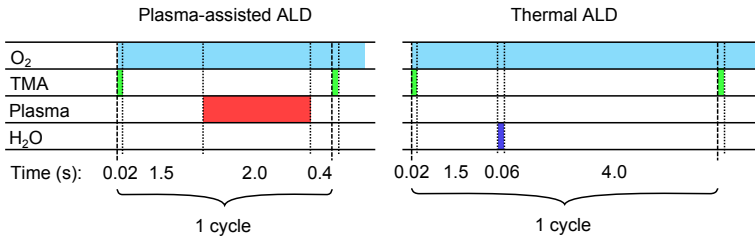
Figure 2.3: Timing of precursor dosing during one ALD cycle for plasma-assisted and thermal ALD applied in this thesis.

A detailed investigation and optimization of the Al_2O_3 deposition using the same ALD reactor is given by Veith [20] for plasma-assisted ALD and by Zielke [21] for thermal ALD, respectively. The resulting processing

sequence is displayed in Fig. 2.3, other relevant parameters of the deposition, as well as the optimized post-deposition anneal, are summarized in Tab. 2.1.

ALD process	Pressure	Plasma power	Deposition temperature	Post-deposition anneal
Plasma-assisted	0.02 mbar	400 W	200 °C	15 min at 425 °C
Thermal	0.02 mbar	–	260 °C	30 min at 350 °C

Table 2.1: Deposition parameters applied in this thesis for plasma-assisted and thermal ALD in an OXFORD INSTRUMENTS FLEXAL reactor.

Unless noted otherwise, the following standard process sequence is used throughout this thesis for the fabrication of Al_2O_3-passivated test samples:

1. The silicon wafer material is selected. Mostly high-quality float-zone (*FZ*) silicon is used in order to reduce the impact of bulk defect recombination on the effective lifetime.

2. (*optional*) The Si wafers typically have a diameter of 6 inch and are hence laser-cut to the desired size. For small samples this is usually $2.5 \times 2.5 \, cm^2$, as this corresponds to the standard size in several tools, e.g. Kelvin probe and vacuum metallization tools.

3. The samples are pre-cleaned in boiling $H_2O{:}NH_4OH{:}H_2O_2$ and $H_2O{:}HCl{:}H_2O_2$ for 10 min each and are rinsed in de-ionized water. This mainly serves to protect the high-purity chemical baths used in the clean-room from any major contamination introduced from outside the clean-room.

4. The samples are cleaned using a standard RCA cleaning sequence. Firstly, the samples are cleaned in $H_2O{:}NH_4OH{:}H_2O_2$ at a temperature of 80 °C, followed by a short dip in hydrofluoric acid (*HF*) to remove the thin chemically grown silicon oxide, which results from an oxidation of the silicon surface during the cleaning. Secondly, the samples are cleaned in $H_2O{:}HCl{:}H_2O_2$ at a temperature of 85 °C,

again followed by a short HF-dip. After each step, the samples are thoroughly rinsed in de-ionized water.

5. Al_2O_3 is deposited by ALD in an OXFORD INSTRUMENTS FLEXAL reactor onto the desired wafer surfaces, using the deposition parameters listed in Tab. 2.1.

6. A post-deposition annealing is typically performed in a quartz tube furnace in a nitrogen ambient. Alternatively, the samples can be annealed with comparable results in a forming gas ambient (95 % N_2, 5 % H_2) or on a hot plate in atmosphere.

2.2.2 Optical characterization

One advantage of the ALD process is the highly conformal and controlled deposition of the dielectric layer. The thickness of the deposited film can be monitored in-situ using a J. A. WOOLLAM M-2000F spectral ellipsometer. However, in order to protect the optical components of the ellipsometer from parasitic deposition, the ALD process is interrupted – and the process chamber flushed with oxygen gas – before any ellipsometry measurement is performed.

The analysis of an ellipsometry measurement requires the assumption of an optical model, which is fit to the experimental data. We have assumed a single Cauchy layer with an extinction coefficient of $k = 0$ and a variable refractive index $n(\lambda) = A + B/\lambda^2 + C/\lambda^4$ on top of a silicon bulk of infinite thickness. Figure 2.4(a) shows the refractive index n as a function of wavelength λ determined for a 100 nm thick Al_2O_3 layer deposited by plasma-assisted ALD. The same experimental data can also be described with an absorbing Al_2O_3 layer ($k > 0$). Assuming an exponential Urbach absorption tail $k = k_0 \exp[\alpha(E - E_0)]$ we obtain $k_0 = 0.4 \pm 0.4$ and $\alpha = (2.5 \pm 0.5) \, \text{eV}^{-1}$, with $E_0 = 6.4 \, \text{eV}$, which corresponds to $k \approx 8 \times 10^{-6}$ at a wavelength of $\lambda = 632.8$ nm. The improvement in the fit quality is, however, only marginal, and we have hence assumed $k = 0$ in the further
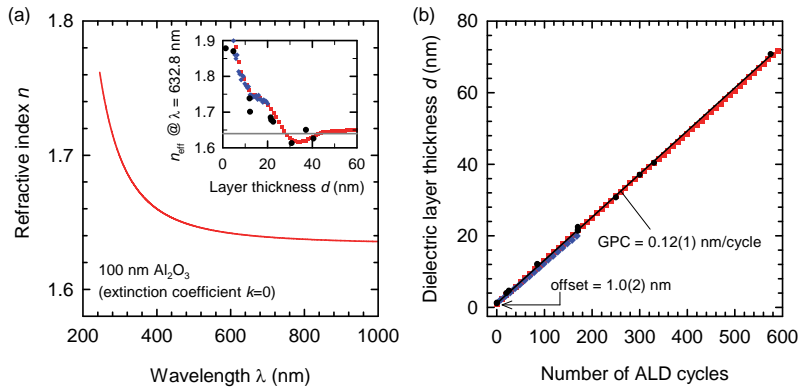
Figure 2.4: (a) Refractive index n as a function of wavelength λ determined for a 100 nm thick Al_2O_3 layer deposited by plasma-assisted ALD. The inset shows the effective refractive index n_{eff} at a wavelength of $\lambda = 632.8$ nm as a function of the deposited layer thickness. (b) Thickness of the deposited dielectric layer as a function of the number of ALD cycles for samples measured after each ALD cycle (blue diamonds), after every ten cycles (red squares), and various samples measured after deposition (black circles).

analysis.

A more realistic optical model of the deposited dielectric layer includes an interfacial layer of SiO_x (compare Sec. 4.2). Due to the optical similarities between Al_2O_3 and intrinsic SiO_x, such an improved model, however, does not yield meaningful thickness values for the SiO_x and Al_2O_3 layers. Accordingly, the interfacial SiO_x layer is not taken into account here, and the values determined for the dielectric layer thickness have to be considered effective values of an SiO_x/Al_2O_3 stack. The inset in Fig. 2.4(a) shows the effective refractive index n_{eff}, where we have varied the parameter A in the Cauchy equation and have kept B and C constant, at a wavelength of $\lambda = 632.8$ nm as a function of the deposited layer thickness. The reference value of $n = 1.64$ determined for 100 nm of Al_2O_3 is indicated by the gray line. Indeed, the refractive index increases significantly with decreasing film thickness for a thickness below ≈ 25 nm. This trend is in good agreement with our model, as the presence of surface roughness and the interfacial SiO_x – which both contribute refractive indices larger than that of Al_2O_3 [22] – is expected to result in a mixing of the silicon, silicon oxide, and aluminum oxide optical constants.

Figure 2.4(b) shows the thickness of the deposited dielectric layer as a function of the number of ALD cycles for two different samples, where the thickness is measured after each ALD cycle (blue diamonds, not all data shown) or after every ten cycles (red squares). In addition, the final thickness of the dielectric layer, measured after deposition, is shown as black circles for various additional samples. All three sets of data form straight lines, as expected for a perfect ALD process. The growth per cycle (*GPC*), given by the slope of a linear fit to the data shown in Fig. 2.4(b), is 0.121 nm/cycle for the undisturbed deposition [black circles in Fig. 2.4(b)]. If the deposition is interrupted, the GPC is reduced to 0.119 nm/cycle (red squares) and 0.112 nm/cycle (blue diamonds), respectively, presumably due to a desorption of precursor molecules during the ellipsometry measurement. Hence, a GPC of (0.12 ± 0.01) nm/cycle describes all data very well.

All sets of data show an offset of (1.0 ± 0.2) nm before the first ALD cycle. The same offset is found on all samples deposited within a few hours after the last HF-dip, and is attributed to a measurement artifact due to surface roughness of the Si wafers. Accordingly, this offset is subtracted from the measured thickness in order to determine the correct thickness of the dielectric layer.

2.2.3 Thermal stability of the passivation quality
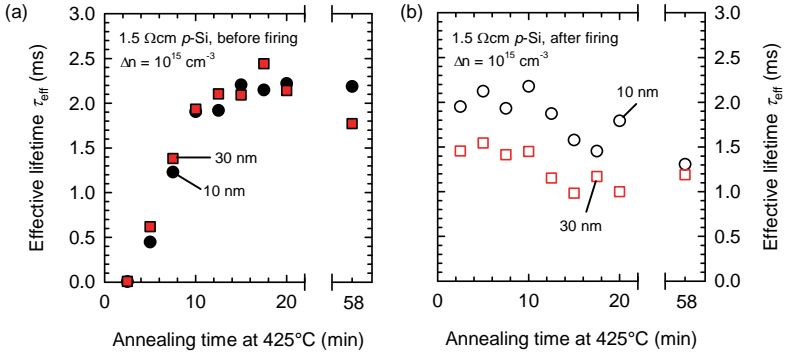
Figure 2.5: Effective lifetime τ_{eff} of $1.5\,\Omega$cm p-Si samples, passivated with 10 nm (black circles) and 30 nm (red squares) of Al_2O_3 deposited by plasma-assisted ALD, as a function of annealing time at a temperature of $425\,^{\circ}$C: (a) after the post-deposition annealing; (b) after an additional firing step at a set peak temperature of $860\,^{\circ}$C and a belt speed of $3\,$m/min.

The thermal stability of Al_2O_3-passivation layers deposited by plasma-assisted ALD on c-Si is analyzed by measuring the effective lifetime τ_{eff} for different samples subjected to different thermal budgets. Figure 2.5(a) shows the effective lifetime τ_{eff} at an excess carrier density of $\Delta n = 10^{15}\,$cm^{-3} as a function of annealing time at a temperature of $425\,^{\circ}$C in a nitrogen ambient. The samples are $1.5\,\Omega$cm p-Si wafers with a size of $2.5 \times 2.5\,$cm^2, passivated with 10 nm and 30 nm of Al_2O_3, respectively, deposited by plasma-assisted ALD. Figure 2.5(b) shows the same data

after an additional firing step in an industrial conveyor belt furnace (Centrotherm Contact Firing Furnace DO 8.600-300-FF) at a set peak temperature of $860\,°C$ and a belt speed of $3\,m/min$. In the as-deposited state, the Al_2O_3 layers deposited by plasma-assisted ALD are virtually non-passivating (not shown), showing lifetimes of $3-4\,µs$. Even after a 2.5 min anneal, the effective lifetime remains below $10\,µs$, which corresponds to an effective surface recombination velocity (*SRV*) of $S_{eff} > 1500\,cm/s$. The low as-deposited effective lifetime for Al_2O_3 layers deposited by plasma-assisted ALD has been linked to plasma damage [18], which results in a large density of interface traps. Accordingly, capacitance-voltage measurements on as-deposited samples yield an almost constant quasi-static capacitance over the full range of the bandgap, which indicates an extremely high interface state density above $10^{13}\,eV^{-1}cm^{-2}$. In addition, the negative fixed charge density at the c-Si/Al_2O_3 interface, which is largely responsible for the excellent surface passivation provided by Al_2O_3, was shown to increase during the post-deposition annealing [18, 23]. At an annealing temperature of $425\,°C$ in a nitrogen ambient, a minimum annealing time of $10-15$ min – which does not appear to be dependent on the Al_2O_3 thickness – is required to attain the maximum effective lifetime.

Figure 2.5(b) shows the measured effective lifetime τ_{eff} of the same samples shown in Fig. 2.5(a), which have been subjected to an additional firing step, at a set peak temperature of $860\,°C$ and a belt speed of $3\,m/min$, after the post-deposition annealing. Two trends are observed: *(i)* For sample which have already been subjected to a large thermal budget during the post-deposition annealing (annealing times $\gtrsim 10$ min), the passivation degrades after the firing step. *(ii)* The thicker Al_2O_3 layer (with a thickness of $30\,nm$) shows a more pronounced degradation, and even shows a degraded passivation for samples which were subjected to only a low or moderate thermal budget during the post-deposition annealing. The latter can also already be observed in Fig. 2.5(a), where the $30\,nm$ layer has degraded after one hour of annealing at $425\,°C$.

A more comprehensive study of the thermal stability of single Al_2O_3 layers and Al_2O_3/SiN_x stacks can be found in Ref. 24.

2.2.4 Surface passivation on different Si wafer surfaces
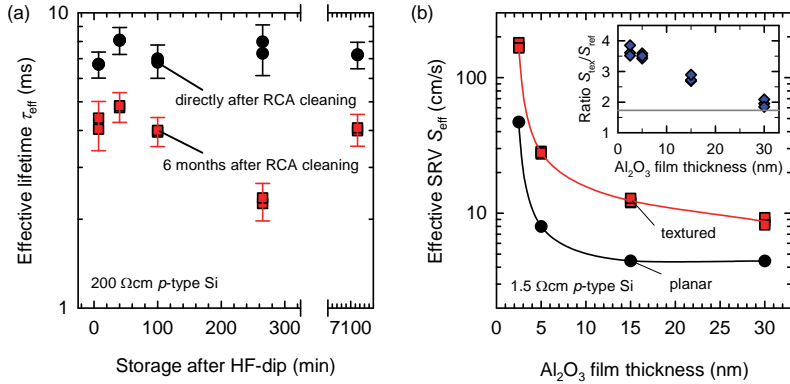
Figure 2.6: (a) Measured effective lifetime τ_{eff} at $\Delta n = 10^{15}\,cm^{-3}$ of a $200\,\Omega cm$ p-type Si wafer for different storage times after the last HF-dip in the cleaning sequence. The last HF-dip is either performed directly (black circles) or 6 months (red squares) after an RCA cleaning. (b) Effective SRV S_{eff} at $\Delta n = 10^{15}\,cm^{-3}$ of a $1.5\,\Omega cm$ p-type Si wafer with planar (black circles) or random-pyramid-textured (red squares) surfaces. The inset shows the ratio of S_{eff} values for textured and planar surfaces. The geometric surface enlargement is indicated by the gray line.

Figure 2.6(a) shows the measured effective lifetime τ_{eff} at $\Delta n = 10^{15}\,cm^{-3}$ of a $200\,\Omega cm$ p-type Si wafer for different surface conditions: One set of samples was stored in a box in a clean-room for six months after a standard RCA cleaning, the second set of samples was RCA-cleaned immediately prior to the experiment. Then, all samples receive a final HF-dip, are stored in the clean-room for a varying period of time, and are then passivated with Al_2O_3. Within the uncertainty range of the measurement, the effective lifetime is not significantly influenced by stor-

18

ing the sample after the last HF-dip. Accordingly, at least for 30 nm of Al_2O_3, the surface passivation does not appear to be sensitive to the presence of a native surface silicon oxide. This is consistent with results presented in Chapters 4 and 5, where the c-Si/Al_2O_3 interface properties are related to a thin interfacial silicon oxide, which is shown to form during the Al_2O_3 deposition. However, storing the samples for 6 months after the RCA cleaning does lead to a reduced effective lifetime, which suggests that the additional HF-dip at the beginning of the experiment is not sufficient to remove all contamination that has accumulated over the course of 6 months, even if the samples are stored in a clean environment.

In a solar cell, the front surface is *textured* to reduce the reflection of incoming photons and to increase the mean path length of a ray of light within the solar cell. On monocrystalline Si this is conveniently achieved by anisotropic etching in an aqueous solution of potassium hydroxide (*KOH*) and isopropyl alcohol (*IPA*), which results in randomly distributed (111)-faceted pyramids with sizes in the range of a few micrometers. Figure 2.6(b) shows the effective SRV S_{eff}, assuming intrinsic bulk recombination, at $\Delta n = 10^{15}\,cm^{-3}$ of a $1.5\,\Omega cm$ *p*-type Si wafer with planar [(100)-oriented, black circles] or random-pyramid-textured [(111)-oriented, red squares] surfaces. The surface area of an ideal (111)-faceted pyramid on a (100)-oriented substrate is $\sin(70.5\,°/2) \approx 1.73$ times larger than its projected base area. The inset in Fig. 2.6(b) shows the ratio S_{tex}/S_{ref} of S_{eff} values for textured and planar surfaces. The gray line indicates the factor 1.73 to account for the surface enlargement. It should be noted, however, that the electronic surface enlargement factor for an Al_2O_3-passivated random-pyramid surface is slightly smaller than the geometric factor, as the edge of the space charge region is more rounded at the tips and valleys of the pyramids. Indeed, no difference is observed in the surface passivation of planar and textured surfaces for an Al_2O_3 thickness of 30 nm, although the Si-(111) surface features a higher density of surface atoms – and hence a higher density of potential surface defects – than the Si-(100) surface [25, p.386]. However, it is possible to compare *relative* values for different Al_2O_3 thicknesses, as the fixed

charge density is considered to be the same for all samples shown in Fig. 2.6(b). We conclude that on textured surfaces a considerably higher minimum thickness of the Al_2O_3 layer is required to achieve the best passivation, compared to planar surfaces where $5 - 10$ nm are sufficient.

A detailed model of the interface between planar crystalline silicon and aluminum oxide, deposited by plasma-assisted atomic layer deposition, will be derived in Chapters 4 and 5.

2.3 High-throughput spatial atomic layer deposition

Conventional sequential ALD reactors limit the deposition rate to below 2 nm/min and require extensive handling times, severely hampering the integration of Al_2O_3 passivation layers into industrial solar cells due to the low throughput. Recently, a *spatial* ALD concept was proposed [19, 26], which enables deposition at atmospheric pressure with deposition rates of up to 70 nm/min.

2.3.1 Principle of spatial ALD
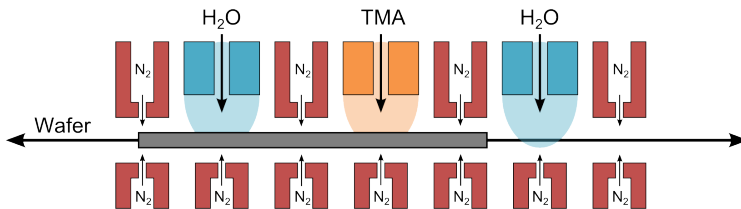
Figure 2.7: Sketch of the linear spatial ALD concept [27]. The TMA and water half-reaction zones are separated by nitrogen curtains. Contactless transport of the wafer is facilitated by nitrogen gas bearings below the wafer.

The spatial ALD process is an H_2O-based thermal ALD process, based on the same two self-limiting half-reactions described above for conventional sequential ALD. Nevertheless, the term *thermal ALD* will be used to denote thermal sequential ALD in this thesis, while thermal spatial ALD will simply be denoted as *spatial ALD*. Although a plasma-assisted spatial ALD concept would in principle be possible, difficulties in ensuring a stable plasma operation in this configuration have not yet been solved.

In a spatial ALD process, both half-reactions are *spatially* separated, as shown by the sketch in Fig. 2.7. The wafers move contactlessly on nitrogen gas bearings and pass TMA and water vapor inlets sealed off by a flow of pressurized nitrogen, forming isolated reaction zones. Since both reaction zones are sealed off by nitrogen flow, any unintentional interaction of the process gases is prevented and the deposition can be performed under atmospheric conditions, an additional advantage concerning the industrial applicability. In a deposition tool with a single reactor [27], the wafers move back and forth underneath the reactor head, each passage depositing one monolayer of Al_2O_3. Alternatively, in a configuration with many reactor heads in-line [28], the wafers move in one direction, each reactor head depositing one monolayer of Al_2O_3 on each wafer.

In the spatial ALD concept, no intermediate purging and pumping steps are required, which significantly decreases the duration of each ALD cycle. The deposition rate is in principle only limited by the time required to supply a sufficient amount of precursor molecules and ensure a complete reaction of the precursor molecules at the wafer surface, which is estimated to be of the order of a few milliseconds [19]. The feasibility of the spatial ALD process was demonstrated in a first proof-of-principle device developed by the Netherlands Organization for Applied Scientific Research (*TNO*) [19], where the wafer rotates beneath a cylindrical reactor head, which significantly simplifies the wafer motion. For this device, a deposition rate of up to $70\,\mathrm{nm/min}$ was experimentally realized [19]. For a linear deposition tool with a single reactor, as shown in Fig. 2.7, the deposition rate is mainly limited by the back-and-forth motion of

the wafer, i.e. stopping and accelerating the wafer, which typically allows deposition rates of $\approx 30\,\text{nm/min}$. Recently, the design of the reactor head shown in Fig. 2.7 has been modified to include an additional pair of TMA and water inlets [29]. In this configuration, two monolayers of Al_2O_3 are deposited during each pass of the wafer, effectively doubling the deposition rate.

2.3.2 Thermal stability of the surface passivation

Al_2O_3 film deposited by spatial ALD were first characterized in this thesis using the proof-of-principle device developed by TNO [19]. In the rotating proof-of-principle tool the Al_2O_3 layer is deposited in a 3 cm wide ring-shaped track. Characterization of the Al_2O_3 layers was performed on both *p*- and *n*-type 6-inch float-zone (*FZ*) silicon wafers. The *p*-type samples were boron-doped $1.3\,\Omega\text{cm}$ shiny-etched silicon wafers of 300 µm thickness. The *n*-type samples were phosphorus-doped $1.0\,\Omega\text{cm}$ wafers, which had been etched in KOH for 10 min to remove the saw damage, resulting in a thickness of 210 µm. To obtain symmetric test samples, Al_2O_3 was deposited on both wafer surfaces by spatial ALD at a deposition rate of 14.4 nm/min. After deposition the wafers were laser-cut in $4 \times 4\,\text{cm}^2$ pieces, each containing a sufficient proportion of the 3 cm wide ring-shaped track of Al_2O_3. The effective carrier lifetimes τ_{eff} were measured as a function of injection density Δn using a SINTON INSTRUMENTS WCT-120 lifetime tester in the transient mode. An upper limit to the surface recombination velocity (*SRV*) was calculated from the measured τ_{eff} using $S_{\text{max}} = W/(2\tau_{\text{eff}})$ [30], where W is the wafer thickness and the bulk lifetime is assumed to be infinite.

The as-deposited Al_2O_3 layers already show a moderate level of surface passivation on *p*- and *n*-type c-Si, yielding effective lifetimes τ_{eff} ranging from 20 µs to 150 µs at $\Delta n = 10^{15}\,\text{cm}^{-3}$, similar to what is observed for sequential thermal ALD [18, 21]. A "mild" anneal for $15 - 30$ min at $350\,^{\circ}\text{C}$ was found to yield the highest effective lifetimes on the *p*-type as
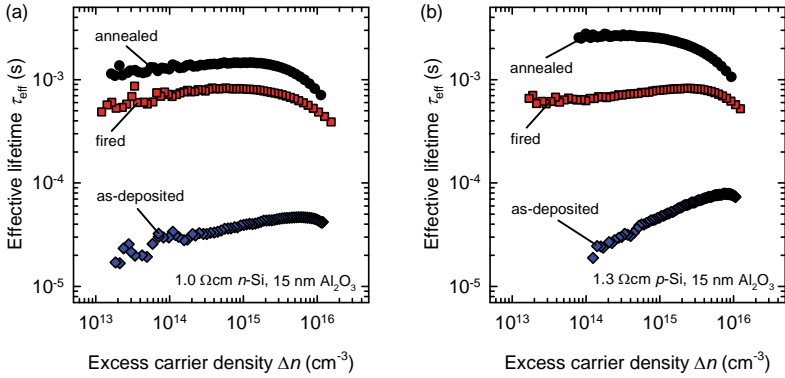
Figure 2.8: Injection-dependent effective lifetimes τ_{eff} measured on (a) $1.0\,\Omega$cm n-type and (b) $1.3\,\Omega$cm p-type silicon samples passivated by spatial ALD-Al_2O_3. The samples are as-deposited (blue diamonds), annealed for 15 min at 350 °C (black circles) or fired at a set peak temperature of 920 °C (red squares); the Al_2O_3 film thickness is 15 nm.

well as on the n-type silicon wafers, again similar to sequential thermal ALD [21]. Figure 2.8 shows the injection-dependent effective lifetimes measured on n- (a) and p-type (b) c-Si wafers, respectively. The samples were either as-deposited, annealed for 15 min at 350 °C, or fired at a belt speed of 5.9 m/min and a set peak temperature of 920 °C, corresponding to an actual peak temperature of about 800 °C and a dwell time of ≈ 6 s above 600 °C. For the annealed samples, the maximum achieved lifetimes at $\Delta n = 10^{15}\,\mathrm{cm}^{-3}$ were $\tau_{eff} = 2.5$ ms for the p-type and $\tau_{eff} = 1.5$ ms for the n-type wafers, corresponding to S_{max} values of 6.0 cm/s and 7.0 cm/s, respectively. The measured effective lifetimes show virtually no injection level dependence in the relevant injection range between $10^{13}\,\mathrm{cm}^{-3}$ and $10^{15}\,\mathrm{cm}^{-3}$, which is significant for one-sun operation of typical solar cells. The achieved lifetimes at $\Delta n = 10^{15}\,\mathrm{cm}^{-3}$ after firing were $\tau_{eff} = 790$ µs for the p-type and $\tau_{eff} = 815$ µs for the n-type wafers, corresponding to S_{max} values of 19.0 cm/s and 12.9 cm/s, respectively. The excellent firing stability and the weak injection dependence of the passivation quality

makes the studied Al_2O_3 layers deposited by spatial ALD well suited for future generations of industrial high-efficiency silicon solar cells.

2.3.3 Surface passivation on large area

A PROCESS DEVELOPMENT TOOL (*PDT*) – later renamed INPASSION ALD [29] – manufactured by the Dutch company SOLAYTEC was employed to assess the passivation quality of Al_2O_3 films deposited by spatial ALD on $15.6 \times 15.6\,cm^2$ Si wafers. In the PDT, the wafer is heated to $200\,°C$ within 6 seconds, and is then cycled through the core reactor sketched in Fig. 2.7 at a rate of $2\,Hz$, resulting in a deposition rate of 4 monolayers per second, or $\approx 30\,nm/min$. If the desired number of ALD cycles – and correspondingly the desired layer thickness – is reached, the wafer is ejected from the core reactor and is cooled down for 30 seconds on a cooling track. During this time the next wafer can already be processed in the core reactor. We use $4\,\Omega cm$ *n*-type Czochralski-grown (*Cz*) silicon wafers with a size of $15.6 \times 15.6\,cm^2$ (full-square), which were etched to a thickness of $180 \pm 15\,\mu m$ in an aqueous KOH solution and received a standard RCA clean. Al_2O_3 films with a thickness of 10, 30 and $200\,nm$, respectively, were deposited on both wafer surfaces by spatial ALD, and were subsequently annealed at $350\,°C$ for 30 min in a nitrogen ambient to activate the passivation. In addition, four wafers were passivated with $10\,nm$ of Al_2O_3 deposited by plasma-assisted ALD in an OXFORD IN-STRUMENTS FLEXAL reactor and annealed at $425\,°C$ for 15 min. These wafers serve as a reference, as Al_2O_3 deposited by plasma-assisted ALD is known to yield extremely low surface recombination velocities on lowly doped *n*-type silicon [3, 10] and is extensively used throughout this work.

A camera-based dynamic infrared lifetime mapping (*ILM*) technique [31] provides a fast analysis of the lateral uniformity of the surface passivation. In the dynamic ILM analysis, wafers are exposed to a constant illumination intensity, which has to be carefully set to compare lifetime mappings of different wafers at a similar injection density Δn. In addition,

it should be kept in mind that the local injection density Δn might vary over the wafer area. The injection-density-dependent effective lifetime $\tau_{\text{eff}}(\Delta n)$ is measured by transient photoconductance decay (*PCD*) using a SINTON INSTRUMENTS WCT-120 lifetime tester in the transient mode, with the wafers centered over the sensor area. The corresponding maximum effective surface recombination velocity (*SRV*) S_{max} is calculated from the measured τ_{eff} using the equation $S_{\text{max}} = W/(2\tau_{\text{eff}})$ [30], where $W = 180\,\mu\text{m}$ is the mean wafer thickness. The bulk lifetime was assumed to be infinite. We combine both measurement techniques – dynamic ILM and transient PCD – in order to gain information about both the spatial variations and the injection density dependence of the effective lifetime τ_{eff}.
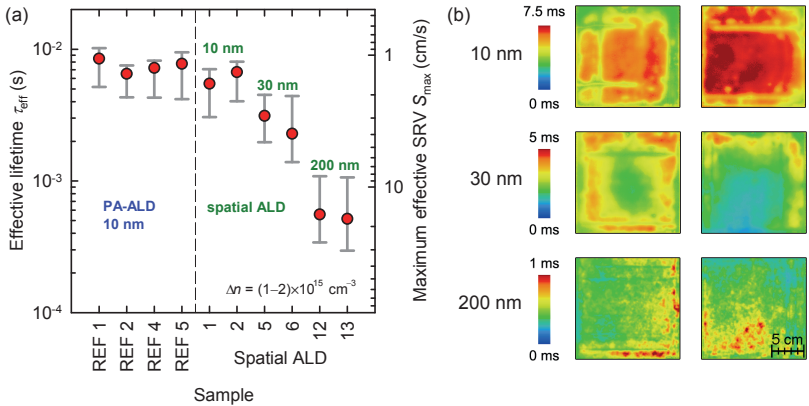
Figure 2.9: (a) Effective lifetime τ_{eff} and maximum effective SRV S_{max} for Al$_2$O$_3$ thicknesses of 10, 30, and 200 nm deposited by spatial ALD, and 10 nm deposited by plasma-assisted ALD, respectively. The lifetime is calculated from the lifetime mappings shown in (b) by averaging over the wafer area, error bars denote the minimum and maximum values; (b) Spatially resolved lifetime mappings measured by dynamic ILM for $15.6 \times 15.6\,\text{cm}^2$ $4\,\Omega\text{cm}$ n-type Cz-Si wafers passivated by spatial ALD-Al$_2$O$_3$.

Figure 2.9(a) shows the effective lifetime τ_{eff} measured by dynamic ILM and averaged over the wafer area, excluding $\approx 0.5\,\text{cm}$ around the wafer

edges. The error bars denote the minimum and maximum lifetime values recorded within this area. The spatially resolved lifetime mappings corresponding to the data points are shown in Fig. 2.9(b) for the samples passivated by spatial ALD. The lifetime values and maximum SRVs are summarized in Table 2.2. The reference wafers passivated by plasma-assisted ALD yield effective lifetimes at a mean injection density of $\Delta n = (1-2) \times 10^{15} \, \text{cm}^{-3}$ between 4.2 and 10.2 ms, corresponding to $S_{\text{max}} = 0.9 - 2.2 \, \text{cm/s}$. A comparable level of surface passivation is achieved with 10 nm of Al_2O_3 deposited by spatial ALD, yielding effective lifetimes between 3.1 and 8.1 ms ($S_{\text{max}} = 1.1 - 2.9 \, \text{cm/s}$). A slight reduction of the effective lifetime along two parallel stripes might be attributed to the wafer handling prior to deposition or during cooling. Adjustments to the wafer handling system successfully eliminated these regions of reduced lifetimes.

ALD	Thickness	Eff. lifetime τ_{eff}	Max. SRV S_{max}
Plasma	10 nm	$4.2 - 10.2$ ms	$0.9 - 2.2$ cm/s
spatial	10 nm	$3.1 - 8.1$ ms	$1.1 - 2.9$ cm/s
spatial	30 nm	$1.4 - 4.5$ ms	$2.0 - 6.5$ cm/s
spatial	200 nm	$0.3 - 1.1$ ms	$8.2 - 30.5$ cm/s

Table 2.2: Effective lifetime τ_{eff} measured by ILM and maximum SRV S_{max} for different Al_2O_3 passivation layers deposited by plasma-assisted and spatial ALD, respectively.

We observe a reduced effective lifetime for an Al_2O_3 thickness exceeding 10 nm. For a film thickness of 30 nm this effect is marginal, yielding effective lifetimes between 1.4 and 4.5 ms ($S_{\text{max}} = 2.0 - 6.5 \, \text{cm/s}$). For a film thickness of 200 nm, however, we measure significantly reduced effective lifetimes between 300 µs and 1.1 ms, corresponding to $S_{\text{max}} = 8.2 - 30.5 \, \text{cm/s}$. The reasons for the degradation of surface passivation quality with increasing film thickness are not yet fully understood. As this effect is absent prior to annealing of the lifetime samples, the

degradation might be related to thermal stress and the accompanying damage to the Si/Al_2O_3 interface induced during thermal treatment. The reduced lifetime for thick Al_2O_3 layers, however, is of no concern for the industrial fabrication of solar cells, as such thick layers of Al_2O_3 are usually not desired. Superior optical properties and firing stability are obtained with a stack system comprising a thin ($< 10\,nm$) Al_2O_3 passivation layer deposited by ALD and a thicker capping layer, commonly of hydrogenated amorphous SiN_x deposited by plasma-enhanced chemical vapor deposition (*PECVD*) [9, 24].
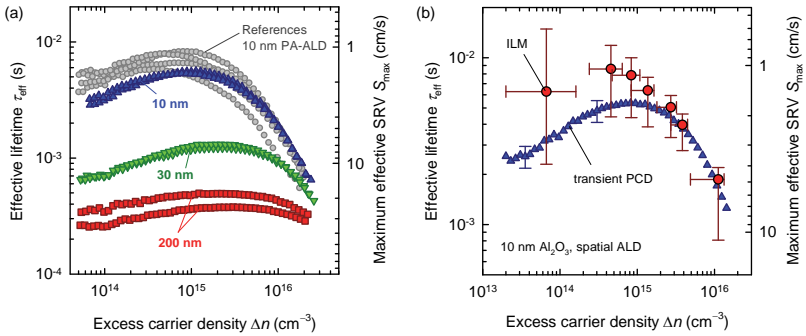
Figure 2.10: (a) Effective lifetime τ_{eff} and maximum effective SRV S_{max} as function of injection density Δn measured by transient PCD. The Al_2O_3 thickness is 10, 30, and 200 nm deposited by spatial ALD, and 10 nm deposited by plasma-assisted ALD, respectively. (b) Comparison of the injection density dependent τ_{eff} and S_{max} as measured by transient PCD (blue triangles) and dynamic ILM (red circles) for 10 nm of Al_2O_3 deposited by spatial ALD.

The dependence of the surface passivation quality on injection density Δn is addressed in Fig. 2.10. Figure 2.10(a) shows the effective lifetime τ_{eff} (left axis) and maximum effective SRV S_{max} (right axis) as a function of injection density Δn measured by transient PCD. In agreement with Fig. 2.9, the reference samples passivated by plasma-assisted ALD and the samples passivated with 10 nm of Al_2O_3 deposited by spatial ALD show a comparable level of surface passivation. For thicker Al_2O_3 layers

the effective lifetime is reduced. Independent of the Al_2O_3 thickness, all samples only show a minor injection density dependence of the effective lifetime. Taking into account that the same shape of the $\tau_{eff}(\Delta n)$ curve is observed for all samples, including the reference samples passivated by plasma-assisted ALD, the slight decrease in effective lifetime for low injection densities is most likely attributed to recombination in the bulk silicon. Figure 2.10(b) compares the $\tau_{eff}(\Delta n)$ data obtained by transient PCD with lifetime values extracted from spatially resolved lifetime mappings as described above. According to Fig. 2.10(b), the injection dependence of the effective lifetime is most pronounced in low-lifetime regions. In addition, hole transport through the Al_2O_3-induced inversion layer towards the defective wafer edge leads to an increased recombination close to the wafer edge at lower injection densities [32]. On the other hand, the regions of the highest effective lifetime do not appear to be significantly reduced at lower excess carrier densities and yield surface recombination velocities $S_{max} < 1\,\mathrm{cm/s}$.

3 Theory and analysis

3.1 Band bending at the c-Si surface

The negative fixed charges present in an Al_2O_3 passivation layer deposited on silicon cause a variation in the carrier densities and electrostatic potential within the silicon wafer towards the interface. The surface band bending, and the resulting depletion of electrons (for negative charges in the Al_2O_3) near the recombination-active c-Si/Al_2O_3 interface, is a main contribution to the excellent passivation quality provided by Al_2O_3, and plays a major role in several experimental techniques used in this thesis. A detailed theoretical treatment of surface band bending in the so-called *band-bending approximation* is given in Ref. 33, the most important equations relevant to this thesis are outlined here.

3.1.1 Energy bands and charge distribution

Figure 3.1 shows a sketch of the energy band diagrams and charge distributions near the silicon surface for a metal/Al_2O_3/Si capacitor on *p*-type Si in accumulation and depletion/inversion [33, p.52]. We assume a semi-infinite silicon wafer with a single homogeneous Al_2O_3 layer at the front, which is characterized by its oxide capacitance C_{ox} per unit area and a fixed charge density $Q_f < 0$ at the Al_2O_3/Si interface. In addition, we demand that electric fields only cause a shift of the energy levels in the silicon bands, but do not change the density of states in the valence and conduction band (*band-bending approximation*). Whenever the device deviates from thermal equilibrium, we demand that both the electron and hole quasi-Fermi levels are constant ("flat") throughout the space charge region.
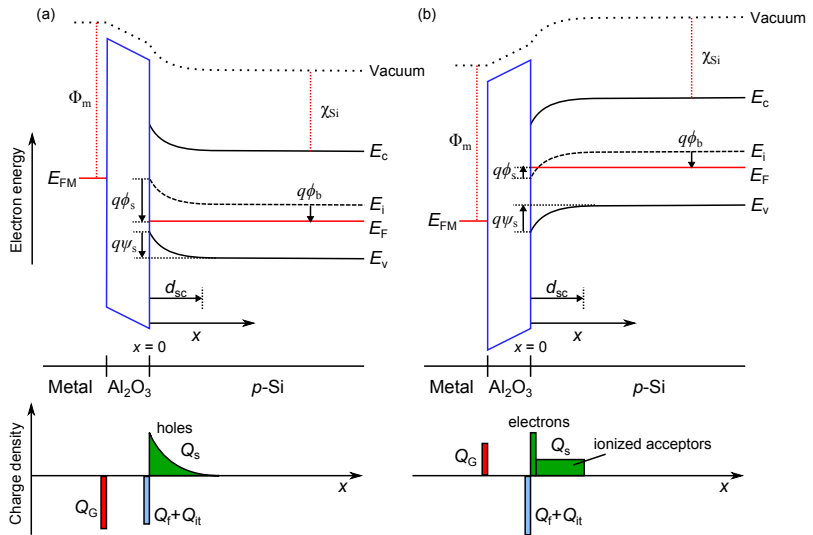
Figure 3.1: Energy diagrams (top) and charge distributions (bottom) near the silicon surface, shown exemplarily for *p*-type Si for a metal/Al$_2$O$_3$/Si capacitor (a) in accumulation and (b) in depletion/inversion. The various symbols are defined in the text. Arrows pointing down denote negative potentials.

Within the silicon wafer, E_v and $E_c = E_v + E_g$ denote the upper edge of the valence band and the lower edge of the conduction band, respectively, where E_g is the silicon bandgap. The intrinsic energy level E_i is chosen parallel to valence and conduction band everywhere in the silicon. Deep in the silicon bulk, E_i is equal to the intrinsic Fermi level $E_{F,i}$, which is given by the equation

$$E_{F,i} = \frac{E_g}{2} + \frac{k_B T}{2} \ln\left(\frac{N_v}{N_c}\right), \qquad (3.1)$$

where N_v and N_c are the effective densities of states of the valence and conduction band. The intrinsic Fermi level lies slightly below the middle of the bandgap in silicon due to the different effective densities of states of the valence and conduction band. This difference however is smaller than $\frac{1}{3}k_B T$, and E_i in the bulk can be identified with the middle of the bandgap in good approximation.

In thermal equilibrium, the Fermi level E_F is constant throughout the silicon. The potential $\phi(x)$ denotes the position of the Fermi level with respect to the intrinsic level, that is $\phi(x) = (E_F - E_i)/q$. In Fig. 3.1, arrows pointing up denote positive potential, and arrows pointing down denote negative potential. The shape of the energy bands at any depth x is determined by the *bulk potential* $\phi_b = \phi(x \to \infty)$ and the *surface potential* $\phi_s = \phi(x=0)$. The *band bending* $\psi(x)$ specifies the potential $\phi(x)$ at a depth x with respect to the value in the bulk, that is $\psi(x) = \phi(x) - \phi_b$. The region where $\psi(x) \neq 0$ is called the *space charge region (SCR)*, its depth is given by d_{sc}. The charges present in the MIS system are depicted in the bottom part of Fig. 3.1: The fixed charge density Q_f and the charge density Q_{it} stored in interface traps are considered to be located directly at the c-Si/Al$_2$O$_3$ interface. The band bending within the c-Si results in a silicon surface charge density Q_s, which is mainly built up by majority carriers in accumulation, and ionized dopants and minority carriers in depletion and inversion. In addition, a charge density Q_G builds up at the metal/Al$_2$O$_3$ interface depending on the applied external gate voltage. A difference in the workfunctions of gate metal

and silicon leads to an additive constant ϕ_{ms} to the gate voltage, which is given by

$$\phi_{\mathrm{ms}} \equiv \Phi_{\mathrm{m}} - \left(\chi_{\mathrm{Si}} + E_{\mathrm{g}}/2 - q\phi_{\mathrm{b}}\right), \qquad (3.2)$$

where Φ_{m} is the metal workfunction and χ_{Si} is the silicon electron affinity. The difference in the Fermi levels E_{F} in the silicon and E_{FM} in the metal is equal to the externally applied gate voltage $V_{\mathrm{G}} = (E_{\mathrm{F}} - E_{\mathrm{FM}})/q$.

In order to facilitate the readability, we define the following abbreviations:

$$\beta \equiv \frac{q}{k_{\mathrm{B}}T}, \quad u \equiv \beta\phi, \quad v \equiv \beta\psi, \quad \text{with} \quad \psi(x) = \phi(x) - \phi_{\mathrm{b}}. \qquad (3.3)$$

Figure 3.1 can equally be applied to Al_2O_3-passivated lifetime samples without metal contacts, as the band diagram within the silicon is identical.

3.1.2 Charge carrier densities in Fermi-Dirac and Boltzmann statistics

The probability $f(E)$ that a state at an energy E is occupied by an electron is given by the Fermi-Dirac function

$$f(E) = \frac{1}{1 + \exp\left(\frac{E - E_{\mathrm{F}}}{k_{\mathrm{B}}T}\right)}. \qquad (3.4)$$

The quasi-free electron density n in a semiconductor is then given by the integral over the density of states $N(E)$ in the conduction band, multiplied by the occupation probability $f(E)$, that is

$$n = \int_{E_{\mathrm{c}}}^{\infty} N(E) f(E) \mathrm{d}E \quad \propto \quad \int_{0}^{\infty} \epsilon^{\frac{1}{2}} f(\epsilon) \mathrm{d}\epsilon \equiv F, \qquad (3.5)$$

where $\epsilon \equiv E - E_{\mathrm{c}}$, F is the second-order Fermi integral, and the density of states $N(E)$ is assumed to be parabolic near the band edges. For Fermi-Dirac statistics, Eq. 3.5 cannot be solved analytically. An approximation

to the numerical solution of Eq. 3.5, accurate ($\Delta\eta < 1\,\text{mV}$) for Fermi energies up to $2k_\text{B}T$ within the conduction or valence band, and hence applicable to most semiconductor devices with reasonably small error, is given by the following equation [34]:

$$g_1\exp\left(\eta\right) = F\exp\left(bF\right), \quad \text{with} \quad g_1 = \frac{\sqrt{\pi}}{2} \text{ and } b = \frac{1}{\sqrt{2\pi}}, \qquad (3.6)$$

where η is the position of the Fermi energy relative to the valence or conduction band edge, that is $\eta \equiv E_\text{F} - E_\text{c}$ for electrons and $\eta \equiv E_\text{v} - E_\text{F}$ for holes. The carrier densities n and p are then given by

$$n \text{ or } p = \frac{N_\text{eff}F}{g_1} = \frac{N_\text{eff}}{g_1 b}\, W\left(g_1 b e^\eta\right), \qquad (3.7)$$

where N_eff is the effective density of states of the respective band (valence band for p and conduction band for n), and $W(x)$ is the Lambert W function [35].

In thermal equilibrium, and applying the Boltzmann approximation of the Fermi-Dirac distribution, given by $f(E) \approx \exp(-\frac{E - E_\text{F}}{k_\text{B}T})$, the solution to Eq. 3.5 is $F = g_1\exp(\eta)$, and the electron and hole densities $n(x)$ and $p(x)$ at a depth x are given by

$$n(x) = N_\text{D}\, e^{\beta\psi(x)} = n_\text{i}\, e^{\beta\phi(x)} \quad \text{and} \quad p(x) = N_\text{A}\, e^{-\beta\psi(x)} = n_\text{i}\, e^{-\beta\phi(x)}, \qquad (3.8)$$

where N_D and N_A are the donor and acceptor densities, respectively. The Boltzmann approximation is accurate ($\Delta\eta < 1\,\text{mV}$ at room temperature) for Fermi energies more than $2k_\text{B}T$ below the conduction band or above the valence band, respectively [34]. However, even for Fermi energies slightly within the valence or conduction band, the Boltzmann approximation overestimates the charge carrier densities only by a factor of less than 2 ($\eta < +1k_\text{B}T$) or 2.5 ($\eta < +2k_\text{B}T$), which can often be neglected compared to other uncertainties. Accordingly, the Boltzmann approximation and Eq. 3.8 are used throughout this thesis. A notable exception is Chapter 7, where a small uncertainty in the hole concentration leads to a considerable uncertainty in the field-dependent hole mobility, and hence Fermi-Dirac statistics are employed.

3.1.3 Solution of the charge neutrality condition

The silicon surface charge Q_s is calculated from the potential $\phi(x)$ in the silicon wafer, which is given by the one-dimensional Poisson equation

$$\frac{\mathrm{d}^2\phi(x)}{\mathrm{d}x^2} = -\frac{\varrho(x)}{\varepsilon_s}, \tag{3.9}$$

where $\varrho(x)$ is the total charge density in the silicon and $\varepsilon_s = 11.7\,\varepsilon_0$ is the dielectric permittivity of silicon. Solving the Poisson equation results in the following equation for the electric field at the silicon surface:

$$F_s = \mathrm{Sgn}(u_b - u_s)\frac{F(u_s, u_b)}{\beta\lambda_i}, \tag{3.10}$$

with the intrinsic Debye length

$$\lambda_i = \sqrt{\frac{\varepsilon_s}{2\beta q n_i}} \tag{3.11}$$

and a dimensionless electric field

$$F(u_s, u_b) = \sqrt{2}\left[(u_b - u_s)\sinh u_b - (\cosh u_b - \cosh u_s)\right]^{\frac{1}{2}}. \tag{3.12}$$

The total charge per unit area Q_s within the silicon is then given as a function of the surface potential u_s by Gauss's law as

$$Q_s(u_s) = \varepsilon_s F_s = \mathrm{sgn}(u_b - u_s)\frac{\varepsilon_s}{\beta\lambda_i}F(u_s, u_b). \tag{3.13}$$

The hyperbolic functions in Eq. 3.12 are related to a sum (cosh) or difference (sinh) of electron and hole concentrations, as the latter are exponential functions of the potential $u(x)$ in the Boltzmann approximation. Accordingly, Eq. 3.13 can be rewritten as a function of the bulk and surface charge carrier concentrations, and ultimately as a function of the bulk potential ϕ_b and the surface band bending ψ_s. Under non-equilibrium conditions, e.g. if excess carriers are generated by illumination, the bulk

potential is replaced by the electron and hole quasi-Fermi potentials u_n and u_p, and Eq. 3.13 becomes [36]

$$
\begin{aligned}
Q_{\mathrm{s}}(v_{\mathrm{s}}) = \\
- \operatorname{sgn}(v_{\mathrm{s}}) \sqrt{\frac{2q\varepsilon_{\mathrm{s}}n_{\mathrm{i}}}{\beta}} \left[e^{-u_p - v_{\mathrm{s}}} - e^{-u_p} + e^{u_n + v_{\mathrm{s}}} - e^{u_n} + v_{\mathrm{s}}\frac{N_{\mathrm{A}} - N_{\mathrm{D}}}{n_{\mathrm{i}}} \right]^{\frac{1}{2}},
\end{aligned}
\tag{3.14}
$$

where N_{A} and N_{D} are the acceptor and donor concentrations, respectively. For an Al_2O_3-passivated lifetime sample, this allows to calculate the surface band bending $\psi_{\mathrm{s}} = v_{\mathrm{s}}/\beta$, and hence the charge carrier densities n_{s} and p_{s} at the c-Si/Al_2O_3 interface, based on an iterative numerical procedure introduced by Girisch *et al.* [36]. In this model, ψ_{s} is varied starting from an arbitrary initial estimate, and the deviation from charge neutrality is evaluated, which is defined as

$$
\delta \equiv Q_{\mathrm{f}} + Q_{\mathrm{s}}(\psi_{\mathrm{s}}) + Q_{\mathrm{it}}(\psi_{\mathrm{s}}).
\tag{3.15}
$$

The value of ψ_{s} is adjusted and the calculations are repeated until charge neutrality at the interface is fulfilled with the desired accuracy, that is $\delta \approx 0$.

The interface-trapped charge Q_{it} is calculated from Eq. 3.18. In the case of Al_2O_3, however, for most practical cases $Q_{\mathrm{f}} \gg Q_{\mathrm{it}}(\psi_{\mathrm{s}})$, and the interface trapped charges can be neglected.

According to Maxwell's equations, the electric field is the gradient of the potential ϕ in the silicon wafer. Hence, if the surface potential is know, the electrostatic potential as a function of depth is obtained from the numerical integration of

$$
F(x) = \frac{1}{\beta}\frac{\mathrm{d}u}{\mathrm{d}x} = \operatorname{sgn}(u_{\mathrm{b}} - u_{\mathrm{s}})\frac{F(u_x, u_{\mathrm{b}})}{\beta\lambda_{\mathrm{i}}} \quad \Rightarrow \quad x(u_x) = \lambda_{\mathrm{i}}\int\limits_{u_{\mathrm{s}}}^{u_x} \frac{\mathrm{d}u}{F(u, u_{\mathrm{b}})},
\tag{3.16}
$$

which yields the depth x at which the potential u has the value u_x.

3.1.4 Response to gate voltage variations

Figure 3.2 shows a sketch of the interface states within the silicon bandgap for a given surface energy E_s, assuming an arbitrary continuous distribution of interface states. The surface energy E_s is defined as that energy level within the silicon bandgap at the c-Si/Al$_2$O$_3$ interface, which lies opposite the bulk Fermi level. Using the potentials defined in Fig. 3.1, E_s for a given external bias voltage V_G is given by

$$E_s(V_G) = E_i + q\phi_s(V_G) = E_i + q\phi_b + q\psi_s(V_G). \tag{3.17}$$

Interface traps can exchange charge with the silicon bulk via capture or emission of charge carriers. Hence, in thermal equilibrium, interface state occupation follows a Fermi-like distribution centered around the surface energy E_s. Accordingly, the mean energy of the electron ensemble trapped in the interface states is equal to the mean energy of electrons in the silicon bulk [see Fig. 3.2(a)]. A change in gate voltage causes a change in surface potential ψ_s, and hence changes the surface energy E_s. This change can be considered instantaneous, as the dielectric relaxation time $\tau_0 = \varepsilon_s \varrho_{bulk}$ in silicon is of the order of $1\,\mathrm{ps}$ for typical bulk resistivities around $\varrho_{bulk} \approx 1\,\Omega\mathrm{cm}$. Charge exchange between the interface traps and the silicon bulk, however, is limited by the majority carrier capture time constants of the interface traps, which generally are larger than the dielectric relaxation time. Eventually, the mean energy of electrons in the silicon and in the interface traps will equilibrate, albeit with a certain time delay. In order to reach equilibrium, the number of charges stored in the interface traps needs to change with a change in ψ_s, which contributes to the capacitance of the MIS capacitor [see Fig. 3.2(d)].

In the following, we consider a modulation of the gate bias voltage V_G by a small ac voltage δV with angular frequency ω. For the sake of simplicity we assume n-type Si, where electrons are the majority carriers. The occupation probability of the interface states is approximated by a simple step function. Before electrons can be transferred between silicon bulk and interface states, the instantaneous change in surface energy
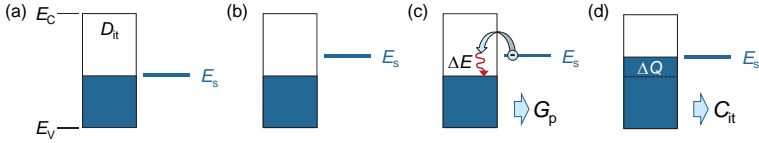
Figure 3.2: Sketch of the interface states and the silicon surface energy E_s (a) in equilibrium, (b) immediately after a change in E_s, (c) during charge transfer between silicon and interface states, and (d) in equilibrium at the new value of E_s. The blue area represents interface states occupied by an electron.

causes interface states below E_s to be unoccupied [see Fig. 3.2(b)] or interface states above E_s to be occupied, respectively, depending on the polarity of δV. In the positive half-cycle of the ac modulation ($\delta V > 0$), the surface energy, and hence the mean energy of electrons near the silicon surface, is increased. An energy loss occurs when electrons are captured by interface traps with a lower mean energy, as shown in Fig. 3.2(c). In the negative half-cycle ($\delta V < 0$), the surface energy falls below the mean energy of the trapped electrons. Electrons are hence emitted from the interface traps, once again causing a loss in energy.

The energy loss is proportional to the difference in mean energy between eletrons in the silicon and electrons trapped in interface states at the time of electron capture/emission, which depends on the capture time constants of the interface states and on the angular frequency ω of the ac modulation. If ω is very low, the surface potential ψ_s changes slowly and the interface states can react almost intantaneously. If ω is very high, no interface trap response occurs at all. The energy loss related to charging/discharging of interface traps is supplied by the voltage source of the experimental setup and can be measured as an equivalent parallel conductance. All relevant information about the dynamics of interface recombination can be extracted from the frequency-dependent normalized equivalent parallel conductance $G_p(\omega)/\omega$, which is directly related to the energy loss occurring during one charging/discharging cycle.

Accordingly, information about the interface states can be extracted both

from a measurement of the capacitance resulting from a change in the stored charge as voltage changes (described in Sec. 3.2), as well as from a measurement of the conductance due to an energy loss during the charging/discharging of a trap (described in Sec. 3.3).

3.1.5 Interface-trapped charge density

Within the scope of the Shockley-Read-Hall (*SRH*) theory, the charge density Q_{it} trapped in the interface states depends on the surface band bending ψ_s and on the donor or acceptor nature of the interface traps. A donor trap is neutral when empty, and positively charged when occupied by a hole, while an acceptor trap is neutral when empty, and negatively charged when occupied by an electron. Note that such treatment on interface traps is only approximate if amphoteric defects are involved, which allow transitions by more than one unit charge [37]. Applying SRH statistics, the electron-occupancy function $f_A(E)$ of acceptor traps and the hole-occupancy function $f_D(E)$ of donor traps are derived from the demand of equal capture and emission rates under steady-state conditions [38]. The interface-trapped charge density Q_{it} is then given by the equations [36]

$$Q_{it}(\psi_s) = -q \int_{E_v}^{E_c} D_A(E) f_A(E, \psi_s) \mathrm{d}E + q \int_{E_v}^{E_c} D_D(E) f_D(E, \psi_s) \mathrm{d}E, \quad (3.18)$$

$$f_A(E, \psi_s) = \frac{\sigma_n n_s + \sigma_p p_1}{\sigma_n (n_s + n_1) + \sigma_p (p_s + p_1)}, \quad (3.19)$$

$$f_D(E, \psi_s) = \frac{\sigma_n n_1 + \sigma_p p_s}{\sigma_n (n_s + n_1) + \sigma_p (p_s + p_1)}, \quad (3.20)$$

$$\text{with } n_1(E) = n_i \, e^{\beta(E - E_i)} \text{ and } p_1(E) = n_i \, e^{-\beta(E - E_i)}, \quad (3.21)$$

where D_A (D_D) are the acceptor (donor) interface state densities, σ_n (σ_p) are the electron (hole) capture cross sections, and n_s (p_s) are the electron (hole) densities at the surface, given by Eq. 3.8. Note that σ_n, σ_p, n_1, and p_1 are functions of energy E, and n_s and p_s are functions of ψ_s, which has been omitted in Eq. 3.19 and 3.20 for improved readability.

The acceptor or donor nature of the interface traps needs to be known in order to correctly calculate the charge density Q_{it} stored in the interface traps. An upper limit of Q_{it} can be estimated if all interface states carry the same charge. For typical D_{it} values of c-Si wafers passivated with annealed Al_2O_3, this yields a maximum value of

$$Q_{it.max} = \int\limits_0^{E_g} q D_{it}(E) dE < 3 \times 10^{11}\,cm^{-2}, \tag{3.22}$$

which is one order of magnitude smaller than typical values of the fixed charge density of $Q_f = -4 \times 10^{12}\,cm^{-2}$ for Al_2O_3-passivated samples. The interface trapped charge might dominate if the fixed charge density is compensated by deposited corona charges as described in Sec. 3.4. In that case, however, inhomogeneities introduced during corona charging cause an uncertainty and lateral variation in the deposited charge density typically larger than $Q_{it.max}$.

3.2 Capacitance – voltage analysis

3.2.1 Flat-band voltage and capacitance model

The recombination parameters of an interface trap can be obtained as a function of the energetic position of the trap within the silicon bandgap by varying the dc component of the gate voltage V_G. If the external gate voltage is varied, the band bending ψ_s at the c-Si/Al_2O_3 interface and, accordingly, the surface energy E_s changes as well. Hence, in order to convert a given gate voltage V_G to its respective surface energy E_s within

the silicon bandgap, the dependence of surface band bending ψ_s on gate voltage V_G needs to be known.

Gauss's law applied to the charges present at the c-Si/Al$_2$O$_3$ interface demands that

$$C_{ox}\left(V_G - \psi_s - \phi_{ms}\right) = -Q_{it}(\psi_s) - Q_s(\psi_s) - Q_f, \qquad (3.23)$$

where the left hand side of the equation, $C_{ox}\left(V_G - \psi_s + \phi_{ms}\right)$, corresponds to the charges Q_G on the gate contact. Taking the derivative with respect to ψ_s yields

$$C_{ox}\frac{dV_G}{d\psi_s} = C_{ox} + C_{it}(\psi_s) + C_s(\psi_s), \qquad (3.24)$$

where

$$C_{it}(\psi_s) \equiv -\frac{dQ_{it}}{d\psi_s} \quad \text{and} \quad C_s(\psi_s) \equiv -\frac{dQ_s}{d\psi_s}. \qquad (3.25)$$

Using the definition of the experimental low-frequency capacitance C_{LF} given below in Eq. 3.33, we can rewrite Eq. 3.24 to obtain

$$\psi_s(V_G) = \int_{V_F}^{V_G} \frac{C_{ox}}{C_{ox} + C_{it} + C_s}dV = \int_{V_F}^{V_G} \left[1 - \frac{C_{LF}(V)}{C_{ox}}\right]dV, \qquad (3.26)$$

where V_F is the flat-band voltage defined by $\psi_s(V_F) = 0$. Applying Eq. 3.23 yields

$$V_F = -\frac{Q_f}{C_{ox}} - \frac{Q_{it}(0)}{C_{ox}} + \phi_{ms}. \qquad (3.27)$$

The flat-band voltage describes the influence of fixed charges or a difference in work functions of silicon and gate metal, which cause a shift in $\psi_s(V_G)$ along the voltage axis. According to Eq. 3.26, the voltage-dependent surface band bending $\psi_s(V_G)$ can be obtained – up to an integration constant related to V_F – by numerical integration, if an experimental or theoretical low-frequency capacitance–voltage (C-V) curve is available. For practical applications, Eq. 3.26 is more conveniently

expressed as [39]

$$\psi_{\mathrm{s}}(V_{\mathrm{G}}) = \psi_0 + \int\limits_{V_{\mathrm{Acc}}}^{V_{\mathrm{G}}} \left[1 - \frac{C_{\mathrm{LF}}(V_{\mathrm{G}})}{C_{\mathrm{ox}}} \right] dV_{\mathrm{G}}, \qquad (3.28)$$

where integration starts at a bias in strong accumulation, where $\mathrm{d}C_{\mathrm{LF}}/\mathrm{d}V_{\mathrm{G}} \approx 0$, and the integration constant ψ_0 is chosen such that $\psi_{\mathrm{s}}(V_{\mathrm{F}}) = 0$.

At flat-band conditions, the silicon surface capacitance is given by $C_{\mathrm{s}}(\psi_{\mathrm{s}} = 0) = \varepsilon_{\mathrm{s}}/\lambda_{\mathrm{D}}$, and accordingly the flat-band capacitance of the MIS capacitor is given by

$$C_{\mathrm{F}} = \left(\frac{1}{C_{\mathrm{ox}}} + \frac{\lambda_{\mathrm{D}}}{\varepsilon_{\mathrm{s}}} \right)^{-1}, \quad \text{with} \quad \lambda_{\mathrm{D}} = \sqrt{\frac{\varepsilon_{\mathrm{s}}}{q\beta N_{\mathrm{dop}}}}, \qquad (3.29)$$

where N_{dop} is the bulk dopant concentration. The flat-band voltage can hence be determined by finding the voltage on an experimental *C-V* curve, where the measured capacitance equals C_{F}.

For a more accurate determination of the flat-band voltage V_{F} and oxide capacitance C_{ox}, experimental high- and low-frequency *C-V* curves are compared to theoretical curves, which are calculated using the extracted values of V_{F}, C_{ox}, and $D_{\mathrm{it}}(\psi_{\mathrm{s}})$. This procedure is iterated, until a good fit between experimental and theoretical curves is obtained. The theoretical silicon surface capacitance $C_{\mathrm{s}}(\psi_{\mathrm{s}})$ is obtained according to Eq. 3.25 as the derivative of the silicon surface charge density Q_{s} given by Eq. 3.13 with respect to ψ_{s}, which yields

$$C_{\mathrm{s}} = \mathrm{sgn}(u_{\mathrm{s}} - u_{\mathrm{b}}) \left(\frac{\varepsilon_{\mathrm{s}}}{\lambda_{\mathrm{i}}} \right) \frac{\sinh u_{\mathrm{s}} - \sinh u_{\mathrm{b}}}{F(u_{\mathrm{s}}, u_{\mathrm{b}})}. \qquad (3.30)$$

If the minority carrier concentration is neglected (for example $n = 0$ in Eq. 3.14 for *p*-type Si), the high-frequency capacitance can be calculated in good approximation from C_{s} in accumulation, depletion, and over a certain range in weak inversion, where minority carrier concentration in the depletion layer is negligibly small compared to the majority carrier

concentration [33, p. 157]. As the minority carrier concentration increases, the simple derivative in Eq. 3.25 becomes invalid, as the number of minority charge carriers does not change with the ac gate voltage variation [40]. In addition, a spatial reorganization of the minority carriers at the silicon surface has to be taken into account [41]. The depletion layer capacitance C_D at high frequencies can be approximated with a maximum error of 1.5 % by the following equations [41]:

$$
C_D(v_s) \approx C_{\text{maj}}(\tilde{v}) = - \left. \frac{\mathrm{d}Q_{\text{s.maj}}(v)}{\mathrm{d}v} \right|_{v=\tilde{v}} \quad \text{with} \quad \tilde{v} = \begin{cases} v_s & v_s \leq v_m \\ v_m & v_s > v_m \end{cases}
$$
(3.31)

where $Q_{\text{s.maj}}$ is calculated from Eq. 3.14 neglecting any minority carrier contributions, and the *matching point* is $v_m = 2.10\, u_b + 1.33$.

For each set of V_F, C_{ox}, and $D_{\text{it}}(\psi_s)$, the theoretical C-V curves are then calculated from C_s and C_D, respectively, using Eq. 3.33, 3.34, $C_{\text{it}}(\psi_s) = qD_{\text{it}}(\psi_s)$, and, integrating Eq. 3.24,

$$
V_G(\psi_s) = \int \frac{C_{\text{ox}} + C_s(\psi_s) + C_{\text{it}}(\psi_s)}{C_{\text{ox}}} \mathrm{d}\psi_s = - \frac{Q_s(\psi_s) + Q_{\text{it}}(\psi_s)}{C_{\text{ox}}} + \psi_s,
$$
(3.32)

with $V_G(0) = V_F$.

3.2.2 Extraction of the interface state density

In capacitance-voltage (C-V) measurements, the interface state density D_{it} is extracted from the contribution of interface traps to the capacitance of the MIS capacitor. A sketch of the sample structure and the corresponding electrical equivalent circuit are shown in Fig. 3.3(a) and (b). The electrical equivalent circuit for a quasi-static measurement, where all interface traps are able to follow the change in gate voltage, is shown in Fig. 3.3(c). At sufficiently high frequencies, interface traps cannot respond to the change in gate voltage and the electric equivalent circuit simplifies to that shown in Fig. 3.3(d). High-frequency curves are typically mea-
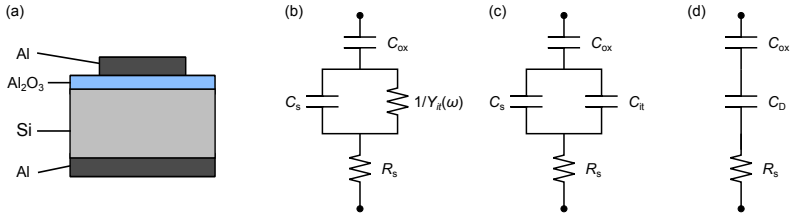
Figure 3.3: (a) Sketch of the sample structure and (b) electrical equivalent circuit of the MIS capacitor. Simplified equivalent circuits for (c) quasi-static and (d) high-frequency capacitance measurements. The symbols are defined in the text.

sured at frequencies of $1\,\mathrm{MHz}$, as higher frequencies are experimentally challenging due to an increasing contribution of series resistance losses and increasing complexity of a sufficiently shielded probe station.

According to the electric equivalent circuits in Fig. 3.3(c) and (d) the quasi-static capacitance C_{QS} and high-frequency capacitance C_{HF} of the MIS capacitor are given by

$$C_{\mathrm{QS}} = \left[\frac{1}{C_{\mathrm{ox}}} + \frac{1}{C_{\mathrm{s}} + C_{\mathrm{it}}}\right]^{-1} \quad \text{and} \tag{3.33}$$

$$C_{\mathrm{HF}} = \left[\frac{1}{C_{\mathrm{ox}}} + \frac{1}{C_{\mathrm{D}}}\right]^{-1} \approx \left[\frac{1}{C_{\mathrm{ox}}} + \frac{1}{C_{\mathrm{s}}}\right]^{-1}, \tag{3.34}$$

where C_{ox} is the gate oxide capacitance, C_{s} is the silicon surface capacitance, C_{it} is the capacitance related to interface traps, and C_{D} is the silicon depletion layer capacitance. The approximation $C_{\mathrm{s}} \approx C_{\mathrm{D}}$ in Eq. 3.34 is not valid in strong inversion, where the inversion layer capacitance significantly contributes to C_{s}, which reduces the energy range over which useful information about the interface state density can be obtained by the analysis of experimental *C-V* curves.

The interface state density D_{it} is obtained from C_{it} by combining experimental quasi-static and high-frequency *C-V* curves, resulting in the

equation

$$qD_{\text{it}} = C_{\text{it}} = \left[\frac{1}{C_{\text{QS}}} - \frac{1}{C_{\text{ox}}} \right]^{-1} - \left[\frac{1}{C_{\text{HF}}} - \frac{1}{C_{\text{ox}}} \right]^{-1}. \qquad (3.35)$$

The resulting interface state density is the sum of the acceptor and donor interface state densities.
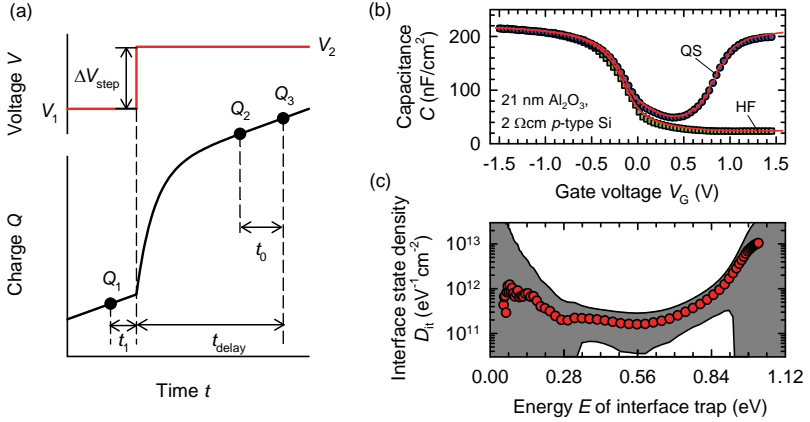
Figure 3.4: (a) Gate voltage (red line on top) and charge (black line on bottom) of the MIS capacitor during one voltage step of ΔV_{step}. The three different charge measurements are indicated as $Q_1, Q_2,$ and Q_3. (b) Exemplary C-V measurement on $2\,\Omega\text{cm}$ p-type Si for $21\,\text{nm}$ of Al_2O_3 deposited by plasma-assisted ALD. Red lines are theoretical C-V curves fitted to the data. (c) Interface state density $D_{\text{it}}(E)$ determined from the measurement in graph (b). The gray area illustrates the uncertainty in D_{it}.

The quasi-static capacitance C_{QS} is not measured directly, but is calculated from charge measurements before and after a step in bias voltage. A schematic of the charge measurements during a step in gate voltage is shown in Fig. 3.4(a). Charge is measured using a feedback-charge method by measuring the change in output voltage of a known feedback capacitor [42]. The charge Q_1 on the MIS capacitor for a gate voltage V_1 is measured shortly before the gate voltage is changed by a small amount

ΔV_{step}. The capacitor is given a time t_{delay} to fully charge up, then the final charge Q_3 is measured at the gate voltage $V_2 = V_1 + \Delta V_{\text{step}}$. The reported capacitance reading is then given by $C_{\text{QS}} = (Q_3 - Q_1)/\Delta V_{\text{step}}$ at a gate voltage $V_{\text{G}} = V_1 + \Delta V_{\text{step}}/2$. This method is very sensitive to leakage currents in the system, which lead to a build-up of charges over time. In order to correct for leakage currents, an additional charge measurement Q_2 is performed at a time t_0 prior to the final charge measurement Q_3. The leakage current is then given by $Q/t = (Q_3 - Q_2)/t_0$ and the capacitance reading can be corrected using

$$C_{\text{QS.corr}} = C_{\text{QS.meas}} - \frac{Q/t}{\Delta V_{\text{step}}} \left(t_{\text{delay}} + t_1 \right). \tag{3.36}$$

For the KEITHLEY 595 QUASISTATIC CV METER used in our setup the timing parameters are $t_1 = 36 \ldots 56 \, \text{ms}$ and $t_0 = t_{\text{delay}}/8$ or $44 \, \text{ms}$, whichever is longer. The delay time t_{delay} is a critical parameter in the *C-V* measurement. On the one hand, it should be short enough to reduce the impact of leakage currents and keep the measurement time short. On the other hand, it needs to be long enough to allow the MIS capacitor to equilibrate at the new gate voltage V_2, which is equivalent to the requirement that the charging transient dQ/dt has vanished by the time the final charge measurements Q_2 and Q_3 are performed. If this requirement is not fulfilled, the leakage current is overestimated, as an additional charging current flows between the measurements of Q_2 and Q_3. Accordingly, the leakage current Q/t can be used to determine whether equilibrium is reached: In thermal equilibrium Q/t is constant over the full gate voltage range (bias-independent leakage current) or a linear function of gate voltage (ohmic shunt through the gate oxide). Furthermore, information about the recombination dynamics can be derived from the charging transient, as shown in Sec. 5.2.3.

A complete voltage sweep from accumulation to inversion, or vice versa, can be obtained within a few minutes, depending on the sweep rate $\Delta V/\Delta t$, measuring quasi-static and high-frequency capacitance at the same time. In order to avoid damage to the c-Si/Al$_2$O$_3$ interface due to

the applied bias voltage, a *virgin $C(V)$* curve is obtained by combining two different measurements – one from $0\,\mathrm{V}$ to accumulation, and one from $0\,\mathrm{V}$ to inversion – on two different contact pads which have previously not been exposed to any bias voltage.

Compared to the analysis of equivalent parallel conductance spectra presented in section 3.3, *C-V* analysis is much faster but less precise [33, p. 320]. In literature, D_{it} distributions determined by *C-V* are often shown over a wide energy range, without taking into account the measurement uncertainties, which significantly limit the accessible energy range. Common measurement uncertainties include [33, p. 345-353]:

Uncertainty of the measured capacitance: The measurement setup was tested with a set of calibrated capacitors. From this data the relative measurement uncertainties in the relevant capacitance range are estimated to be $< 1\,\%$ for C_{HF} and $< 2.5\,\%$ for C_{QS}.

Deviation from a true high-frequency curve: Due to technical limitations, high-frequency curves are rarely measured at frequencies above $1\,\mathrm{MHz}$. Majority trap time constants typically decrease towards the majority carrier band edge, as exemplified in Fig. 5.4 for $\mathrm{Al_2O_3}$. Interface traps can therefore follow the ac gate voltage variation over a part of the gate voltage range, causing an underestimation of D_{it} over the relevant gate voltage range.

Round-off errors: Equation 3.35 requires the subtraction of inverse capacitance values, which leads to large round-off errors if C_{QS} and C_{HF} are nearly equal, or at least one of them is nearly equal to C_{ox}. When calculating the relative uncertainty in C_{it}, the relative uncertainties in C_{QS}, C_{HF}, and C_{ox} are multiplied by factors of the form $x/(1-x)$ or $1/(1-x)$, where x is a ratio $C_{\mathrm{QS}}/C_{\mathrm{ox}}$, $C_{\mathrm{HF}}/C_{\mathrm{ox}}$, or $C_{\mathrm{HF}}/C_{\mathrm{QS}}$. Accordingly, the uncertainty in the extracted value of D_{it} will increase drastically if x approaches unity.

Onset of strong inversion: The approximation $C_{\mathrm{s}} \approx C_{\mathrm{D}}$ in Eq. 3.34, and hence Eq. 3.35, becomes invalid if the silicon surface is inverted.

The corresponding overestimation of D_{it} is negligible in weak inversion, but rapidly increases in strong inversion ($\psi_s > 2\phi_b$).

Series resistance: The series resistance mainly plays a role for high frequencies. Although the series resistance can be estimated from the experimental data, and the high-frequency *C-V* curve can be corrected, deviations occur mainly in a voltage range where C_{HF} is large and round-off error are significant. Hence, no meaningful information about the D_{it} distribution can be extracted anyway in an energy range, where series resistance contributions are significant.

All these measurement uncertainties can be estimated from a theoretical description of the MIS capacitance and are taken into account whenever uncertainty values are provided for D_{it} values in this work. Figure 3.4(b) shows an exemplary *C-V* measurement on $2\,\Omega$cm *p*-type Si for $21\,$nm of Al_2O_3 deposited by plasma-assisted ALD. Red lines are theoretical *C-V* curves fitted to the data according to the procedure described in Sec. 3.2.1. Figure 3.4(c) shows the resulting interface state density $D_{it}(E)$, where the uncertainty in the extracted D_{it} values is illustrated by the gray area. It is worth mentioning that *(i)* around midgap the uncertainty in D_{it} can be one order of magnitude for a typical measurement, and *(ii)* an exponentially increasing D_{it} towards the band edges, often identified as tail-states, is in fact most likely a measurement artifact due to the series resistance (near the majority carrier band edge) or strong inversion (near the minority carrier band edge).

3.3 Admittance spectroscopy

3.3.1 Analysis of equivalent parallel conductance spectra

Figure 3.3(b) shows the electrical equivalent circuit of an MIS capacitor for an arbitrary angular frequency ω. The admittance Y_m of the $Al/Al_2O_3/Si$ capacitor is measured as a function of the angular frequency

ω for a fixed gate bias voltage V_G superimposed by a small ac variation δV. By varying V_G in subsequent measurements, the interface parameters are determined as a function of energetic position in the silicon bandgap given by the surface energy E_s in Eq. 3.17.

In an experiment, only the total admittance of the device under test is accessible, rather than the interface-trap-related admittance Y_{it}. If stray and fringing capacitances and leakage conductances are avoided or reduced, we can identify the measured admittance Y_m with the admittance of the MIS capacitor as shown in Fig. 3.3(b). Converting all capacitances and the series resistance to admittances, and using Kirchhoff's law, we can derive

$$Y_{it} = \left[\frac{1}{Y_m} - R_s - \frac{1}{i\omega C_{ox}}\right]^{-1} - i\omega C_s. \tag{3.37}$$

The equivalent parallel conductance G_p, which is the conductive component of $Y_{it} = G_p + i\omega C_p$, is then extracted from the measured admittance $Y_m = G_m + i\omega C_m$ of the complete system by taking the real part of Eq. 3.37, resulting in the equation [43]

$$G_p = \frac{(G_m^2 + \omega^2 C_m^2)a}{a^2 + \left[\omega C_m - \frac{G_m^2 + \omega^2 C_m^2}{\omega C_{ox}}\right]^2}, \tag{3.38}$$

where $a = G_m - R_s(G_m^2 + \omega^2 C_m^2)$. Knowledge of the silicon capacitance C_s in Eq. 3.37 is not required for the extraction of G_p, as it only adds to the imaginary component of the admittance.

If the MIS capacitor is biased in accumulation, the silicon capacitance C_s and the interface-trap-related admittance Y_{it} can be neglected, and the MIS capacitor is dominated by the oxide capacitance C_{ox}. Thus, the equivalent circuit in Fig. 3.3(b) can be simplified to an $R - C$ circuit as shown in the inset of Fig. 3.5. The series resistance R_s and oxide capacitance C_{ox} can then be obtained by a least-square fit of the predicted total
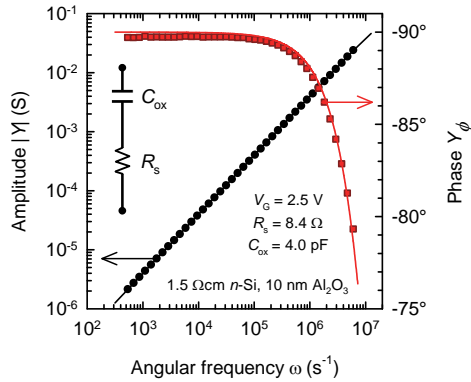
Figure 3.5: Amplitude (black circles) and phase (red squares) of the measured admittance in accumulation. The straight lines are fits assuming the equivalent circuit shown in the inset. The fit parameters are series resistance $R_\mathrm{s} = 8.4\,\Omega$ and oxide capacitance $C_\mathrm{ox} = 4.0\,\mathrm{pF}$.

admittance to a measurement of $Y_\mathrm{m}(\omega)$ in accumulation. The amplitude and phase of $Y_\mathrm{m} = |Y|\,e^{iY_\phi}$ and the respective fit curves are shown in Fig. 3.5 for a typical sample with $R_\mathrm{s} = 8.4\,\Omega$ and $C_\mathrm{ox} = 4.0\,\mathrm{pF}$.

For most samples the phase signal Y_ϕ at low frequencies deviates slightly (fractions of a degree) from the predicted value of $Y_\phi(0) = -90\,^\circ$. This is attributed to a small leakage current through the gate oxide, shunting the oxide capacitance. Taking into account a non-vanishing gate leakage conductance indeed leads to a better agreement between experiment and fit, but only has a negligible impact on the extracted values of R_s and C_ox, and is hence ignored. The gate leakage conductance obtained from the best fit for all samples results in a lower limit of the bulk resistivity of amorphous Al_2O_3 above $3\times10^{11}\,\Omega$cm. In literature, a value of $\approx 10^{16}\,\Omega$cm has been reported for atomic-layer-deposited Al_2O_3 [44], which justifies neglecting the leakage conductance. Only for a sample with $3\,\mathrm{nm}$ of Al_2O_3 we observe a significant contribution of the leakage conductance, which yields $Y_\phi(80\,\mathrm{Hz}) = -80.8\,^\circ$ and corresponds to a bulk

resistivity as low as $(2-3) \times 10^{10}\,\Omega\text{cm}$.
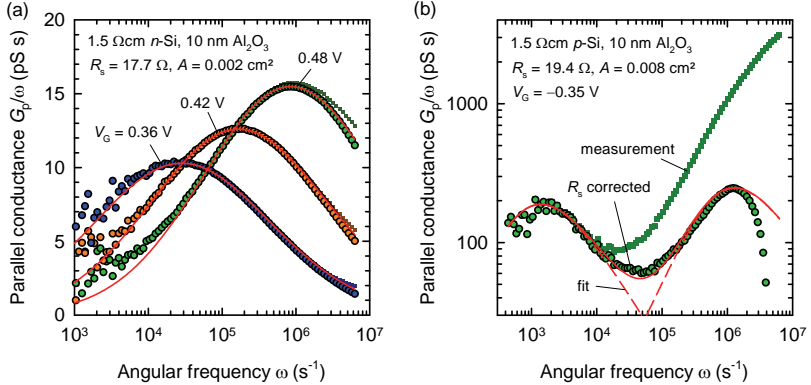
Figure 3.6: (a) Representative plots of the normalized parallel conductance G_{p}/ω as a function of the angular frequency ω for gate voltages of $V_{\mathrm{G}} = 0.36$, 0.42, and 0.48 V on $1.5\,\Omega\text{cm}$ n-type FZ-Si and (b) $V_{\mathrm{G}} = -0.35\,\text{V}$ on $1.5\,\Omega\text{cm}$ p-type FZ-Si for an Al_2O_3 film thickness of 10 nm. Squares show the measurement data, circles are series-resistance-corrected. Red lines are fits of Eq. 3.44 to the series-resistance-corrected measurement data. The data in graph (b) illustrates a second type of defect at low frequencies and a deformation of the peak shape at high frequencies.

Figure 3.6(a) shows exemplary plots of the normalized parallel conductance G_{p}/ω obtained using Eq. 3.38 as a function of the angular frequency ω for three different gate voltages V_{G} on $1.5\,\Omega\text{cm}$ n-type FZ-Si for an Al_2O_3 layer thickness of 10 nm. Similar plots are obtained for other gate voltages within the accessible range, on p-type substrates, as well as for different Al_2O_3 layer thicknesses. The relevant interface recombination parameters, i.e. the interface state density D_{it} and the capture time constant τ_n for electrons (on n-type samples) or τ_p for holes (on p-type samples), respectively, are deduced from the peak of G_{p}/ω versus $\log(\omega)$ by the following equations [33, p.216-218]:

$$D_{\mathrm{it}} = \frac{[G_{\mathrm{p}}/\omega]_{\mathrm{peak}}}{qAf_{\mathrm{D}}(\sigma_{\mathrm{s}})} \tag{3.39}$$

$$\tau_{n/p} = \frac{\xi_{\mathrm{p}}(\sigma_{\mathrm{s}})}{\omega_{\mathrm{peak}}} \tag{3.40}$$

where A is the gate contact area, and f_{D} and ξ_{p} are functions of the surface potential fluctuation σ_{s} explained in the following section. The capture cross sections σ_n and σ_p are related to the capture time constants τ_n and τ_p by the following equations [36]:

$$\sigma_n = (v_{\mathrm{th}}\tau_n n_{\mathrm{s}})^{-1} = (v_{\mathrm{th}}\tau_n n_{\mathrm{i}})^{-1} \exp\left(-\beta[E - E_{\mathrm{i}}]\right) \tag{3.41}$$

$$\sigma_p = \left(v_{\mathrm{th}}\tau_p p_{\mathrm{s}}\right)^{-1} = \left(v_{\mathrm{th}}\tau_p n_{\mathrm{i}}\right)^{-1} \exp\left(+\beta[E - E_{\mathrm{i}}]\right) \tag{3.42}$$

where $v_{\mathrm{th}} = 1 \times 10^{7}$ cm/s is the thermal velocity of the free carriers in silicon, n_{s} and p_{s} are the electron and hole concentrations at the surface, n_{i} is the intrinsic carrier concentration, $\beta = (k_{\mathrm{B}}T)^{-1}$, k_{B} is the Boltzmann constant, and T is the temperature.

3.3.2 Surface potential fluctuations

In a real device, the experimental data typically cannot be quantitatively reproduced by the G_{p}/ω versus $\log(\omega)$ curves calculated for the expected values of the surface band bending. This can be attributed to a spatially non-uniform surface band bending, e.g. caused by non-uniformities in the thickness of the gate oxide or by a non-homogeneous distribution of fixed charges at the interface. Although the exact surface potential fluctuation is typically unknown, a Gaussian distribution with standard deviation σ_{s} around the mean value of surface band bending $\bar{v}_{\mathrm{s}}$ is a reasonable estimate, as the fluctuations result from a random distribution of a large number of atoms or charges and hence are expected to follow a normal distribution. The distribution function $P(v_{\mathrm{s}})$ of the local surface band bending v_{s} is then given by:

$$P(v_{\mathrm{s}}) = \frac{1}{\sqrt{2\pi\sigma_{\mathrm{s}}^2}} \exp\left(-\frac{1}{2}\left[\frac{v_{\mathrm{s}} - \bar{v}_{\mathrm{s}}}{\sigma_{\mathrm{s}}}\right]^2\right). \tag{3.43}$$

Note that, for simplicity, ψ_{s} rather than $\bar{\psi}_{\mathrm{s}}$ is used in this thesis to denote the mean value of the surface band bending $\bar{v}_{\mathrm{s}}/\beta$.

As interface trap time constants usually strongly vary with energy, and hence with the local value of the surface band bending, a spatially non-uniform surface band bending leads to a significant interface trap time constant dispersion in the measurement. As a result, the peak of G_{p}/ω vs $\log(\omega)$ is broadened, shifted to higher frequencies, and the peak value of G_{p} is reduced in the presence of surface potential fluctuations compared to a spatially homogeneous surface potential. As the G_{p}/ω vs $\log(\omega)$ peak is broadened by surface potential fluctuations, σ_{s} can be determined experimentally by calculating a theoretical conductance curve for a given surface band bending, folding it with the Gaussian distribution given by Eq. 3.43, and fitting the resulting curve to the experimental data. In depletion, G_{p}/ω averaged over the Gaussian distribution of the surface potential is described by the following equation [33, p.211-212]:

$$\begin{aligned} \left\langle \frac{G_{\mathrm{p}}}{\omega} \right\rangle &= \frac{q}{2} \int_{-\infty}^{\infty} \frac{D_{\mathrm{it}}}{\omega\tau} \ln\left(1 + \omega^2\tau^2\right) P(v_{\mathrm{s}}) \mathrm{d}v_{\mathrm{s}} \\ &= \frac{qD_{\mathrm{it}}}{2\omega\tau\sqrt{2\pi\sigma_{\mathrm{s}}^2}} \int_{-\infty}^{\infty} \exp\left(-\frac{\eta^2}{2\sigma_{\mathrm{s}}^2} - \eta\right) \ln\left(1 + \omega^2\tau^2 e^{2\eta}\right) \mathrm{d}\eta, \end{aligned} \tag{3.44}$$

where $\eta = v_{\mathrm{s}} - \bar{v}_{\mathrm{s}}$, and where we assume that the interface state density D_{it} and the capture cross sections $\sigma_{n/p}$ do not vary significantly over an energy range of a few $k_{\mathrm{B}}T$. Figure 3.6 shows an excellent agreement of theoretical and experimental G_{p}/ω curves for most measurements. However, the analysis fails if series resistance losses become too large and uncertainties in R_{s} obscure the peak shape, as exemplified by the second peak around $\omega \approx 10^6\,\mathrm{s}^{-1}$ in Fig. 3.6(b).

This integration and fitting procedure can be simplified significantly: The ratio of G_p/ω values taken at the peak frequency ω_{peak} and a multiple $n\omega_{\text{peak}}$ defines the peak shape and is independent of the actual interface trap parameters. Hence, this ratio can be calculated once from Eq. 3.44 as a function of σ_s, and the resulting tabulated values can then be used to obtain σ_s from the experimental data. Figure 3.7(a) shows this ratio for multiples of $n_1 = 5$ and $n_2 = 1/5$.
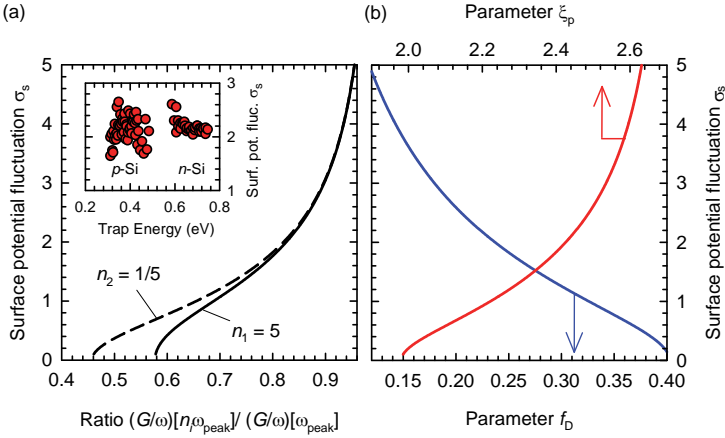
Figure 3.7: (a) Dependence of the ratio of G_p/ω values taken at the peak frequency ω_{peak} and a multiple $n\omega_{\text{peak}}$ on the standard deviation σ_s of the surface potential distribution, for multiples of $n_1 = 5$ and $n_2 = 1/5$. The inset shows σ_s values determined for $Al/Al_2O_3/c$-Si capacitors. (b) Correction factors f_D and ξ_p in Eq. 3.39 and 3.40 as a function of σ_s.

Typical values of σ_s for an $Al/Al_2O_3/c$-Si capacitor are shown in the inset in Fig. 3.7(a). We obtain values of $\sigma_s/\beta = 54 \pm 7\,\text{mV}$ on p-type and $57 \pm 3\,\text{mV}$ on n-type samples, respectively. A spatially inhomogeneous fixed charge density Q_f due to randomly distributed charges in the Al_2O_3 is one possible cause of a non-uniform surface potential. These σ_s values then correspond to a standard deviation of the distribution of the fixed charge density of $\sigma_{Q.f} < 2 \times 10^{11}\,\text{cm}^{-2}$, which is at least one order of magnitude lower than typical values of $Q_f = -4 \times 10^{12}\,\text{cm}^{-2}$ for Al_2O_3

on c-Si.

When extracting D_{it} and $\tau_{n/p}$ from a conductance measurement, the correction factors $f_{\text{D}}(\sigma_{\text{s}})$ and $\xi_{\text{p}}(\sigma_{\text{s}})$ in Eq. 3.39 and 3.40 account for the change of the peak shape in the presence of surface potential fluctuations. Both $f_{\text{D}}(\sigma_{\text{s}})$ and $\xi_{\text{p}}(\sigma_{\text{s}})$ are known functions of σ_{s}, which can be calculated numerically [33, p. 207-217] and, for realistic values of σ_{s}, have values in the range of $f_{\text{D}} = 0.15 - 0.35$ and $\xi_{\text{p}} = 2.0 - 2.5$, as shown in Fig. 3.7(b). The plots in Fig. 3.7 can be used to first obtain σ_{s} from the ratio of experimental G_{p}/ω values at two frequencies ω_{peak} and $n\omega_{\text{peak}}$, and then obtain the parameters f_{D} and ξ_{p} for the determined σ_{s}, which are in turn used to calculate D_{it} and $\tau_{n/p}$ using Eq. 3.39 and 3.40.

3.3.3 Measurement range and uncertainty

The energy range in the silicon bandgap accessible by the $G_{\text{p}}(\omega)/\omega$ analysis extends roughly between $2\,k_{\text{B}}T$ from midgap to within $2\,k_{\text{B}}T$ from the bulk Fermi level, and the conductance signal is dominated by the majority carrier time constant [43]. Therefore, both n- and p-type samples are required to cover both halves of the bandgap. In addition, upper and lower limits to the detectable capture time constants $\tau_{n/p}$ are given by constraints on the corresponding peak frequency $\omega_{\text{peak}} = \xi_{\text{p}}(\sigma_{\text{s}})/\tau_{n/p}$ in our experimental setup. On the one hand, for large capture time constants, and accordingly low peak frequencies, the conductance G_{p} is small and affected by low-frequency noise and leakage currents through the gate oxide. On the other hand, capture time constants below $3.5 \times 10^{-7}\,\text{s}$ cannot be resolved in our experimental setup, as the corresponding peak frequency lies above the maximum measurement frequency of $1\,\text{MHz}$.

Furthermore, at high frequencies the measured conductance signal is large, and inaccuracies in the measurement or in the correction for series resistance have a large impact on the shape of the G_{p}/ω peak. For the exemplary set of data shown in Fig. 3.6(a), the series resistance correction only leads to a minor change in the peak position and shape, and interface

recombination parameters can be extracted with great accuracy. For the data shown in Fig. 3.6(b), however, the second peak around $\omega \approx 10^6\,\text{s}^{-1}$ is obscured in the raw data due to dominant series resistance losses. Accordingly, the corrected data is highly sensitive to the exact value of the series resistance. This masks the real dependence of ω_{peak} on gate bias, and yields apparent capture time constants near the detection limit, which are practically independent of energy. As a consequence, the apparent capture cross-sections seem to decrease exponentially with energy, following the exponential factor in Eq. 3.41 and 3.42. In order to avoid such misinterpretation, we disregard all data where the experimental and the numerically computed peak shapes deviate significantly. The standard deviation σ_{s} of the surface potential distribution provides a good estimate: the data is discarded if σ_{s} evaluated according to Fig. 3.7(a) differs by more than $10\,\%$ between using multiples of $n_1 = 5$ and $n_2 = 1/5$.

In order to convert the applied gate voltage V_{G} into the energy level E within the silicon bandgap, $\psi_{\text{s}}(V_{\text{G}})$ is calculated from an experimental or theoretical $C\text{-}V$ curve according to Eq. 3.28 or 3.32. Due to the exponential dependence of capture cross section $\sigma_{n/p}$ on energy E, and hence ψ_{s}, in Eq. 3.41 and 3.42, the capture cross sections can typically only be determined with an accuracy of one order of magnitude.

3.4 Corona charge analysis

The fixed charge density Q_{f} in a dielectric layer, for example Al_2O_3, can be probed by means of a corona charge experiment [45]. Figure 3.8(a) shows a sketch of a typical corona charge setup. A voltage of $\pm(7-8)\,\text{kV}$ is applied between the sample and a needle above the sample. Air molecules are ionized and accelerated in the electric field, which leads to the deposition of corona charges onto the sample surface, thereby varying the surface potential ψ_{s}. In a corona charge experiment, Eq. 3.15 has to be extended to include the deposited corona charge density Q_{c}. Accordingly, the corona charge density required to obtain a given band
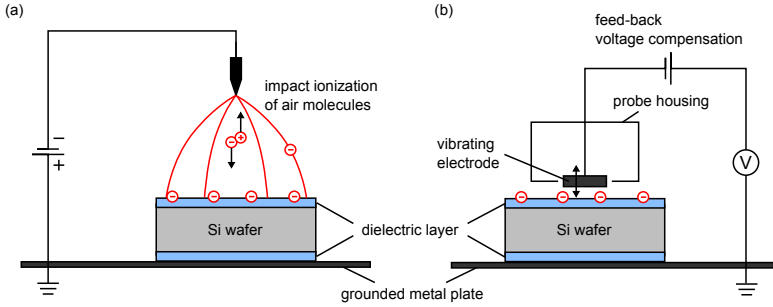
Figure 3.8: (a) Schematic drawing of the corona charge setup applied in this study. Air molecules are ionized in an electric field and deposited unto the sample surface. (b) Schematic drawing of an electrostatic Kelvin probe setup. A feedback circuit drives the probe housing towards the same potential as the sample surface.

bending ψ_s is given by the equation

$$Q_\mathrm{c} = - \left[Q_\mathrm{f} + Q_\mathrm{s}(\psi_\mathrm{s}) + Q_\mathrm{it}(\psi_\mathrm{s}) \right]. \tag{3.45}$$

Analogous to Eq. 3.23, the surface voltage V_s relative to the bulk Fermi level in the presence of deposited corona charges is then given by

$$V_\mathrm{s}(\psi_\mathrm{s}) = \frac{q Q_\mathrm{c}(\psi_\mathrm{s})}{C_\mathrm{ox}} + \psi_\mathrm{s}. \tag{3.46}$$

In order to reproduce a corona charge experiment, ψ_s is varied over a wide range, and Eq. 3.45 and 3.46 are evaluated for each value of ψ_s to obtain $V_\mathrm{s}(Q_\mathrm{c})$.

The surface voltage, and hence – indirectly – the deposited corona charge density, can be monitored experimentally relative to a reference surface using a Kelvin probe [46] (TREK 320C [47]). A schematic drawing of the electrostatic Kelvin probe used in this study is shown in Fig. 3.8(b). In order to measure the surface voltage on the sample, a vibrating electrode

is brought in close proximity to the sample surface. In the presence of any potential difference between sample surface and probe housing, which serves as reference surface, the modulated capacitance between sample and vibrating electrode induces an ac signal on the electrode. In a feed-back circuit, the probe housing is driven towards the same potential as the sample surface, at which point the induced ac signal vanishes. As the Kelvin probe measures the surface voltage *relative* to a sample surface, the Kelvin probe reading is typically adjusted to zero on the sample surface prior to the deposition of corona charges. Thus, the determined surface voltage after corona deposition corresponds to the change in surface voltage caused by the deposited corona charges. Accordingly, calculated values of V_s according to Eq. 3.46 need to be shifted to fulfill $V_s(Q_c = 0) = 0$.

In our corona charge experiments [45], corona charges are successively deposited onto both sides of a passivated lifetime sample, and the effective surface recombination velocity S_{eff} is determined after each charging step by means of a photoconductance measurement. As the deposited corona charges gradually compensate the fixed charge density Q_f in the passivation layers and reduce the surface band bending, and hence the field-effect passivation, S_{eff} increases significantly. A maximum of S_{eff} is observed for $n_s\sigma_n = p_s\sigma_p$ [45], where n_s and p_s are the electron and hole concentrations at the surface, and σ_n and σ_p are the electron and hole capture cross sections. For typical samples, the fixed charge density Q_f can directly be identified with the corona charge density Q_{peak} at which the maximum value of S_{eff} is observed, that is $Q_f = -Q_{peak}$, with a minor error of $\Delta Q < \left(Q_{it} + 10^{11} \text{ cm}^{-2}\right)$ [45]. Alternatively, a fit of a calculated $V_s(Q_c)$ curve to experimental data allow a more precise determination of the fixed charge density independent of the capture cross sections.

Figure 3.9 shows an exemplary corona charge measurement for 5 nm of Al_2O_3 deposited by plasma-assisted ALD on 1.5 Ωcm p-Si. Figure 3.9(a) shows the surface voltage V_s measured using a Kelvin probe (solid symbols) as a function of the number of successive corona charging steps,
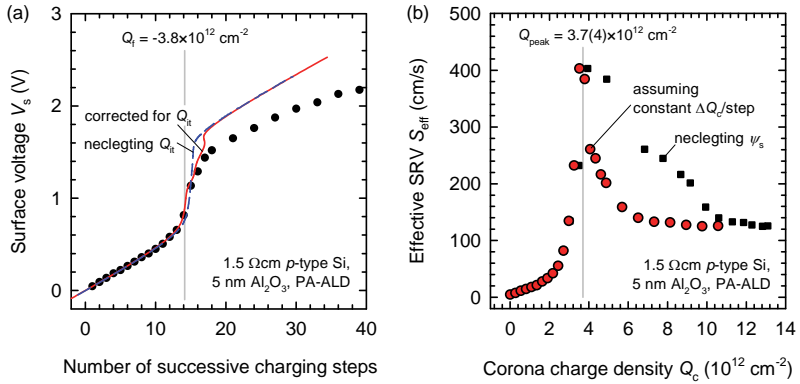
Figure 3.9: (a) Surface voltage V_s as a function of the number of successive corona charging steps measured for 5 nm of Al_2O_3 deposited by plasma-assisted ALD on $1.5\,\Omega$cm p-Si (solid symbols). The red solid line is a best fit of calculated V_s values to the experimental data, where the interface-trapped charge Q_{it} is calculated from experimental D_{it} values. The flat-band condition is indicated by the gray line, the resulting fixed charge density is $Q_f = -3.8 \times 10^{12}\,cm^{-2}$. For the blue dashed line Q_{it} is neglected. (b) Effective SRV S_{eff} as a function of deposited corona charge density Q_c for the data shown in graph (a), where Q_c is calculated according to Eq. 3.46 neglecting ψ_s (black squares), or by assuming a constant charging rate ΔQ_c/step (red circles). For the latter the maximum value of S_{eff} is observed at $Q_{peak} = (3.7 \pm 0.4) \times 10^{12}\,cm^{-2}$.

as well as best fits of calculated V_s values to the experimental data (lines) with and without taking into account the interface-trapped charge Q_{it}. The best fit yields a fixed charge density of $Q_f = -3.8 \times 10^{12}\,\mathrm{cm}^{-2}$, which is obtained from the location of the flat-band point on the calculated curve. Figure 3.9(b) shows the effective SRV S_{eff} as a function of deposited corona charge density Q_c. A fixed charge density of $Q_f = -(3.7 \pm 0.4) \times 10^{12}\,\mathrm{cm}^{-2}$ is obtained from the peak of $S_{eff}(Q_c)$. For the Al_2O_3-passivated samples analyzed in this study the surface band bending ψ_s in Eq. 3.46 cannot be neglected and Q_s is not a linear function of the surface voltage V_s. In a corona charge experiment, Q_s is most conveniently calculated assuming a constant corona charge density ΔQ_c deposited during each charging step [red circles in Fig. 3.9(b)]. The value of ΔQ_c is either calculated from the change ΔV_s in surface voltage for the first few measurements of the experiment, where ψ_s does not change significantly, or is determined on a reference sample with a small oxide capacitance C_{ox}, in which case ψ_s in Eq. 3.46 can be neglected.

The level of chemical passivation at the interface is given by the *surface recombination velocity parameter* S_0 for zero net charge, which is identified with the maximum of S_{eff}. For a better comparison, the S_0 values can be scaled to a true interface state density D_{it} by means of a *C-V* measurement of a reference sample. However, due to the non-homogeneous distribution of the fixed charge density and of the deposited corona charge density, as observed for example in Fig. 4.9, corona experiments typically underestimate the value of S_0. Simulations of the effective SRV S_{eff} as a function of surface charge density $Q_\Sigma = Q_f + Q_c$ presented in Sec. 5.3 show that for typical PA-ALD-Al_2O_3-passivated samples and for an excess carrier density of $\Delta n = 10^{15}\,\mathrm{cm}^{-3}$ the true value of S_0 is underestimated by a factor of $1.5 - 5$ due to spatially inhomogeneous distributions of Q_f and Q_c.

4 Model of the c-Si/Al$_2$O$_3$ interface

4.1 Structural properties of the c-Si/Al$_2$O$_3$ interface

A thin $(1-2\,\text{nm})$ interfacial layer of SiO$_x$ had previously been reported at the c-Si/Al$_2$O$_3$ interface [3] and is considered to play an important role in the passivation of silicon surfaces with Al$_2$O$_3$ layers [4, 18]. In order to directly verify the presence of such an interfacial SiO$_x$ layer, in this thesis the c-Si/Al$_2$O$_3$ interface was examined by cross-sectional transmission electron microscopy (*TEM*). The Al$_2$O$_3$ layer under investigation has a thickness of 30 nm and has been deposited by plasma-assisted ALD on a shiny-etched non-polished $1.5\,\Omega$cm (100)-oriented *p*-type FZ-Si wafer and subsequently annealed for 15 min at 425 °C in a nitrogen ambient. Figure 4.1(a) shows a bright-field TEM image of the Al$_2$O$_3$ layer on top of the c-Si wafer, details of the Si/Al$_2$O$_3$ interface morphology are revealed by a high-resolution (*HR-*) TEM image shown in Fig. 4.1(b).

The interface shows a roughness at the nanometer scale, which is typical for RCA-cleaned Si(100) surfaces [48]. The pronounced bright-dark contrast within the c-Si wafer near the interface is attributed to tension within the silicon. It is not clear, however, whether this is due to the Al$_2$O$_3$ deposition, etching of the surface during the wafer fabrication, or if it related to thermal stress due to a difference in the coefficients of thermal expansion of Si and Al$_2$O$_3$. A bright feature at the Si/Al$_2$O$_3$ interface – which in previous studies [3] might have been mistakenly interpreted as a thin interfacial SiO$_x$ film of a few nanometers – can be seen in the low-magnification image in Fig. 4.1(a). This feature is caused by pronounced Fresnel diffraction resulting from a large step of the projected scattering potential in the rather thick part of the TEM foil imaged
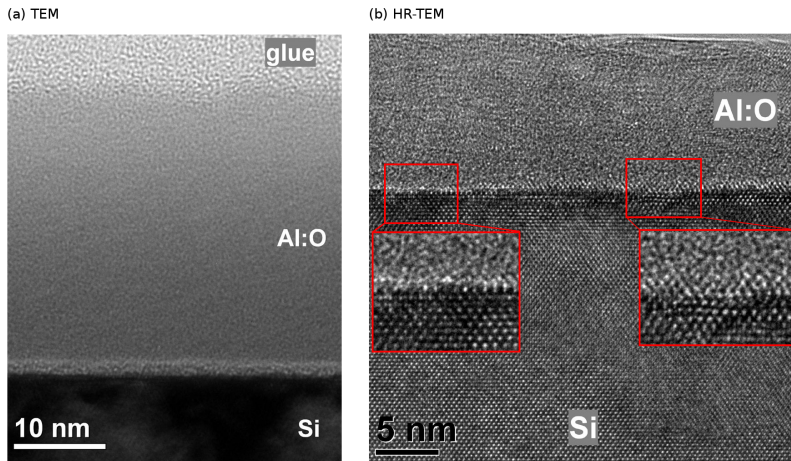
Figure 4.1: (a) Bright-field TEM image of a 30 nm thick Al$_2$O$_3$ layer deposited on c-Si by plasma-assisted ALD. The Al$_2$O$_3$ layer was annealed for 15 min at 425 °C. (b) High-resolution TEM image of the same Al$_2$O$_3$ layer. The insets show magnifications of the interface region at atomic scale.

here [49]. The complete absence of any structural contrast in HR-TEM images of this region [Fig. 4.1(b)] refutes the presence of a noticeable interfacial SiO$_x$ layer with a thickness of the order of a few nanometers. The presence of only a few monolayers of SiO$_x$ at the interface, however, cannot be excluded on the basis of present TEM data.
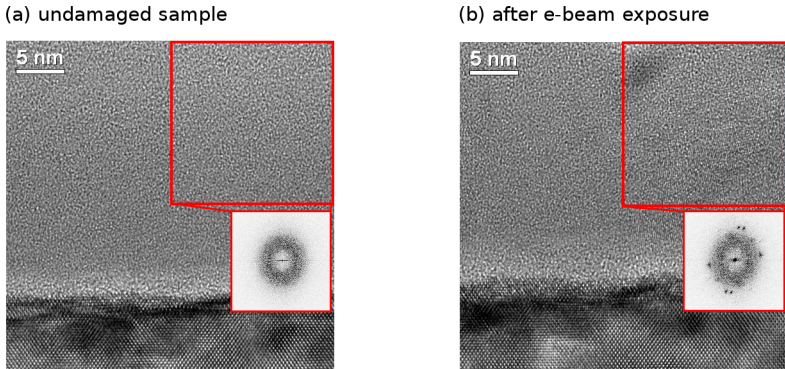
Figure 4.2: TEM images of an annealed 30 nm thick Al$_2$O$_3$ layer deposited on c-Si by plasma-assisted ALD (a) with short exposure time before recording the image and (b) after 3 min of exposure to the 200 keV electron beam. Insets show the Fourier transformation of the marked region in the respective TEM image.

The Al$_2$O$_3$ layer is clearly shown to be amorphous, which is corroborated by the feature-less pattern of the Fourier transformation of an area of the TEM image shown in Fig. 4.2(a). It is worth mentioning, however, that nanocrystalline regions were observed in the Al$_2$O$_3$ after 3 min of exposure to the 200 keV TEM electron beam, as exemplified by the Fourier transformation shown in Fig. 4.2(b). Although this effect can be completely avoided by keeping the exposure time before recording an image in the TEM short, it might indicate that the amorphous Al$_2$O$_3$ films are susceptible to phase changes due to external energy supply.

4.2 Chemical composition of the c-Si/Al₂O₃ interface

4.2.1 X-ray photoelectron spectroscopy

X-ray photoelectron spectroscopy (*XPS*) is a highly sensitive tool to analyze the electronic structure and chemical composition even of very thin films of the order of a few tenths of a nanometer. XPS is highly surface sensitive due to the short inelastic mean free path length of the photoelectrons, which is below 3.5 nm in c-Si and amorphous Al₂O₃ [50–52] for kinetic energies up to 1.5 keV.

A polished c-Si wafer coated with an aluminum oxide layer deposited by plasma-assisted ALD is introduced to ultra-high vacuum and irradiated with monochromatic Mg K_α X-ray photons with an energy of 1253.6 eV. The kinetic energy of photo-generated electrons released from the sample depends, among other parameters, on the binding energy E_B of the orbital from which the electron was released. Orbitals in the inner electronic shells of an atom do not participate in the formation of chemical bonds and hence exhibit discrete energy levels (*core-levels*), rather than forming continuous energy bands like valence orbitals. The exact binding energy E_B of a core-level, however, depends on the chemical environment and the valence state of the atom [53]. By means of a precise energy calibration and a peak-fitting procedure to find the constituent components of recorded core-level peaks, it is possible to identify the chemical compounds present in a sample. For a quantitative determination of the chemical composition, the different photoemission cross-sections of different atomic species and different orbitals need to be taken into account. For this, the raw XPS intensity originating from a given core-level orbital is normalized by an atomic sensitivity factor (*ASF*), which is calculated from properties of the core-level orbital and the XPS detection system [54]. If a sample contains atomic species $x, y, z, ...$ with integrated peak intensities $I_{p.i}$ and ASF S_i, the relative atomic concentration c_x of species

x is given by

$$c_x = \frac{I_{\mathrm{p}.x}/S_x}{\sum_{x,y,z,\ldots} I_{\mathrm{p}.i}/S_i}. \tag{4.1}$$

In the following, XPS peaks are denoted by e.g. Si-2p[SiO$_2$], which refers to a sub-peak of the Si-2p core-level, which is attributed to a silicon atom bound as SiO$_2$.

A detailed investigation of the atomic sensitivity factors is beyond the scope of this thesis and we rely on ASF values published in Ref. 54. For Al$_2$O$_3$ layers with a thickness of 15 nm we determine an aluminum-to-oxygen atomic ratio of 0.63 ± 0.04 [compare Fig. 4.4(b)], which is in excellent agreement with the stochiometric value of 2/3 and with values of 0.66 ± 0.07 reported by other groups [10, 55] for comparable ALD-Al$_2$O$_3$ layers. Hence, we only expect a minor influence of any uncertainties in the chosen ASF values.

A thickness-dependent analysis of the chemical composition is presented here by varying the number of ALD cycles for the deposition of the Al$_2$O$_3$ films (0, 1, 5, 30 and 125 cycles). In addition, the sample preparation (HF dip prior to deposition/no HF dip) and post-deposition anneal (annealed in forming gas/not annealed) are varied.

A pronounced energy-resolved silicon signal can only be observed for thin Al$_2$O$_3$ films below a few nanometers, where scattering of photoelectrons originating from the Si/Al$_2$O$_3$ interface is negligible. On these samples the silicon core-level peaks show a distinct double-peak structure, as exemplified by the Si-2p core-level peak for 5 ALD cycles of Al$_2$O$_3$ shown in Fig. 4.3(a). Besides the bulk silicon signal at a binding energy of 99.4 eV [54], a second peak is observed for all samples at a binding energy of 102.9 eV, which is attributed to Si-O bonds [54]. This clearly indicates an oxidation of the silicon surface, forming a SiO$_x$ interface between the silicon and aluminum oxide. The thickness of the interfacial SiO$_x$ is estimated by the relative contributions of the Si−Si and Si−O signals to the Si-2p double-peak. We assume an ideal stack with a homogeneous SiO$_x$ layer on a semi-infinite Si wafer, and a planar and abrupt interface. Due

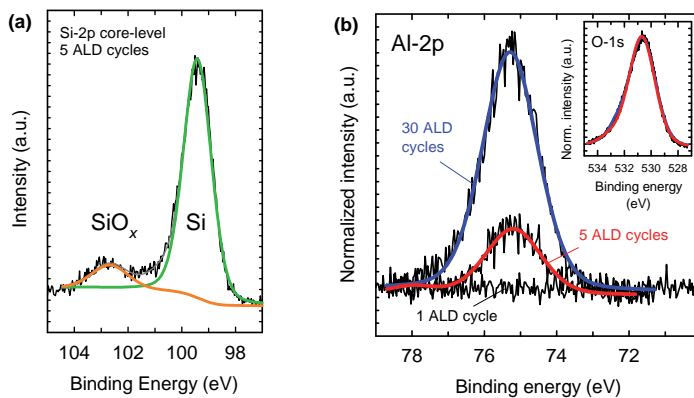**Figure 4.3:** (a) Si-2p core-level peak for 5 cycles of ALD-Al$_2$O$_3$ showing a small second peak attributed to an interfacial SiO$_x$. (b) Al-2p core-level peak, and oxygen O-1s in the inset, after 1, 5, and 30 ALD cycles, respectively. The intensities were normalized to yield the same O-1s peak intensity. Solid lines correspond to results of an XPS peak fitting procedure applied to the data.

to scattering of the photoelectrons within the sample, the XPS intensity originating from a depth x is attenuated by a factor of $\exp(-x/\lambda)$, where λ is the inelastic mean free path of the photoelectron. Using Mg K_α X-ray photons, the kinetic energy of a photoelectron from the Si-2p core-level is approximately $1150\,\text{eV}$, and $\lambda = 2.0 - 2.2\,\text{nm}$ in Si and amorphous SiO$_x$ [52]. The ratio of the recorded peak intensities of the Si-2p[SiO$_x$] and Si-2p[Si] peaks is obtained by integrating the emitted photoelectrons over the depth in the semi-infinite Si wafer, and in a layer of SiO$_x$ with a thickness of d_ox, which yields

$$\frac{I_\text{p}(\text{Si-2p}[\text{SiO}_x])}{I_\text{p}(\text{Si-2p}[\text{Si}])} = \frac{\lambda_{\text{SiO}_x}}{\lambda_\text{Si}} \frac{1}{\gamma} \left[e^{\frac{d_\text{ox}}{\lambda_{\text{SiO}_x}}} - 1 \right], \tag{4.2}$$

where the factor $\gamma = 1.5 - 2.0$ accounts for the different densities of Si atoms in crystalline Si and amorphous SiO$_x$. Solving Eq. 4.2 for the thickness d_ox of the interfacial SiO$_x$ yields the equation

$$d_\text{ox} = \lambda_{\text{SiO}_x} \ln \left[\gamma \frac{\lambda_\text{Si}}{\lambda_{\text{SiO}_x}} \frac{I_\text{p}(\text{Si-2p}[\text{SiO}_x])}{I_\text{p}(\text{Si-2p}[\text{Si}])} + 1 \right]. \tag{4.3}$$

Figure 4.4(a) shows the resulting value of d_ox as a function of the number of ALD cycles for non-annealed (black triangles down) and annealed (red triangles up) samples. The interfacial SiO$_x$ grows during the Al₂O₃ deposition from an initial value of approximately $0.5\,\text{nm}$ to more than $1\,\text{nm}$. This is in contrast to the TEM image in Fig. 4.1(b), where such a thick interfacial layer could not be resolved. A possible explanation might be a non-ideal stack system with a gradual transition from SiO$_x$ to Al₂O₃, which would reduce the contrast in the TEM image. Remarkably, an HF-dip directly before the Al₂O₃ deposition only has a negligible impact on the final thickness of the interfacial SiO$_x$. Although a slightly thicker layer of SiO$_x$ is observed for ultra-thin films of AlO$_x$ (1 and 5 cycles) when annealing the samples after deposition, compared to non-annealed samples, no more differences are observed for 30 ALD cycles. Note that Gao *et al.* [56, 57] have concluded that at least part of the SiO$_x$ is in fact located at the Al₂O₃ *surface*, not at the c-Si/Al₂O₃ interface, which

would drastically alter the thickness values presented in Fig. 4.4(a). At temperatures below 600 °C, however, the diffusion of Si atoms through the Al_2O_3 layer is negligible [58], and we neglect any SiO_x contributions from the surface of the Al_2O_3.

(a)

(b)
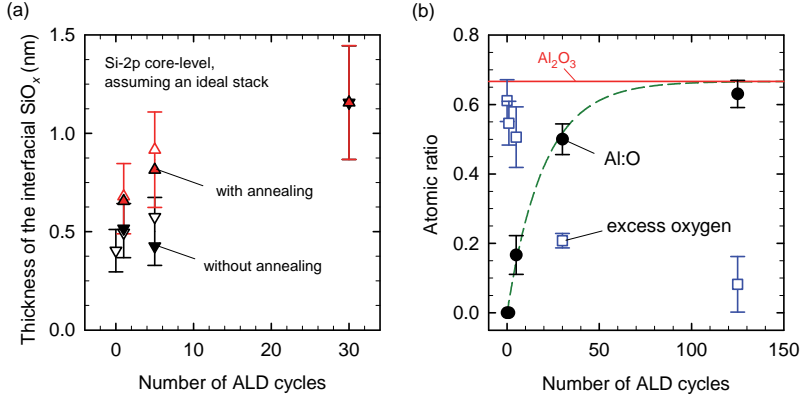
Figure 4.4: (a) Thickness d_{ox} of the interfacial SiO_x layer as a function of the number of ALD cycles for non-annealed (black triangles down) and annealed (red triangles up) samples. Solid symbols represent a final HF-dip, open symbols are without HF-dip. (b) Ratio Al:O of aluminum and oxygen atoms (black circles) detected by XPS as a function of the number of ALD cycles. The value of Al:O = 2/3 for stochiometric Al_2O_3 is given as reference (red line), the dashed green line is an exponential fit to the data. Blue open squares show the fraction of excess oxygen atoms defined in Eq. 4.4.

Equation 4.3 is independent of the thickness of the growing AlO_x film, as all contributions to the Si-2p peak are attenuated by the same amount. The integrated Si-2p peak intensity is found to decay exponentially, which indicates the growth of a closed layer. In contrast to this, an initial island growth during the first 10 ALD cycles was observed for Al_2O_3 deposited by thermal ALD by Naumann *et al.* [55]. From the decay of the integrated Si-2p peak intensity as a function of the number of deposited ALD cycles, assuming a constant growth per cycle of 0.121 nm/cycle, we deduce an inelastic mean free path length in AlO_x of approximately 1.9 nm at a

kinetic energy of 1150 eV. This value is slightly below the literature value of $2.3 - 2.4$ nm calculated for amorphous Al_2O_3 [50], but agrees well with the recently re-evaluated inelastic mean free path length in crystalline Al_2O_3 of 2.0 nm [52].

The aluminum Al-2p and oxygen O-1s core-level peaks are shown in Fig. 4.3(b) after 1, 5, and 30 ALD cycles, respectively. The samples had been HF-dipped prior to deposition and were annealed at 425 °C for 15 min in forming gas. For better comparison, the intensities were normalized to yield the same O-1s peak intensity. For samples coated with only one ALD cycle no aluminum is detected at all, indicating that at least one "starting cycle" is required to generate a suitable nucleation surface for the ALD process. With increasing number of ALD cycles, the aluminum to oxygen ratio increases.

Figure 4.4(b) shows the ratio Al:O of aluminum and oxygen atoms (black circles), which is calculated according to Eq. 4.1 using the Si-2p, O-1s, and Al-2p integrated peak intensities, as a function of the number of ALD cycles. The large uncertainty mainly originates from the difficulty of unambiguously differentiating between oxygen contributions from the AlO_x layer, the interfacial SiO_x layer, and oxygen physisorbed at the surface, especially if sub-oxides other than SiO_2 and Al_2O_3, or hydroxides, are involved. In addition, the oxygen concentration is slightly different for annealed and non-annealed samples. Possible uncertainties in the ASFs used in Eq. 4.1 are not taken into account. Blue open squares in Fig. 4.4(b) show the fraction of excess oxygen, which is not bound to Si or Al, assuming stochiometric SiO_2 and Al_2O_3 layers. The excess oxygen is calculated according to

$$\text{excess O} \equiv \frac{c_O - 2c_{Si.ox} - \frac{3}{2}c_{Al}}{c_O}, \tag{4.4}$$

where the oxygen, oxidized silicon, and aluminum concentrations c_i are calculated from the O-1s, Si-2p[SiO_x], and Al-2p peaks, respectively. Figure 4.4(b) demonstrates that, independent of sample preparation, thin layers of atomic-layer-deposited aluminum oxide are extensively oxygen-

rich. For thin AlO$_x$ layers below 1 nm approximately half of the detected oxygen is not stochiometrically bound as SiO$_2$ or Al$_2$O$_3$. These findings agree well with measurements of the dielectric constant ε_r presented in section 4.2.2, which show that the c-Si/Al$_2$O$_3$ interface can be well described by introducing a thin interfacial SiO$_2$ and a transition region between c-Si and Al$_2$O$_3$. Our results are confirmed by recent XPS studies by Naumann *et al.* [55] for Al$_2$O$_3$ deposited by thermal ALD, who find a similar amount of excess oxygen near the interface.

The reduced aluminum concentration in the deposited films at the beginning of the ALD process leads to the conclusion that in the native state or after an HF dip the functional surface groups on the silicon wafer are not optimal for an adsorption of the TMA precursor molecules. This leads to an incomplete reaction of the TMA and, consequently, an increased relative oxygen concentration at the interface. In fact, it has been shown that more than half of all Si–H bonds at an initially H-terminated surface might remain after thermal ALD [56]. The incomplete ALD process during the first cycles might explain the increased interface state density for ultra-thin Al$_2$O$_3$ films in Fig. 5.1(c) and (d), since deposition might start with the formation of nucleation islands, leaving parts of the silicon substrate unpassivated. The absence of unambiguous evidence for an initial island-growth regime for plasma-assisted ALD, in contrast to thermal ALD [55], explains the significantly more pronounced lifetime degradation for ultra-thin Al$_2$O$_3$ layers deposited by thermal ALD, compared to plasma-assisted ALD, observed in Fig. 5.1(a). Furthermore, structural defects and dangling bonds formed during the beginning of the ALD process might be healed at a later stage, e.g. by hydrogen passivation during the thermal post-deposition anneal, if a sufficiently large "bulk" of Al$_2$O$_3$ is present in thicker layers.

4.2.2 Dielectric permittivity

The presence of an interfacial SiO$_x$ adds an additional capacitance in series to the Al$_2$O$_3$ capacitance. Accordingly, the dielectric constant ε_r extracted from a *C-V* measurement is expected to deviate from the value of Al$_2$O$_3$. The dielectric properties of a stack are conveniently analyzed regarding the effective oxide thickness t_ox, which is calculated from the measured oxide capacitance C_ox assuming a single layer of SiO$_2$ with a relative permittivity of $\varepsilon_\mathrm{ox} = 3.9$, that is

$$t_\mathrm{ox} \equiv \frac{3.9\,\varepsilon_0}{C_\mathrm{ox}}. \tag{4.5}$$

If we divide a dielectric stack into infinitesimal slices with thickness $\mathrm{d}d$ and (depth-dependent) relative permittivity $\varepsilon_\mathrm{r}(d)$, the total oxide capacitance C_ox is described by the following equation:

$$\frac{1}{C_\mathrm{ox}} = \int \frac{1}{\mathrm{d}C} = \int \frac{\mathrm{d}d}{\varepsilon_0 \varepsilon_r(d)} = \frac{t_\mathrm{ox}}{3.9\,\varepsilon_0} \quad \Rightarrow \quad t_\mathrm{ox} = \int \frac{3.9}{\varepsilon_\mathrm{r}(d)} \mathrm{d}d. \tag{4.6}$$

From Eq. 4.6 the depth-resolved relative permittivity $\varepsilon_\mathrm{r}(d)$ can be determined from the slope of the effective oxide thickness t_ox as a function of the thickness d_eff of the deposited dielectric stack. Figure 4.5(a) shows the effective oxide thickness t_ox calculated from a *C-V* measurement using Eq. 4.5 as a function of effective film thickness d_eff determined by spectral ellipsometry for Al$_2$O$_3$ layers deposited by plasma-assisted ALD and subsequently annealed at 425 °C for 15 min. The inset demonstrates the linear dependence of d_eff on the number of ALD cycles at a growth per cycle of 0.121 nm/cycle, representative for Al$_2$O$_3$ deposited by plasma-assisted ALD. The data follows a linear dependence, indicating that the dielectric properties of the deposited layer are homogeneous down to a thickness of the order of a few nanometers. A linear fit to the data yields a relative permittivity of $\varepsilon_\mathrm{r} = 8.1 \pm 0.2$ for annealed Al$_2$O$_3$ deposited by plasma-assisted ALD.

We also observe an offset of $t_0 = (1.3 \pm 0.2)$ nm in the linear fit. Such an offset is easy to misinterpret: commonly, such an offset is attributed
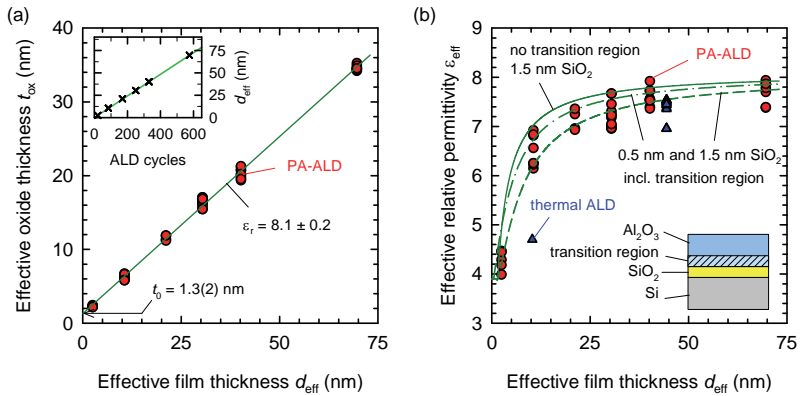
Figure 4.5: (a) Effective oxide thickness t_{ox} calculated from *C-V* measurements as a function of effective film thickness d_{eff} determined by spectral ellipsometry. The inset shows the linear dependence of d_{eff} on the number of ALD cycles. (b) Dielectric effective relative permittivity ε_{eff} as a function of effective film thickness d_{eff} for Al₂O₃ deposited by plasma-assisted ALD (red circles) and thermal ALD (blue triangles). Lines are calculations based on different models of the interface between Si and Al₂O₃, as explained by the sketch in the graph.

to an interfacial layer [59], if d_{eff} is interpreted as actual thickness of the Al$_2$O$_3$ layer. In our case, however, d_{eff} determined from ellipsometry is an *effective* optical thickness of the entire dielectric stack, and hence $t_{\text{ox}}(d_{\text{eff}} = 0) = 0$ is required. On one hand, quantum mechanical corrections due to accumulation of charge carriers in the accumulation layer lead to a decrease in t_{ox} by approximately $0.5 - 1\,\text{nm}$ [59], which already explains part of the offset. On the other hand, a deviation from the linear dependence is expected for small thickness values, if a thin interfacial layer with a relative permittivity below that of Al$_2$O$_3$ is present.

Figure 4.5(b) shows the effective relative permittivity $\varepsilon_{\text{eff}} = C_{\text{ox}} d_{\text{eff}}/\varepsilon_0$ as a function of the effective thickness d_{eff} for the same samples as shown in Fig. 4.5(a). Results for several samples deposited by thermal ALD are shown as well as blue triangles. Here, the presence of an interfacial layer at the c-Si/Al$_2$O$_3$ interface is apparent due to the significantly reduced relative permittivity for thin films below $20 - 30\,\text{nm}$ thickness, taking into account that the relative permittivity of bulk-like Al$_2$O$_3$ was shown to be 8.1 ± 0.2 in Fig. 4.5(a). In addition, the minimum measured value of $\varepsilon_{\text{eff}} = 4.0$ indicates that the dielectric closest to the Si surface needs to have $\varepsilon_{\text{r}} \leq 4.0$. Hence, we have assumed SiO$_2$ with $\varepsilon_{\text{r}} = 3.9$. The green lines in Fig. 4.5(b) show calculated values of ε_{eff} assuming different interface models as shown in the graph: *(i)* a single interfacial layer of $1.5\,\text{nm}$ SiO$_2$ (solid line), and *(ii)* $0.5\,\text{nm}$ (dash-dotted line) and $1.5\,\text{nm}$ (dashed line) of SiO$_2$, in conjunction with a transition region between SiO$_x$

relative permittivity $\varepsilon_{\text{r}}(x)$ in the transition region, we calculate a weighted average of the relative permittivities of SiO$_2$ and Al$_2$O$_3$ according to

$$\varepsilon_{\text{r}}(x) = 8.1\,\xi + 3.9\,(1 - \xi), \quad \text{where} \quad \xi = \frac{\text{Al:O}(x)}{2:3}. \qquad (4.7)$$

The parameter ξ, which reflects the proportion of Al$_2$O$_3$ in the transition region, is calculated from the depth resolved aluminum-to-oxygen ratio determined by XPS, assuming a growth per cycle of $0.121\,\text{nm/cycle}$, and is given by the dashed green line in Fig. 4.4(b), divided by $2/3$ for stochiometric Al$_2$O$_3$. The assumption of an extended transition region

at the interface is still consistent with the conclusion of a fairly homogeneous layer, as demanded by the linear dependence of the data shown in Fig. 4.5(a), as a deviation from the linear fit would only be evident for a film thickness below 5 nm in the case of the three different interface models assumed here. After all, the exponential decay constant of $\xi(x)$ has a value of only 2.4 nm.

Due to the scatter in the experimental data in Fig. 4.5(b), all three models are consistent with at least part of the data. The best agreement, however, is achieved by assuming a transition region in conjunction with a thin $(0.5 - 1.5\,\mathrm{nm})$ SiO_x at the interface between the c-Si and the transition region. This is in excellent agreement with the chemical analysis presented in the previous section.

For thin Al_2O_3 layers deposited by thermal ALD, a significantly lower relative permittivity is observed compared to plasma-assisted ALD, as shown in Fig. 4.5(b). For a film thickness of 10 nm we measure $\varepsilon_r = 4.7 \pm 0.3$, rather than $\varepsilon_r = 6.5 \pm 0.5$ for plasma-assisted ALD. For a film thickness of approximately 40 nm this difference is less pronounced, with values of $\varepsilon_r = 7.4 \pm 0.3$ for thermal ALD compared to $\varepsilon_r = 7.6 \pm 0.3$ for plasma-assisted ALD. This suggests a more severely perturbed growth of the first couple of AlO_x layers for the H_2O-based thermal ALD process compared to the O-based plasma-assisted ALD process, which is consistent with the comparably low passivation quality of Al_2O_3 layers deposited by thermal ALD with a thickness below 10 nm, as discussed in Sec. 5.1. Note that a severe growth inhibition has indeed been observed for the thermal ALD of Al_2O_3 on c-Si [21, 55].

4.3 Origin of the negative fixed charges

It is well known that the excellent surface passivation quality of Al_2O_3 is mainly due to a high negative fixed charge density in the Al_2O_3 films (compare Fig. 5.1), which leads to a depletion of electrons from the surface,

and hence a reduction of the surface recombination rate.

The negative fixed charges have previously been attributed to the presence of octahedrally coordinated Al in Al^{3+} and tetrahedrally coordinated Al in AlO_4^- [60], where the latter was proposed to be dominantly found at the interface due to the tetrahedrally coordinated Si in the interfacial SiO_x [61]. In contrast to this, we do not observe any XPS double-peak structures for the aluminum and oxygen peaks in Fig. 4.3(b), besides the contribution from the interfacial SiO_x, and hence both species are assumed to be present in only one charge state. The energy resolution of the XPS measurements in this study might however be insufficient to actually resolve the different contributions to the Al-2p peak.

An alternative candidate for the origin of the high negative charge density at the interface, based on the XPS results presented above, could be the high oxygen-to-aluminum ratio caused by the incomplete ALD process during the first cycles. Density functional calculations show that oxygen dangling bonds in Al_2O_3 form charge-state transitions levels well below the silicon valence band edge, hence being negatively charged, while aluminum dangling bonds form levels above the silicon conduction band edge, hence being positively charged [62]. Oxygen dangling bonds are expected to dominate in oxygen rich material, while aluminum dangling bonds dominate in Al rich material. In addition, interstitial oxygen point defects O_i and aluminum vacancies V_{Al} were shown to be preferentially negatively charged [63, 64]. Hence, based on these calculations, the excess oxygen observed in Fig. 4.4(b) near the $c\text{-}Si/Al_2O_3$ interface might result in a negative fixed charge density near or at the interface.

Several authors reported [65, 66] that the fixed charge density at the $c\text{-}Si/Al_2O_3$ interface increases under illumination, which is explained by tunneling of excited electrons through the interfacial SiO_x into the Al_2O_3 conduction band. The transient behavior of the charge density was best described by assuming two or three different types of charge traps, and the de-trapping process was generally found to be slower than the trapping process. Hole injection into the Al_2O_3 is considered to be negligible due

to the larger barrier height for holes ($\approx 3.3 - 4.2\,\text{eV}$) than for electrons ($\approx 2.0 - 2.2\,\text{eV}$) [65, 67, 68]. Note that there exists significant uncertainty in the bandgap of amorphous ALD-Al$_2$O$_3$, with values between 6.4 and 7.3 eV reported in the literature [17, 68, 69], and hence in the hole energy barrier.

The models described above attribute the charges at the c-Si/Al$_2$O$_3$ interface to charged traps within the Al$_2$O$_3$ near the interface. Hence, the negative charge density for Al$_2$O$_3$ is in fact not an actual *fixed* charge density, but at least partially a *trapped* charge density (for a differentiation of these terms see for example Ref. 33). Nevertheless, the term "fixed charge density" and the symbol Q_f will be used in this thesis to denote the charge density within the Al$_2$O$_3$ near the c-Si/Al$_2$O$_3$ interface, irrespective of the actual nature of these charges.

4.3.1 Defect and charge formation under applied bias

Figure 4.6 shows the fixed charge density Q_f and the midgap interface state density $D_\text{it.midgap}$ determined by C-V analysis for 10 nm of Al$_2$O$_3$ deposited by plasma-assisted ALD on 1.5 Ωcm p-Si for repeated measurements on the same sample. The first measurement yields a fairly low fixed charge density of $Q_\text{f} \approx -2 \times 10^{12}\,\text{cm}^{-2}$ and a moderate interface state density at midgap of approximately $3 \times 10^{11}\,\text{eV}^{-1}\text{cm}^{-2}$. The low value of the fixed charge density is in good agreement with the value of $Q_\text{f} = -2 \times 10^{12}\,\text{cm}^{-2}$ reported by Schiele *et al.* [70], which they attribute to substantial damage to the c-Si/Al$_2$O$_3$ interface during electron beam evaporation of Al. With subsequent measurements in Fig. 4.6, the fixed charge density and interface state density increase to values of $Q_\text{f} = -(4 - 5) \times 10^{12}\,\text{cm}^{-2}$ and $D_\text{it.midgap} = (1 - 2) \times 10^{12}\,\text{eV}^{-1}\text{cm}^{-2}$, respectively. After annealing the sample at 300 °C for 30 min, the damage to the interface is fully recovered. Moreover, the fixed charge density remains at a high level of $Q_\text{f} = -(4 - 7) \times 10^{12}\,\text{cm}^{-2}$, and the interface state density is stable under subsequent measurements. If the sample
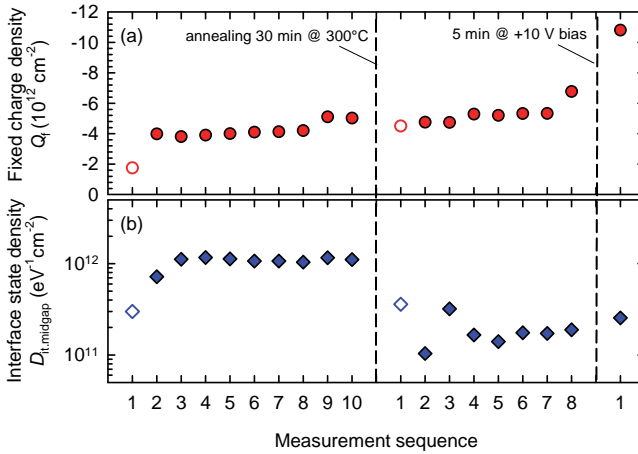
Figure 4.6: (a) Fixed charge density Q_f and (b) midgap interface state density $D_{\text{it.midgap}}$ determined from C-V measurements for 10 nm of Al_2O_3 deposited by plasma-assisted ALD on 1.5 Ωcm p-Si for repeated measurements on the same sample. Open symbols denote "virgin" measurement, where the voltage sweep starts at 0 V. The final voltage of one sweep is 2.5 V.

is kept in deep inversion for a prolonged time (5 min at a gate voltage of $+10\,$V in Fig. 4.6), a significant increase in the negative fixed charge density to values above $10^{13}\,\mathrm{cm}^{-2}$ is observed.

The change in Q_f when applying a bias voltage is investigated in more detail in a hysteresis experiment for $10\,$nm of $\mathrm{Al_2O_3}$ deposited on $1.5\,\Omega\mathrm{cm}$ *p*-Si, as shown in Fig. 4.7: after recording the initial *C-V* curve (black dot), the sample is biased for 1 min at a voltage $V_\mathrm{max} > 0$ and a *C-V* curve is measured, then the sample is biased for 1 min at a voltage $V_\mathrm{max} < 0$ and again a *C-V* curve is measured. After the first experiment, the sample is stored for two days in the dark and then gradually annealed at $350\,^\circ$C for a total of 15 min (green squares in Fig. 4.7). All *C-V* curves are measured from inversion to accumulation (red triangles up in Fig. 4.7) after applying a positive bias, and from accumulation to inversion for all other measurements.

After applying a *positive* bias voltage of several volt, the flatband voltage V_F and fixed charge density Q_f shown in Fig. 4.7 increase significantly. However, upon applying a *negative* bias, V_F and Q_f are again reduced, albeit to values higher than the initial values $V_{\mathrm{F}.0}$ and $Q_{\mathrm{f}.0}$. Although this reduction can be quite severe, for example $\Delta V_\mathrm{F} = -0.6\,$V for $V_\mathrm{max} = -6\,$V, virtually no further change in V_F is observed for additional cycles of exposing the sample to a negative bias, as shown by the measurements $11 - 14$ in Fig. 4.7. Additionally, no significant change is observed after storing the sample for two days in the dark (measurement 15 in Fig. 4.7). However, annealing the sample for 5 min at $350\,^\circ$C reduces the charge density to $Q_\mathrm{f} = -4.8 \times 10^{12}\,\mathrm{cm}^{-2}$.

A similar change of the fixed charge density Q_f with experimental condition is observed for corona measurements. Figure 4.8 shows the maximum effective SRV S_max as a function of deposited corona charge density Q_c for three consecutive corona measurements, where the deposited corona charges have been removed by rinsing the sample in de-ionized water after each measurement. The change of the peak of $S_\mathrm{max}(Q_\mathrm{c})$ clearly corroborates the formation of interface defects and fixed charges, as S_0
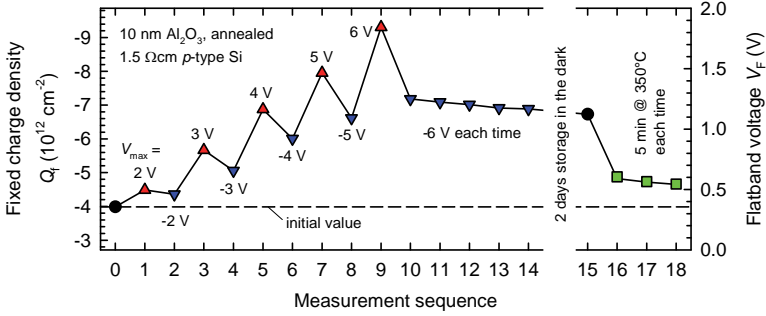
Figure 4.7: Fixed charge density Q_f (left axis) and flatband voltage V_F (right axis) after biasing the sample for 1 min at the voltages indicated in the graph. The sample is stored 2 days in the dark and then annealed at $350\,°C$ for a total of 15 min (green squares).
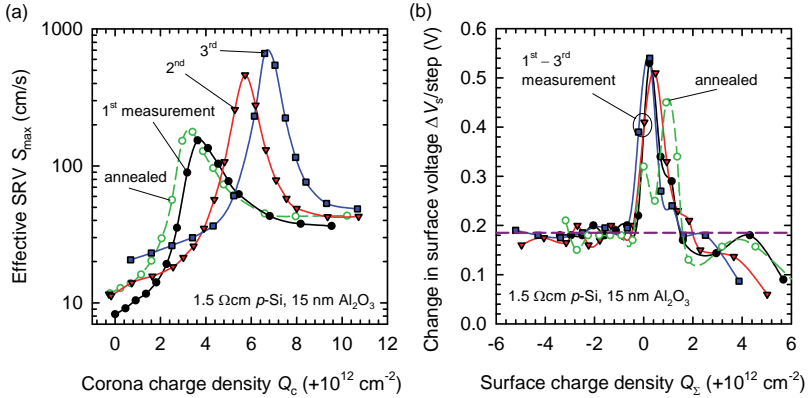
Figure 4.8: (a) Maximum effective SRV S_{max} as a function of deposited corona charge density Q_c for three consecutive corona measurements (solid symbols), and after subsequently annealing the sample for 15 min at $350\,°C$ (open symbols). The deposited corona charges have been removed by rinsing the sample in deionized water after each measurement. (b) Change ΔV_s in surface voltage for each corona charging step in graph (a) as a function of surface charge density $Q_\Sigma = Q_c + Q_f$. The expected nominal value of $185\,mV$ is given by the violet dashed line.

79

increases from $150\,\mathrm{cm/s}$ to $460\,\mathrm{cm/s}$ and $700\,\mathrm{cm/s}$ in consecutive measurements, and $-Q_\mathrm{f}$ increases from $3.9\times10^{12}\,\mathrm{cm}^{-2}$ to $5.7\times10^{12}\,\mathrm{cm}^{-2}$ and $6.8\times10^{12}\,\mathrm{cm}^{-2}$. Figure 4.8(b) shows the change ΔV_s in surface voltage for each corona charging step in Fig. 4.8(a) as a function of surface charge density $Q_\Sigma = Q_\mathrm{c} + Q_\mathrm{f}$. Here, a constant charging rate $\Delta Q_\mathrm{c} = 4.54(3)\times10^{11}\,\mathrm{cm}^{-2}/\mathrm{step}$ is assumed, which was determined on a reference sample coated with a thick thermally-grown SiO$_2$. The corresponding expected nominal value of $\Delta V_\mathrm{s} = 185\,\mathrm{mV/step}$ is indicated by the violet dashed line in Fig. 4.8(b). Initially ($Q_\Sigma < -1\times10^{12}\,\mathrm{cm}^{-2}$) the Fermi level is in or near the valence band, and the slope $\mathrm{d}V_\mathrm{s}/\mathrm{d}Q_\mathrm{c}$ is constant according to Eq. 3.46 and agrees well with the expected value. As the Fermi level is swept across the silicon bandgap ($-1\times10^{12}\,\mathrm{cm}^{-2} < Q_\Sigma < +2\times10^{12}\,\mathrm{cm}^{-2}$), the surface voltage changes rapidly due to the strong dependence of the surface potential ψ_s on the deposited corona charge density.

For $Q_\Sigma > +2\times10^{12}\,\mathrm{cm}^{-2}$ the Fermi level is in or near the conduction band, and again a constant $\mathrm{d}V_\mathrm{s}/\mathrm{d}Q_\mathrm{c}$ is expected. However, in this region the surface voltage is found to increase slower than expected for all measurements. On the one hand, the formation of additional negative fixed charges in the Al$_2$O$_3$ might balance some of the deposited positive corona charges, which would lead to a slower rise in Q_Σ. On the other hand, some of the deposited corona charges might be discharged by leakage currents. For this to occur, however, electrons need to be injected into the Al$_2$O$_3$ layer, which is considered to be the essential mechanism of the formation of fixed charges in Al$_2$O$_3$ [65, 66]. Accordingly, the data presented in Fig. 4.8 is consistent with the formation of additional fixed charges in the Al$_2$O$_3$ layer or at the c-Si/Al$_2$O$_3$ interface under conditions that lead to a high electron density at the silicon surface.

After annealing the sample for 15 min at 350 °C, the interfacial damage is almost fully recovered, in good agreement with *C-V* data in Fig. 4.6(b), and Q_f is reduced to $-(3-4)\times10^{12}\,\mathrm{cm}^{-3}$.

In the *C-V* and corona experiments, a significant formation of negative

charges was only observed for surface energies near or within the silicon conduction band. Furthermore, Gielis *et al.* observed charge injection into the Al_2O_3 conduction band, rather than a tunneling process directly into the trap levels within the Al_2O_3 [65]. Both findings are unexpected if the traps responsible for the charge formation are located very close to the c-Si/Al_2O_3 interface and have an energy below the silicon valence band edge. However, it might be possible that in fact positively charged defects in the Al_2O_3 layer are responsible for the formation of an additional net negative charge density upon illumination or charge injection. For example, the $(+/0)$ and $(0/-)$ transitions of the aluminum dangling bond DB_{Al} are predicted to lie energetically in the vicinity of the silicon conduction band edge [62]. In this model, oxygen-related point defects with energies below the silicon valence band edge, which are located at or near the c-Si/Al_2O_3 interface, give rise to a negative fixed charge density of approximately $Q_f = -4 \times 10^{12}\,\mathrm{cm}^{-2}$, which is stable under typical experimental conditions including annealing. In Fig. 5.1(b) the fixed charge density Q_f was found to be virtually independent of the thickness of the Al_2O_3 layer. Hence, negative and positive charges in the Al_2O_3 bulk are considered to roughly balance. Note, however, that a non-vanishing positive or negative bulk charge density in Al_2O_3 was observed at least for specific sample preparations by several authors [62, 71]. Upon charge injection or illumination, positively charged bulk traps might be neutralized or charged negatively by electron capture, resulting in an increased net negative charge density. As shown in Fig. 4.7 and 4.8, these charge states are however unstable under annealing and, at least partly, unstable if a bias voltage of reverse polarity is applied. At the moment, this model is however speculative, and further work is needed to unambiguously determine the origin of the negative fixed charge density in Al_2O_3.
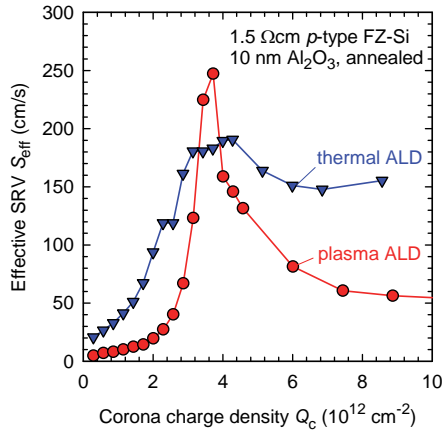
Figure 4.9: Effective surface recombination velocity S_{eff} at $\Delta n = 10^{15}\,\text{cm}^{-3}$ as function of deposited corona charge density Q_c for Al$_2$O$_3$ films deposited by plasma-assisted (red circles) and thermal (blue triangles), respectively.

4.3.2 Spatial homogeneity of the negative fixed charge density

Corona measurements indicate similar fixed charge densities for plasma-assisted and thermal ALD, and S_0 values are found to be lower in Al$_2$O$_3$ films deposited by thermal ALD. However, plasma-assisted ALD is usually superior in obtaining low interface state densities and highest effective lifetimes, as shown for example in Fig. 5.1(a) and (d). At first sight this behavior is unexpected, as S_0 is proportional to D_{it}, and for a given fixed charge density Q_f the surface recombination velocity S_{eff} is expected to scale with S_0. A plot of the surface recombination velocity S_{eff} at $\Delta n = 10^{15}\,\text{cm}^{-3}$ as a function of deposited Corona charge density Q_c is shown in Fig. 4.9 for annealed 10 nm Al$_2$O$_3$ layers deposited on 1.5 Ωcm p-type FZ-Si by plasma-assisted and thermal ALD, respectively. Two major differences between samples passivated by thermal and plasma-assisted ALD are apparent:

1. The peak of the effective surface recombination velocity S_{eff} around $Q_c = -Q_f$ is broader for samples passivated by thermal ALD than in the case of plasma-assisted ALD. We explain the broader shape of the peak by a spatially inhomogeneous charge distribution (on a microscopic scale) in the thermal ALD samples, whereas the fixed charges in the Al_2O_3 films deposited by plasma-assisted ALD are considered to be spatially more homogeneous, resulting in a sharper $S_{\text{eff}}(Q_c)$ peak. For the $2.5 \times 2.5\,\text{cm}^2$ samples used for this experiment the deposited corona charge density is largely uniform and drops by less than $5\,\%$ towards the wafer edges. Any significant inhomogeneity in the total charge density must therefore be attributed to an inhomogeneous fixed charge density Q_f. As a consequence, the level of chemical passivation achieved by thermal ALD cannot be directly accessed by corona charge measurements, since a locally non-zero charge density remains even for a deposited corona charge density equal to the mean absolute fixed charge density $\left|\langle Q_f \rangle\right|$. For Al_2O_3 films deposited by plasma-assisted ALD, the spatial inhomogeneity of the fixed charge is covered in more detail in Sec. 3.3.2, where the standard deviation of the fixed charge distribution – assuming a Gaussian distribution – was shown to be $< 2 \times 10^{11}\,\text{cm}^{-2}$.

2. In the regimes where the total charge density $Q_f + Q_c$ is sufficiently large to provide an effective field-effect passivation, the measured effective surface recombination velocity S_{eff} is larger for thermal ALD than is the case for plasma-assisted ALD, indicating a reduced level of chemical passivation. This is corroborated by measurements of the interface state density presented in the following chapter. The unexpectedly high value of S_{eff} for high positive charge densities $Q_c > -Q_f$ is discussed in Sec. 5.3.2.

5 Recombination at the c-Si/Al$_2$O$_3$ interface

Electrical measurements on metal-insulator-silicon (*MIS*) capacitors provide a convenient tool to study the electronic interface properties at the silicon/insulator interface. Numerical analysis using an equivalent electrical circuit model enables us to extract the energy-resolved fundamental interface recombination parameters, i.e. interface state density D_{it}, capture time constants τ_n and τ_p for electrons and holes, as well as the corresponding electron and hole capture cross sections σ_n and σ_p. In this chapter, the measurement techniques introduced in Chapter 3 are applied to Al$_2$O$_3$ layers. In order to verify the interface recombination parameters extracted from MIS measurements, numerical simulations of the injection-level-dependent surface recombination velocity for Al$_2$O$_3$-passivated silicon samples are compared with experimental data measured at different surface charge densities.

5.1 Role of chemical and field-effect passivation

There are two complementary contributions to a reduction in the surface recombination velocity: *(i)* a reduction in the density of recombination-active interface traps (*chemical passivation*), characterized by the interface state density D_{it}, and *(ii)* a reduction in the electron or hole concentration near the surface (*field-effect passivation*), characterized for example by the fixed charge density Q_{f}, which causes a band bending in the c-Si towards the interface.

The effective carrier lifetime τ_{eff} of Al$_2$O$_3$-passivated Si wafers is typically

found to deteriorate if the thickness of the Al$_2$O$_3$ passivation layer is reduced below a critical thickness. Figure 5.1(a) shows effective lifetime values τ_{eff} measured using the photoconductance decay technique (*PCD*, Sinton Instruments WCT 120 lifetime tester) at an injection density of $\Delta n = 10^{15}\,\text{cm}^{-3}$ on 1.5 Ωcm *p*-type FZ-Si wafers as a function of the Al$_2$O$_3$ thickness *d*. The wafers were passivated with Al$_2$O$_3$ films deposited by plasma-assisted, thermal, and spatial ALD, respectively. A deterioration of the otherwise excellent surface passivation quality is observed below a critical thickness $d < 5\,\text{nm}$ for plasma-assisted ALD and $d < 10\,\text{nm}$ for both thermal and spatial ALD.

Such thin layers of only a few nanometers are challenging to investigate by the capacitance - voltage method described in section 3.2.2 because:

- Leakage currents through the thin Al$_2$O$_3$ layer may be too large for a reliable quasi-static measurement.

- The interface properties might be severely influenced by the electronic properties of the metal contact.

- The interface might be damaged by electron bremsstrahlung emitted during the electron gun evaporation of the metal contacts.

Corona charge analysis (see Sec. 3.4), on the other hand, is a contactless technique and poses less strict constrains on the permitted leakage current as the remaining charge density can be determined with a Kelvin probe. Figures 5.1 (b)-(d) show the fixed charge density Q_{f}, the SRV parameter S_0, and the interface state density D_{it} at midgap for a wide range of Al$_2$O$_3$ film thickness values, where the Al$_2$O$_3$ layers were deposited by plasma-assisted (red circles), thermal (blue triangles), and spatial ALD (green squares), respectively. All samples were annealed at the optimum annealing conditions. The ultralow surface recombination velocities routinely obtained on *p*- and *n*-type silicon are predominantly attributed to a pronounced field effect passivation caused by a high negative fixed charge density of $Q_{\text{f}} = -(4 \pm 1) \times 10^{12}\,\text{cm}^{-2}$ in the Al$_2$O$_3$, which is consistent with results published earlier by other authors [4, and references
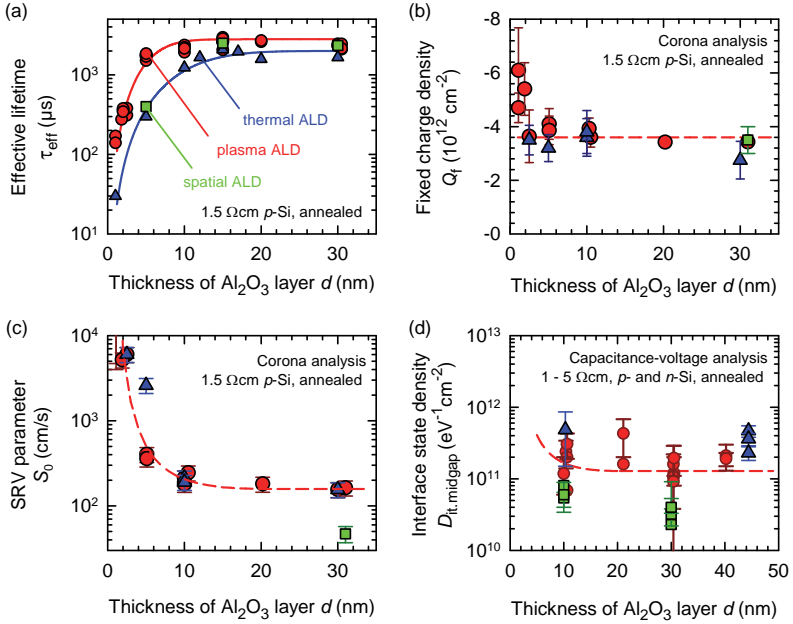
Figure 5.1: (a) Effective lifetime τ_{eff} measured at an injection density of $\Delta n = 10^{15}\ \text{cm}^{-3}$, (b) fixed charge density Q_f and (c) SRV parameter S_0 determined by corona analysis, and (d) midgap interface state density $D_{\text{it.midgap}}$ determined by C-V analysis as a function of Al_2O_3 film thickness d for layers deposited by plasma-assisted (red circles), thermal (blue triangles), and spatial ALD (green squares), respectively. Lines are guides to the eye.

therein]. The apparent rise in Q_f for very thin Al$_2$O$_3$ films might be due to calibration errors for ultra-thin Al$_2$O$_3$ films during the corona charge experiment. Due to leakage currents reducing the total amount of corona charge remaining on the sample surface, the fixed charge density Q_f in the ultra-thin films is expected to be closer to the lower bound of the uncertainty range. Taking this into account we find the same high negative fixed charge density of $Q_f = -(4\pm1)\times10^{12}\,\mathrm{cm}^{-2}$ for all samples from 1 nm to 32 nm thickness, which indicates that the negative charges are located within 1 nm of the interface. This is an important result, as, consequently, even ultra-thin Al$_2$O$_3$ films of 1 nm thickness profit from the high level of field-effect passivation, enabling surface recombination velocities $S_{\mathrm{eff}} < 100\,\mathrm{cm/s}$ at $\Delta n = 10^{15}\,\mathrm{cm}^{-3}$ on these samples, in good agreement with results published earlier [9, 72]. Measurements of the dark sheet resistance of the Al$_2$O$_3$-induced inversion layer on n-type Si, shown in Fig. 7.4 and discussed in Sec. 7.2, indicate that a significant charge density is already present in AlO$_x$ films with a thickness well *below* 1 nm.

The limiting factor for the application of ultra-thin passivation layers of Al$_2$O$_3$ is their reduced level of chemical passivation. The interface state density at the c-Si/Al$_2$O$_3$ interface remains in the range of $D_{\mathrm{it}} = (1-3)\times10^{11}\,\mathrm{eV}^{-1}\mathrm{cm}^{-2}$ for Al$_2$O$_3$ films down to $5-10$ nm, which significantly increases for thinner layers and explains very well the deterioration of the effective lifetime τ_{eff} with decreasing film thickness observed in Fig. 5.1(a). Below a film thickness of 3 nm, no significant level of chemical passivation was observed, and lifetimes below 5 μs, corresponding to $S_0 > 10^4\,\mathrm{cm/s}$, were measured at $\Delta n = 10^{15}\,\mathrm{cm}^{-3}$ for zero net charge $Q_f + Q_C = 0$.

Remarkably, we measure the same negative fixed charge density of $Q_f = -(4 \pm 1)\times10^{12}\,\mathrm{cm}^{-2}$ independent of the deposition method (plasma-assisted, thermal, or spatial ALD). However, the interface state density, and hence the level of chemical passivation, varies between different ALD methods. Furthermore, for Al$_2$O$_3$ layers below 10 nm thickness deposited by thermal or spatial ALD, the increase in D_{it} with decreasing layer

thickness is more pronounced than in the case of plasma-assisted ALD. This is consistent with a more severe growth inhibition for thermal ALD compared to plasma-assisted ALD, as discussed in Sec. 4.2.2.

5.2 Interface recombination parameters

The interface state density D_{it}, the capture time constants τ_n for electrons and τ_p for holes, as well as the corresponding capture cross sections σ_n and σ_p at the Al_2O_3/c-Si interface are determined as functions of the energetic position in the silicon bandgap by capacitance-voltage and conductance measurements on MIS capacitors. Unless stated otherwise, the following standard process sequence is used for the fabrication of the MIS capacitor samples: We use $280 - 300\,\mu\mathrm{m}$ thick $1.3 - 1.5\,\Omega\mathrm{cm}$ p-type or $1.5 - 1.6\,\Omega\mathrm{cm}$ n-type FZ-Si wafers, respectively, with a size of $2.5 \times 2.5\,\mathrm{cm}^2$. The samples were RCA-cleaned and subsequently coated with an Al_2O_3 film on the front side, deposited by plasma-assisted ALD in an Oxford Instruments FlexAL reactor. All samples were annealed for 15 min at $425\,^{\circ}\mathrm{C}$, then circular aluminum gate contacts were defined on top of the Al_2O_3 film by electron gun evaporation through a shadow mask, and a full-area aluminum back contact was evaporated on the rear side. No post-metalization anneal was performed before the first measurement. Figure 3.3(a) shows a sketch of the sample structure.

5.2.1 Interface state density

The interface state density D_{it} obtained by the conductance method using Eq. 3.39 is shown in Fig. 5.2(a) and compared to D_{it} values obtained by capacitance-voltage analysis. Both methods are in excellent agreement and yield D_{it} values near midgap of $(6 - 20) \times 10^{10}\,\mathrm{eV}^{-1}\mathrm{cm}^{-2}$, which are virtually independent of energy over a wide range of energies around midgap. For numerical simulations the exponential tails towards
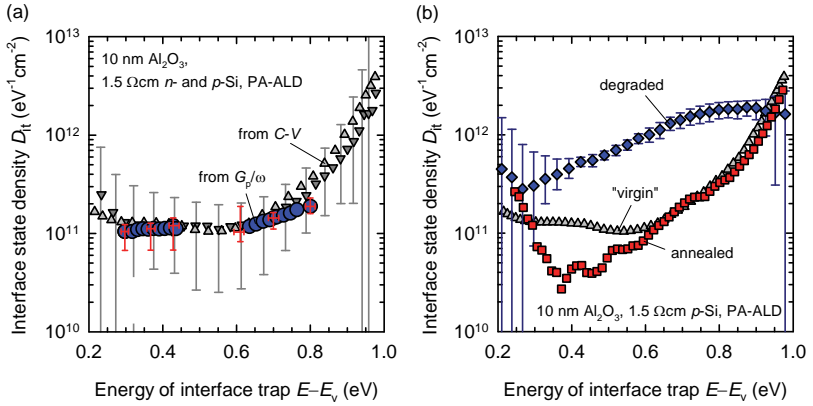
Figure 5.2: (a) Interface state density D_{it} as a function of the energetic position $E - E_v$ of the interface trap, obtained by the conductance method (blue circles, red error bars) and *C-V* analysis on *n*-type (triangles down) and *p*-type (triangles up) Si for 10 nm of Al₂O₃ deposited by plasma-assisted ALD. (b) Energy-dependent interface state density derived from *C-V* measurement for an initial measurement ("virgin", gray triangles), the first subsequent measurement ("degraded", blue diamonds), and after annealing the sample at 300 °C for 15 min (red squares), all on the same contact pad.

the band edges were neglected, as they are attributed to measurement artifacts in the *C-V* analysis (compare Sec. 3.2.2). The remaining defect distribution is well described by a virtually constant D_{it} with a small Gaussian-shaped peak around an energy of $0.8 - 0.9$ eV above the valence band edge, as discussed in Sec. 5.2.3. From the data shown in Fig. 5.2(a), the assumption of a defect peak in the upper half of the bandgap is difficult to justify due to the generally low values of D_{it}. According to Sec. 4.3.1, additional defect states at the interface are created upon applying an external bias voltage. Figure 5.2(b) shows the energy-dependent interface state density derived from *C-V* measurements for an initial "virgin" measurement, where the gate voltage is swept from 0 V towards accumulation or inversion on two different contact pads, and a subsequent measurement on one of the same contact pads. Here, the degraded curve [blue diamonds in Fig. 5.2(b)] clearly indicates a peak of the interface state density in the upper half of the bandgap. In addition, Fig. 5.2(b) shows a measurement after annealing the sample at 300 °C for 15 min (red squares), which corroborates that the additional interface states created by applying an external bias voltage can be fully eliminated by a short annealing.

Figure 5.3 shows the interface state density D_{it} as a function of the energetic position $E - E_v$ of the interface trap, obtained by *C-V* analysis, for Al_2O_3 deposited by thermal (blue triangles) and spatial ALD (green squares), and compared to plasma-assisted ALD (red circles). Note that Si wafers with different dopant types and concentrations were used, the resulting interface state distributions are, however, representative of the respective deposition techniques. For spatial ALD, an exceptionally low interface state density around midgap of $D_{it.midgap} = (7 \pm 1) \times 10^{10}$ eV^{-1}cm^{-2} is observed. Here, no distinct dependence of D_{it} on energy is apparent, and D_{it} is virtually constant over most of the accessible energy range in the bandgap. The interface state density for thermal ALD is the highest with values of $D_{it.midgap} = (3 \pm 1) \times 10^{11}$ eV^{-1}cm^{-2}, and the data in Fig. 5.3 suggest a peak slightly below midgap for thermal ALD. Black and McIntosh have identified two distinct peaks in D_{it}– one
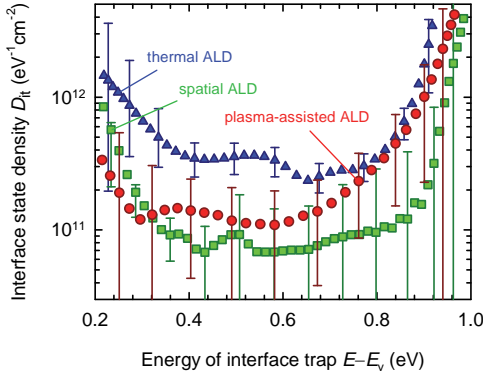
Figure 5.3: Interface state density D_{it} as a function of the energetic position $E - E_{\mathrm{v}}$ of the interface trap, obtained by *C-V* analysis, for Al₂O₃ deposited by plasma-assisted (red circles), thermal (blue trianlges), and spatial ALD (green squares), respectively.

slightly below midgap and one in the upper half of the bandgap – for Al₂O₃ deposited by atmospheric pressure CVD [73]. Hence, the most reasonable interpretation of Fig. 5.3 seems to be that in fact two distinct defect peaks are present at the c-Si/Al₂O₃ interface, whose relative contributions are different for different deposition techniques. A model of the defects at the c-Si/Al₂O₃ interface is discussed in more detail in Sec. 5.2.3.

5.2.2 Capture cross sections and time constants

Figure 5.4 shows the capture time constants τ_p (below midgap) and τ_n (above midgap) calculated from the peak frequency ω_{peak} of a conductance measurement using Eq. 3.40, and the corresponding capture cross sections σ_p and σ_n. The solid green lines in Fig. 5.4(a) are fits to the experimental data, which intersect at an energy E_0 of 40 meV below the intrinsic Fermi energy E_{i}. This energy corresponds to the symmetry point
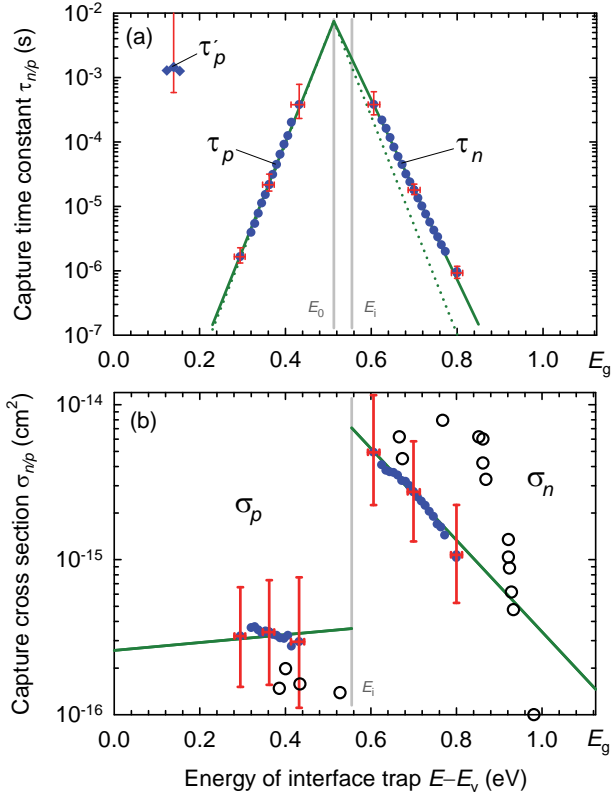
Figure 5.4: (a) Capture time constants τ_p (below midgap) and τ_n (above midgap) as a function of the energetic position in the silicon bandgap for the main defect (circles) and a second type of defect (diamonds). The solid green lines are fits to the experimental data; the dotted green lines illustrate the relation $\tau \propto \exp(\pm\beta E)$ expected from Eq. 3.41 and 3.42 for constant capture cross sections. (b) Capture cross sections σ_n and σ_p of the main defect (solid symbols) and literature data for the c-Si/SiO$_2$ interface (open symbols, Ref. 74). The solid green lines were calculated using the fit results from part (a). Error bars are shown in red for exemplary data points.

of the intrinsic defects at the Si/SiO$_2$ interface, reported earlier by Füssel et al. [75] to lie 40 meV below midgap, which acts as charge neutrality level in silicon. We obtain capture cross sections of $\sigma_n = (7 \pm 4) \times 10^{-15}$ cm^2 and $\sigma_p = (4 \pm 3) \times 10^{-16}$ cm^2 at midgap. The asymmetry $\sigma_n/\sigma_p = 5 - 70$ mainly originates from the difference of 40 meV between E_0 and E_i, which results in a factor of 20 in the midgap ratio of σ_n/σ_p. The dotted green lines in Fig. 5.4(a) illustrate the relation expected from Eq. 3.41 and 3.42 for energy-independent capture cross sections, which is well fulfilled for σ_p in the lower half of the bandgap. Hence, the hole capture cross section σ_p below midgap is virtually independent of energy, while the electron capture cross section σ_n above midgap decreases towards the conduction band edge E_c, as illustrated in Fig. 5.4(b). It should be kept in mind, however, that small variations in the capture time constant lead to a large error in the capture cross section, which could conceal a more pronounced energy dependence of σ_p.

Figure 5.4(b) only shows capture cross sections over a relatively small energy range. As explained in Sec. 3.3.3, we have discarded all data where the experimental and numerically computed peak shapes deviate significantly, in order to take into account the limited measurement range and inaccuracies of the series resistance correction.

Over a wide range of energies around midgap, the capture cross sections σ_n and σ_p shown by the solid symbols in Fig. 5.4(b) are similar to capture cross sections measured for c-Si passivated with high-quality thermal silicon dioxide (SiO$_2$, open symbols in Fig. 5.4(b), Ref. 74) or AlO$_x$ deposited by PECVD [76]. This similarity between Al$_2$O$_3$ and SiO$_2$ is attributed to the thin silicon oxide layer forming at the c-Si/Al$_2$O$_3$ interface (compare Sec. 4.2), which presumably dictates the chemical conditions, and hence the recombination parameters, at the interface.

For several p-type Si samples a second peak in the G_p/ω vs. ω curve was identified at low frequencies, as shown in Fig. 3.6(b), and as shown by the blue diamonds in Fig. 5.4(a). This peak is attributed to a second type of defect with a unique set of recombination parameters $D_{it}^{\cdot}$, $\tau_p^{\cdot}$ and

σ_p', which can only be resolved far from midgap where $\tau_p'(E)$ drops below the detection limit of $5\,\mathrm{ms}$. The corresponding capture cross sections σ_p' can be estimated to be below $10^{-19}\,\mathrm{cm^2}$ near the valence band edge, and are, hence, at least three orders of magnitude smaller than σ_p of the main defect, presumably making this second defect less important concerning interface recombination. However, the energy dependence of σ_p' remains unknown as the second defect could not be resolved at energies closer to midgap. Nevertheless, this second defect is ignored in the following.

5.2.3 Defect model

Black and McIntosh have recently measured the energy-dependent interface recombination parameters for Al_2O_3 layers deposited by atmospheric pressure chemical vapor deposition (*APCVD*), and have obtained a similar energy-dependence of the capture cross sections for the range of energies shown in Fig. 5.4(b) [73]. In their work they interpret the energy-dependent cross sections as a superposition of two distinct defects with constant capture cross sections, and show that this interpretation is consistent with experimental lifetime data.

In our conductance measurements, comparable to the data in Ref. 73, all peaks in the $G_\mathrm{p}(\omega)/\omega$ spectra are well described by a single defect, as exemplified in Fig. 3.6(a). Double peaks in the spectra are only observed for two clearly distinct defects for some of the p-type samples, as shown in Fig. 3.6(b). However, if two defects have fairly similar capture cross sections, the superposition of two distinct $G_\mathrm{p}(\omega)/\omega$ peaks yields a single – slightly broadened – peak corresponding to an effective capture cross section σ_eff in between the capture cross sections σ_1 and σ_2 of the two constituting peaks. Furthermore, if one defect clearly dominates due to a significantly higher interface state density at the respective energy, the other defect will not contribute significantly to the recorded $G_\mathrm{p}(\omega)/\omega$ spectrum.

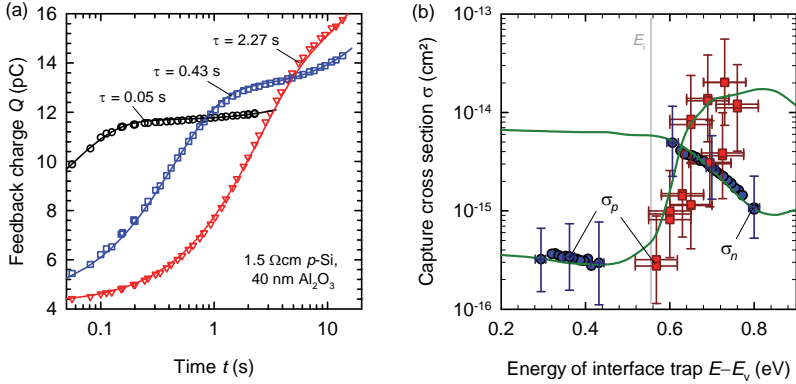The charging transient $Q(t)$ during a *C-V* measurement provides infor-

Figure 5.5: (a) Exemplary charging transients $Q(t)$ measured on $1.5\,\Omega$cm p-Si coated with 40 nm of annealed Al_2O_3. Solid lines are fits of Eq. 5.1 to the data. (b) Capture cross sections obtained from conductance measurements (blue circles) and charging transients (red squares). Solid lines are calculated apparent capture cross sections for a superposition of the three defects A, B, and C summarized in Tab. 5.1.

mation about the capture time constant τ_p of holes in the upper half of the silicon bandgap, where τ_p is large enough to be detected. The time dependence of the feedback charge and the three different charge measurements in a quasi-static C-V measurement are depicted in Fig. 3.4(a). The charging transient is described by an exponential function

$$Q(t) = J_{\mathrm{L}}t + Q_0 + Q_{\mathrm{it}}\left(1 - e^{-t/\tau}\right), \qquad (5.1)$$

where J_{L} is the equilibrium leakage current in the experimental setup, Q_0 is the number of charges which instantly follow the gate voltage change, and Q_{it} is the number of charges transferred between silicon and interface states with a capture time constant τ. Note that Q_{it} is not directly proportional to D_{it}, as the change in surface potential is smaller than the change in gate voltage due to the finite oxide capacitance C_{ox}. By varying the delay time t_{delay} at a constant bias voltage V_{G}, the

charging transient $Q(t)$ can be reconstructed from the measured quasi-static capacitance C_{QS} and leakage current Q/t. Figure 5.5(a) shows three exemplary plots of the measured $Q(t)$ transients, solid lines are fits of Eq. 5.1 to the data. Figure 5.5(b) shows the energy-dependent hole capture cross section $\sigma_p(E)$ calculated from the time constants τ obtained from fitting Eq. 5.1 to $Q(t)$ data, together with capture cross sections obtained from conductance measurements (compare Fig. 5.4). Despite the large uncertainty range, the data clearly supports an increasing capture cross section with increasing energy for holes in the upper half of the silicon bandgap, similar to the results of Black and McIntosh [73].

Parameter	Dimension	Defect A	Defect B	Defect C
$E_0 - E_v$	eV	$-$	0.85	0.50
w	eV^2	(bandgap)	$0.015^\dagger$	0.015
Best fit σ_n	cm^2	7×10^{-15}	3×10^{-16}	$\approx 5 \times 10^{-15}$
Range σ_n	cm^2	$(2-20) \times 10^{-15}$	$(1-20) \times 10^{-16}$	any
Best fit σ_p	cm^2	4×10^{-16}	2×10^{-14}	2×10^{-16}
Range σ_p	cm^2	$(1-16) \times 10^{-16}$	$(0.5-8) \times 10^{-14}$	$(0.4-6) \times 10^{-16}$
σ_n/σ_p	$-$	≈ 20	≈ 0.02	≈ 25

Table 5.1: Recombination parameters of the defects used to fit the experimental data in Fig. 5.5(b) and 5.6. †: $w = 0.015 - 0.04$ eV for degraded samples.

In our case, the interface state distributions shown in Fig. 5.2 and 5.3 can best be described with three different defects: *(A)* a continuous distribution of defects throughout the bandgap, and two Gaussian peaks centered around an energy E_0 of *(B)* 0.85 eV and *(C)* 0.50 eV above the silicon valence band edge E_v. These defects might be related to the M-shaped U_M distribution (defect A) and Gaussian defect peaks P_H (defect B) and P_L (defect C) at the c-Si/SiO$_2$ interface according to Füssel *et al.* [75]. The Gaussian peaks are modeled according to the equation

$$D_{it}(E) = D_{max} \exp\left[-\frac{(E-E_0)^2}{2w}\right], \tag{5.2}$$

where w is the peak half width and D_{max} is the peak height. Table 5.1 lists the parameters which best describe the experimental defect distributions in Fig. 5.6, and best reproduce the experimental apparent capture cross sections, as shown by the green lines in Fig. 5.5(b). The defect density pre-factors D_{max} used to fit the experimental interface state distributions in Fig. 5.6 are summarized in Tab. 5.2.

D_{max} of defect	Dimension	PA ALD initial	degraded	thermal ALD	spatial ALD
A	$\mathrm{eV^{-1}cm^{-2}}$	8×10^{10}	8×10^{10}	8×10^{10}	8×10^{10}
B	$\mathrm{eV^{-1}cm^{-2}}$	1.2×10^{11}	1.8×10^{12}	2×10^{11}	–
C	$\mathrm{eV^{-1}cm^{-2}}$	4×10^{10}	3×10^{11}	3×10^{11}	–

Table 5.2: Defect density pre-factors D_{max} used to fit the experimental interface state distributions shown in Fig. 5.6 for different Al₂O₃ ALD techniques.
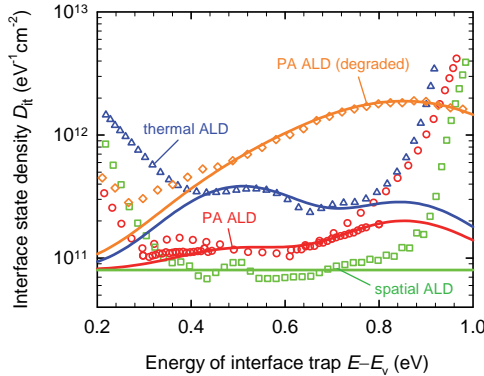

Figure 5.6: Interface state density D_{it}, obtained from C-V measurements, for Al₂O₃ deposited by plasma-assisted ALD (initial distribution: red circles, data from conductance measurements included; degraded distribution: orange diamonds), thermal ALD (blue triangles), and spatial ALD (green squares), respectively, together with calculated distributions using the parameters listed in Tab. 5.1 and 5.2.

Figure 5.6 shows the interface state density D_{it} for Al₂O₃ deposited by

plasma-assisted (initial and degraded distributions), thermal, and spatial ALD, respectively, together with calculated distributions using the parameters listed in Tab. 5.1 and 5.2. The apparent electron and hole capture cross sections expected for Al_2O_3 deposited by plasma-assisted ALD for a superposition of defects A, B, and C are shown as solid green lines in Fig. 5.5(b). The values of D_{max} and w for defects B and C were chosen to fit the experimentally determined interface state density D_{it} for different samples used for the conductance and charging transient measurements. Although this choice changes the energy dependence of the apparent capture cross sections, it does not significantly affect the values of the extracted capture cross sections of the three peaks. Note that the effect of defect C on the apparent capture cross section is limited to energies around midgap, where no experimental data is available for the electron capture cross section σ_n. Hence, any physically meaningful value of $\sigma_{n,C}$ for defect C allows to reproduce the experimental data with acceptable accuracy.

5.3 Numerical simulations of the surface recombination velocity

5.3.1 Modeling the effective surface recombination velocity

The recombination rate U_{it} via interface traps is calculated using the Shockley-Read-Hall (*SRH*) [38, 77] theory, applying the interface recombination parameters presented in Section 5.2. The second very shallow defect observed on some of the *p*-type samples was ignored. The effective interface recombination velocity (*SRV*) S_{it} as a function of excess carrier density Δn is then given by the following equation [36, 38]:

$$S_{\text{it}} = \frac{U_{\text{it}}}{\Delta n} = \left(\frac{n_{\text{s}} p_{\text{s}} - n_{\text{i}}^2}{\Delta n} \right) \int_0^{E_{\text{g}}} \left[\frac{n_{\text{s}} + n_1(E)}{\sigma_p(E)} + \frac{p_{\text{s}} + p_1(E)}{\sigma_n(E)} \right]^{-1} v_{\text{th}} D_{\text{it}}(E) \mathrm{d}E,$$

(5.3)

where Δn is the excess carrier density at the edge of the space charge region, $n_1(E) = n_{\text{i}} \exp \left[\beta(E - E_{\text{i}}) \right]$ and $p_1(E) = n_{\text{i}} \exp \left[-\beta(E - E_{\text{i}}) \right]$ are the energy-dependent SRH densities for a defect level at energy E [36], and n_{s} and p_{s} are the electron and hole concentrations at the interface, respectively. We calculate $S_{\text{it}.j}$ for each of the three defects identified in Sec. 5.2.3, applying their respective D_{it} and $\sigma_{n/p}$ values. Then, the total interface SRV is calculated from the sum of the three contributions, $S_{\text{it}} = \sum_{j=1\ldots3} S_{\text{it}.j}$. In order to calculate n_{s} and p_{s}, the charge neutrality condition at the Si surface is solved for the surface band bending ψ_{s}, as described in Sec. 3.1.3. When depositing a corona charge density Q_{c} onto the Al₂O₃ surface, the fixed charge density Q_{f} in Eq. 3.15 is replaced with the surface charge density $Q_{\Sigma} = Q_{\text{f}} + Q_{\text{c}}$. The interface-trapped charge Q_{it} is neglected in the calculations, as the acceptor or donor nature of the interface traps is unknown, and errors caused by neglecting Q_{it} are expected to be negligible compared to uncertainties and inhomogeneities in the corona charge density.

The simulated values of S_{it} are compared to experimental values of the effective surface recombination velocity, determined from the effective lifetime τ_{eff} measured using the photoconductance decay (*PCD*) and quasi-static photoconductance (*QSSPC*) methods in a Sinton Instruments WCT 120 lifetime tester. The effective SRV S_{eff} is calculated from τ_{eff} using the equation [30, 78]

$$S_{eff} = \frac{W}{2} \left[\left(\tau_{eff} - \frac{W^2}{\alpha D} \right)^{-1} - \tau_b^{-1} \right], \qquad (5.4)$$

where W is the wafer thickness, D is the minority carrier diffusion constant, the bulk lifetime τ_b is assumed to be equal to the intrinsic lifetime given by Eq. 6.12, and $\alpha = \pi^2$ for PCD [30] and $\alpha = 12$ for QSSPC [78], respectively. Further losses, for example recombination via bulk defects, are neglected. Hence, we obtain an upper limit S_{max} of the surface recombination velocity

5.3.2 Variation of surface potential

Due to the strong suppression of interface recombination caused by the excellent field-effect passivation, standard Al_2O_3-passivated lifetime samples are unsuited to compare simulated and experimental lifetime data. We use corona charging as a tool to vary the total surface charge density Q_Σ and hence vary the interface recombination rate. For a moderate or low level of field-effect passivation, S_{eff} strongly depends on Q_Σ, and spatial variations of Q_Σ have to be taken into account. We assume a Gaussian distribution of the surface charge density with a standard deviation σ_Q, which initially is given by $\sigma_Q = 2 \times 10^{11}\,\mathrm{cm}^{-2}$ obtained from conductance measurements (compare Sec. 3.3.2). During corona charging σ_Q is increased by 5% of the deposited corona charge density Q_c, which corresponds to the lateral inhomogeneity of Q_c over the active sensor area of approximately $6\,\mathrm{cm}^2$ of the WCT 120 lifetime tester. Then,

$S_{\text{eff}}(\Delta n, Q_\Sigma + \Delta Q)$ is calculated for a range of surface charge densities within 2.5 standard deviations around Q_Σ and folded with a Gaussian distribution to yield $S_{\text{eff}}(\Delta n)$.

Figure 5.7 shows the experimentally determined (black symbols) and numerically calculated (red lines) effective SRV S_{eff} for (a) 300 µm thick 1.3 Ωcm p-type Si and (b) 225 µm thick 1.0 Ωcm n-type Si, respectively, as a function of total surface charge density Q_Σ given by the sum of the fixed charge density $Q_{\text{f}} = -3.8 \times 10^{12}\,\text{cm}^{-2}$ and the deposited corona charge density Q_{c}. In this case, S_{eff} is calculated from τ_{eff} at a fixed excess carrier density of $\Delta n = 10^{15}\,\text{cm}^{-3}$, and the bulk lifetime is assumed to be equal to the intrinsic lifetime given by Eq. 6.12. Figure 5.8(a) shows the corresponding injection-level-dependent SRV $S_{\text{eff}}(\Delta n)$ for 1.3 Ωcm p-type Si and for Q_Σ values ranging from $-3.8 \times 10^{12}\,\text{cm}^{-2}$ (bottom) to 0 (top). The calculated S_{eff} values include the interface recombination velocity S_{it} and, in order to explain the injection level dependence of the lower plot ($Q_\Sigma = -3.8 \times 10^{12}\,\text{cm}^{-2}$, black line), an increased recombination in the space charge region with an electron/hole lifetime of $\tau_{n0} = 1.5 \times 10^{-6}\,\text{s}$ and $\tau_{p0} = 1.5 \times 10^{-4}\,\text{s}$, respectively [79, 80]. At lower $|Q_\Sigma|$ values interface recombination dominates and recombination in the space charge region becomes negligible. The same type of plot is shown in Fig. 5.8(b) for 1.0 Ωcm n-type Si. Due to the different surface treatment, however, the electron/hole lifetimes τ_{n0} and τ_{p0} in the space charge region are reduced by a factor of 5. Note that the assumption of a damaged space charge region is an arbitrary choice, as the injection-level dependence for large charge densities – and hence reduced interface recombination – might be due to bulk defects [81]. Furthermore, the more pronounced injection-level dependence on n-type Si might be an edge effect due to lateral transport of holes in the Al$_2$O$_3$-induced inversion layer to the highly recombination active sample edge [32].

The calculated $S_{\text{eff}}(\Delta n)$ curves are in excellent agreement with the experimental data, taking into account that recombination via bulk defects has been neglected and the experimental data only represents an upper
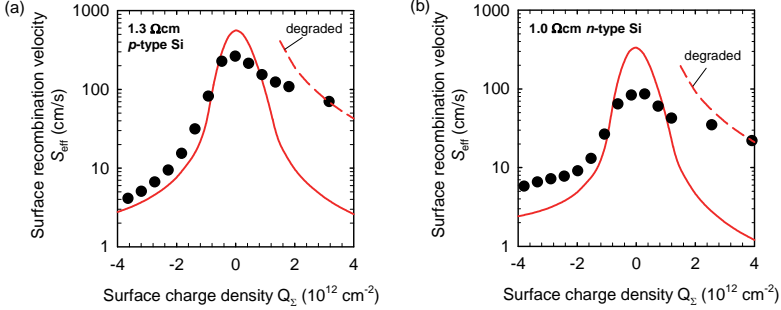
Figure 5.7: Experimentally determined (symbols) and numerically calculated (lines) effective SRV S_{eff} at an excess carrier density of $\Delta n = 10^{15}\,\text{cm}^{-3}$ for (a) 1.3 Ωcm p-type Si and (b) 1.0 Ωcm n-type Si as a function of total surface charge density Q_Σ. A degraded c-Si/Al$_2$O$_3$ interface is assumed for the dashed lines (data only shown for $Q_\Sigma > +1.5 \times 10^{12}\,\text{cm}^{-2}$).

limit to the SRV. Only for Q_Σ near zero, S_{eff} seems to be systematically overestimated, although calculation and experiment agree within the uncertainty range due to the large uncertainty in the capture cross section values. For Q_Σ near zero, S_{eff} is sensitive to small changes in Q_Σ of the order of $10^{11}\,\text{cm}^{-2}$, which is below the smallest charging step of $\Delta Q_c = (4 \pm 1) \times 10^{11}\,\text{cm}^{-2}$ in our corona setup. Furthermore, for such small surface charge densities, the interface-trapped charge Q_{it} can no longer be neglected. Hence, a slight deviation from $Q_\Sigma = 0$, or assuming a larger inhomogeneity in the deposited corona charge density, is expected to lead to a better agreement.

For large positive values of $Q_\Sigma > +10^{12}\,\text{cm}^{-2}$, S_{eff} is significantly underestimated, as shown in Fig. 5.7. We attribute this to damage occurring during corona charging, as described in Sec. 4.3.1. Figure 5.9 shows the measured and calculated injection-dependent effective SRV $S_{\text{eff}}(\Delta n)$ for $Q_\Sigma = +4 \times 10^{12}\,\text{cm}^{-2}$ for the same samples as shown in Fig. 5.7. The simulations are either based on the initial or on the degraded interface state distributions given in Tab. 5.1 and 5.2 for plasma-assisted ALD. The calculated effective SRV S_{eff} at $\Delta n = 10^{15}\,\text{cm}^{-3}$ is also shown as a
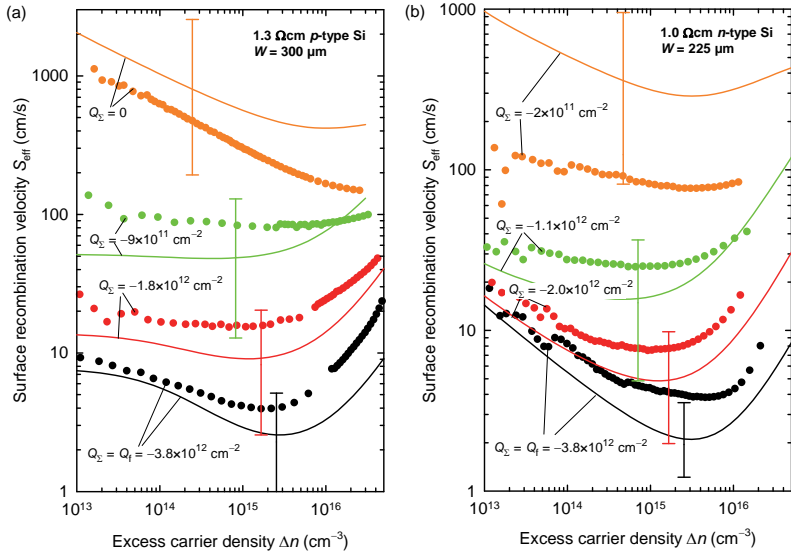
Figure 5.8: Experimentally determined (symbols) and numerically calculated (lines) injection-level-dependent effective SRV $S_{\text{eff}}(\Delta n)$ for (a) 1.3 Ωcm p-type Si and (b) 1.0 Ωcm n-type Si for different surface charge densities Q_Σ ranging from -3.8×10^{12} cm^{-2} (bottom) to 0 (top).
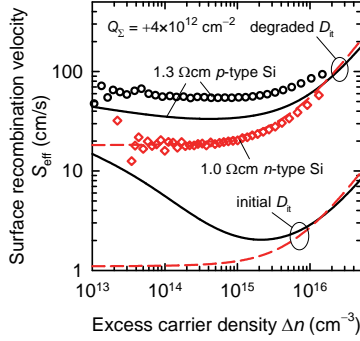
Figure 5.9: Experimentally determined (symbols) and numerically calculated (lines) injection-level-dependent effective SRV $S_{\mathrm{eff}}(\Delta n)$ for 1.3 Ωcm p-type Si (black circles and solid lines) and 1.0 Ωcm n-type Si (red squares and dashed lines) for a positive surface charge density of $Q_\Sigma = +4 \times 10^{12} \, \mathrm{cm}^{-2}$. The calculations are either based on the initial (lower lines) or on the degraded (upper lines) interface state distributions given in Tab. 5.1 and 5.2 for PA-ALD.

function of the total surface charge density Q_Σ by the dashed lines in Fig. 5.7. Assuming a degraded interface quality due to the corona charging process, the calculated $S_{\mathrm{eff}}(\Delta n)$ curves are in excellent agreement with the experimental data also for *positive* surface charge densities.

5.3.3 Simplified model assuming a single interface trap

The interface recombination rate U_{it} for a continuous distribution $D_{\mathrm{it}}(E)$ of interface traps is frequently approximated by a single interface trap level with an area density N_{it} at an energy level E_{t}, typically located in the middle of the silicon bandgap. In this case, U_{it} can be expressed as

$$U_{\mathrm{it}} = \left(np - n_{\mathrm{i}}^2\right)\left[\frac{n_{\mathrm{s}} + n_1}{S_{p0}} + \frac{p_{\mathrm{s}} + p_1}{S_{n0}}\right]^{-1}, \tag{5.5}$$

where $n_1 = N_c\exp(\frac{E_t - E_c}{k_B T})$ and $p_1 = N_v\exp(\frac{E_v - E_t}{k_B T})$. The recombination activity of the interface traps is characterized by the SRV parameters S_{n0} and S_{p0}, which are given by

$$S_{n/p.0} = v_{th}\sigma_{n/p}N_{it} = \int_0^{E_g} v_{th}\sigma_{n/p}(E)D_{it}(E)\mathrm{d}E. \qquad (5.6)$$

We derive the SRV parameters S_{n0} and S_{p0} for the Al$_2$O$_3$-passivated surfaces from the conductance measurements of the energy-dependent capture cross sections $\sigma_{n/p}(E)$ and the interface state density $D_{it}(E)$ presented in Sec. 5.2, which yields $S_{n0} = (5200 \pm 3000)\,\mathrm{cm/s}$ and $S_{p0} = (1300 \pm 1000)\,\mathrm{cm/s}$.

Sentaurus Device simulations of lifetime samples passivated on both wafer surfaces with Al$_2$O$_3$, using $S_{n0} = 5200\,\mathrm{cm/s}$ and $S_{p0} = 1300\,\mathrm{cm/s}$, yield effective SRVs in low injection of $S_{eff} = 0.6\,\mathrm{cm/s}$ on 1.5 Ωcm n-Si and $S_{eff} = 2.1\,\mathrm{cm/s}$ on 1.3 Ωcm p-Si, which agree remarkably well with experimentally determined values of $S_{eff} = 0.5\,\mathrm{cm/s}$ on 1.5 Ωcm n-Si and $S_{eff} = 2.1\,\mathrm{cm/s}$ on 1.3 Ωcm p-Si.

In this thesis, a simplified model of interface recombination is applied for the numerical simulation of inversion layer solar cells presented in Sec. 7.3. The required calculations for the Al$_2$O$_3$-passivated base can further be simplified by neglecting the fixed charge density Q_f, since the absence of noticeable surface band bending significantly reduces the complexity and time consumption of the computation. Recombination at the c-Si/Al$_2$O$_3$ interface is effectively suppressed by the negative fixed charge density Q_f due to a significantly reduced electron concentration n_s at the interface. This effect can be approximated by a reduced SRV parameter S_{n0}, neglecting the surface band bending induced by the fixed charge density Q_f. For n-type Si the best agreement between experimental data and the simplified model is found for $S_{n0} = S_{p0} = 0.5\,\mathrm{cm/s}$, which yields an effective SRV in low injection of $S_{eff} = 0.6\,\mathrm{cm/s}$ on 1.5 Ωcm n-Si. The impact of the parameter S_{p0} is negligible due to the large hole

concentration near the interface, which exceeds the electron concentration by more than 10 orders of magnitude. Accordingly, S_{p0} is arbitrarily chosen equal to S_{n0}. Please note, however, that the simplified model yields comparable values of the low-injection interface recombination velocity S_{it}, but does not account for recombination in the space charge region or "parasitic shunting" [79] at a contacted solar cell surface due to lateral hole transport in the charge-induced inversion layer.

6 Improved quantitative description of Auger recombination in c-Si

6.1 Review of Auger theory and earlier parameterization

The Auger process was first observed for atoms [82–84]. If an electron is released from an inner electronic orbital of an atom, the resulting vacancy can be occupied by an electron from an orbital with higher energy. The excess energy can be released as a photon, or, in the Auger effect, can be transferred to a second electron. The band-to-band Auger recombination in semiconductors is a generalization of the atomic Auger effect: An electron from the conduction band and a hole from the valence band recombine, and the excess energy is transferred to a third charge carrier. This third charge carrier can either be an electron (*eeh* process) or a hole (*ehh* process).

The Auger recombination process in silicon plays an important fundamental role: While extrinsic recombination, e.g. via bulk defects or at the wafer surface, can in principle be avoided by a sufficiently advanced device technology, Auger recombination is an intrinsic effect and ultimately limits the device performance. In addition, intrinsic radiative recombination is relatively weak in silicon, as silicon is an indirect semiconductor, making Auger recombination the dominant intrinsic recombination process in most practical cases. The radiative recombination only starts to dominate for low dopant concentrations, where intrinsic recombination is typically negligible compared to extrinsic recombination (see Fig. 6.3 for a comparison of the radiative and Auger lifetimes with the highest lifetime values ever measured in silicon).

In the theoretical treatment of the Auger process, the involved charge carriers have traditionally been assumed to be non-interacting quasi-free particles, which yields a recombination rate proportional to the densities of the involved charge carriers. Accordingly, the total net Auger recombination rate, which is the sum of the net Auger recombination rates of the *eeh* and *ehh* processes, is given by [85]

$$U_{\text{Auger}} = C_n \left(n^2 p - n_{\text{i}}^2 n_0 \right) + C_p \left(np^2 - n_{\text{i}}^2 p_0 \right), \tag{6.1}$$

where C_n and C_p are the Auger recombination coefficients for the *eeh* and *ehh* processes, respectively. Commonly, $C_n = 2.8 \times 10^{-31}$ cm^6/s and $C_p = 9.9 \times 10^{-32}$ cm^6/s [86] are used for the Auger recombination coefficients at 300 K. The traditional theory of Auger recombination agrees very well with experimental lifetime data for highly doped silicon with dopant concentrations above 5×10^{18} cm^{-3}. For lower dopant concentrations, however, the Auger recombination rate is significantly underestimated [86]. Deviations from the traditional Auger theory were also observed in high-injection measurements on lowly-doped silicon ($\Delta n < 2 \times 10^{17}$ cm^{-3}), were the ambipolar Auger coefficient was found to be several times larger than the theoretically expected value of $C_n + C_p$ [87]. Hangleiter and Häcker [88] attributed this deviation to a correlation of the involved charge carriers due to Coulomb interaction. The correlated electrons and holes can form bound states (e.g. excitons) and scattering states. The exciton formation dominates for charge carrier densities below the Mott transition [89] (for silicon $\approx 10^{18}$ cm^{-3} at 300 K), which results in an increased charge carrier density in the vicinity of an oppositely charged carrier. As a result, the Auger recombination rate increases. For charge carrier densities above the Mott transition, exciton formation is suppressed due to screening of the Coulomb interaction and the Auger recombination rate converges to the traditional Auger theory. This *Coulomb-enhanced Auger recombination* (*CE-AR*) can be described by multiplying the Auger coefficients C_n and C_p with enhancement factors g_{eeh} and g_{ehh}, respectively. Based on lifetime measurements, Altermatt et al. proposed an empirical parametrization of the enhancement factors

for low-injection conditions [90]:

$$g_{\text{eeh}}(n, T) = 1 + \left[g_{\text{max.n}}(T) - 1\right] \left\{1 - \tanh\left[\left(\frac{n}{N_{0.\text{eeh}}}\right)^{0.34}\right]\right\}, \quad (6.2)$$

$$g_{\text{ehh}}(p, T) = 1 + \left[g_{\text{max.p}}(T) - 1\right] \left\{1 - \tanh\left[\left(\frac{p}{N_{0.\text{ehh}}}\right)^{0.29}\right]\right\}, \quad (6.3)$$

where $g_{\text{max.n}} = 235548\, T^{-1.5013}$, $g_{\text{max.p}} = 564812\, T^{-1.6546}$, and $N_{0.\text{eeh}} = N_{0.\text{ehh}} = 5 \times 10^{16}\,\text{cm}^{-3}$. At $T = 300\,\text{K}$, $g_{\text{max.n}} = g_{\text{max.p}} = 45$.

Auger recombination cannot be directly measured, unlike radiative recombination [91, 92], and the underlying physical mechanisms are not yet understood well enough to allow a full theoretical description. Therefore, empirical parameterizations based on carrier lifetime measurements are used. In order to quantify Auger recombination, competing extrinsic recombination channels – for high-quality float-zone-grown Si mainly surface recombination – are neglected and the measured lifetime is directly identified with the intrinsic lifetime. Obviously, the accuracy of this approach strongly depends on the quality of the surface passivation. A review of earlier parameterizations is given in Ref. [13].

Prior to this study, the parametrization proposed by Kerr and Cuevas [13] was most widely used. In their parametrization, the intrinsic lifetime of silicon at $300\,\text{K}$ is given by

$$\tau_{\text{intr.Kerr}} = \frac{\Delta n}{np\left(C_n n_0^{0.65} + C_p p_0^{0.65} + C_a \Delta n^{0.8} + B\right)}, \quad (6.4)$$

where $C_n = 1.8 \times 10^{-24}$, $C_p = 6 \times 10^{-25}$, $C_a = 3 \times 10^{-27}$, and $B = 9.5 \times 10^{-15}$; all densities (n, p, n_0, p_0, and Δn) are in units of $1\,\text{cm}^{-3}$ and $\tau_{\text{intr.Kerr}}$ is in units of $1\,\text{s}$.

Over the last years, the quality of silicon surface passivation has improved continuously. In particular, Al_2O_3 surface passivation layers have demonstrated an excellent level of surface passivation on lowly and moderately

doped p- and n-type c-Si, which allows to investigate silicon bulk recombination with high precision. Recently, effective lifetimes exceeding the intrinsic lifetime limit according to Kerr's parametrization have been measured in this study and also by other authors [93–95]. As a consequence, it is necessary to revise the quantitative description of Auger recombination in silicon based on the improved surface passivation.

6.2 Lifetime measurements of silicon samples of various dopant concentrations

6.2.1 Sample selection and measurement techniques

We study the intrinsic recombination of c-Si as a function of dopant concentration and excess carrier density by means of injection-dependent lifetime measurements on a wide selection of well-passivated c-Si wafers. Symmetrically passivated lifetime samples have been prepared and analyzed at Fraunhofer ISE and ISFH in parallel, in order to reduce systematic errors and generate a larger set of data.[‡] We use shiny-etched (100)-oriented boron-doped p-type and phosphorus-doped n-type floatzone (FZ) c-Si wafers as well as KOH-etched phosphorus-doped n-type Czochralski (Cz) c-Si wafers, with dopant concentrations ranging from $4.6 \times 10^{13}\,\mathrm{cm}^{-3}$ to $2.5 \times 10^{17}\,\mathrm{cm}^{-3}$. The wafer thickness ranges from $180\,\mu\mathrm{m}$

[‡]The data and analysis presented in this chapter result from a cooperation between ISFH and Fraunhofer ISE, based on experiments and analysis carried out by A. Richter (Fraunhofer ISE) and F. Werner (ISFH), see Ref. 81. The experimental and evaluation methods were discussed and agreed upon by both scientists based on all available data. In order to derive a unique and consistent parameterization, A. Richter has been responsible for the final version of the proposed improved parameterization of Auger recombination in silicon. Graphs, data, and equations presented in this chapter are mostly based on Ref. 81. Additional measurements by F. Werner, which are not included in the analysis as they duplicate measurements by Fraunhofer ISE, are consistent with the parameterization presented in this chapter.

to 300 µm, some wafers have been further thinned by mechanical grinding. Details of the wafer properties and of the lifetime measurements are summarized in Table 1 in the appendix.

At ISFH the wafers were cleaned according to the standard RCA cleaning sequence. All wafers are passivated with 10 nm of Al_2O_3, deposited by plasma-assisted ALD in an OXFORD INSTRUMENTS FLEXAL reactor, and subsequently annealed at 425 °C for 15 min in a nitrogen ambient. At Fraunhofer ISE the wafers were cleaned in an HNO_3 solution, followed by an HF-dip, and then passivated either with 30 nm of Al_2O_3 deposited by plasma-assisted ALD in an OXFORD INSTRUMENTS OPAL reactor, or with 70 nm of SiN_x deposited by microwave-induced plasma-enhanced chemical vapor deposition (*PECVD*) in a ROTH & RAU AK800 reactor. The Al_2O_3-passivated wafers were annealed at 440 °C for 25 min in a forming gas (N_2/H_2) ambient.

The effective carrier lifetime τ_{eff} is measured as a function of excess carrier density Δn by two different techniques: *(i)* photoluminescence (*PL*) under quasi-steady-state (*QSSPL*) or steady-state (*SSPL*) conditions, and *(ii)* transient photoconductance decay (*PCD*) or quasi-steady-state photoconductance (*QSSPC*). More details about the procedure of the lifetime measurements are given in Ref. 81. For a meaningful analysis of the data, the wafer thickness W and the dopant concentration N_{dop} need to be known. The wafer thickness W was determined with a relative accuracy of 1 % using either a contactless wafer geometry gauge (E+H METROLOGY) or using a dial indicator. The dopant concentration N_{dop} was determined from four-point probe measurements of the bulk resistivity with an estimated relative accuracy of 5 % using the Klaassen model [97] for the bulk mobilities.

6.2.2 Uncertainty range of the lifetime measurements

We estimate the uncertainty of our lifetime measurements by comparing independent lifetime measurements at different institutes, applying dif-

ferent measurement techniques. We define the relative deviation δ of the effective lifetime τ_x relative to a given lifetime τ_0 by the equation

$$\delta = \frac{\tau_x}{\tau_0} - 1. \tag{6.5}$$

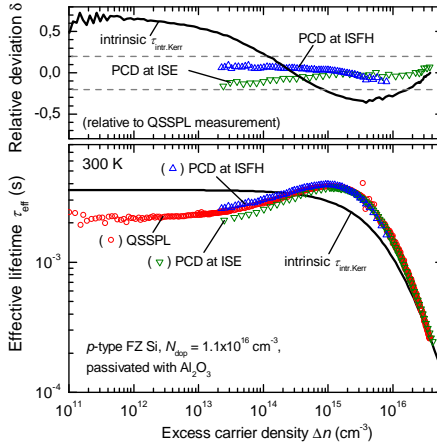Depending on the context, the absolute value $|\delta|$ might be refered to as relative deviation as well.

Figure 6.1: Injection-dependent effective carrier lifetime determined for the same Al$_2$O$_3$-passivated sample using different lifetime measurement techniques at different laboratories. The solid line corresponds to the intrinsic lifetime according to Kerr and Cuevas [13]. The upper graph shows the relative deviation δ of the different lifetime values with respect to the QSSPL measurement in the lower graph. The dashed gray lines indicate the estimated measurement uncertainty of $\pm 20\,\%$.

Figure 6.1 shows the injection-dependent effective carrier lifetime $\tau_{\text{eff}}(\Delta n)$ for an Al$_2$O$_3$-passivated 1.34 Ωcm p-type FZ c-Si sample measured by PCD at ISFH (blue triangles up), and by PCD (green triangles down) and QSSPL (red circles) at Fraunhofer ISE, respectively. The intrinsic lifetime $\tau_{\text{intr.Kerr}}$ according to the parametrization of Kerr and Cuevas (Ref. 13, Eq. 6.4) is given by the solid line. The relative deviation of $\tau_{\text{intr.Kerr}}$ and

of the PCD measurements relative to the QSSPL measurement are shown in the upper graph. All measurements are in good agreement, especially for high excess carrier densities $\Delta n > 10^{15}\,\mathrm{cm}^{-3}$, where the relative deviation is below 10 %. It is important to note that this good agreement is observed for two measurement techniques based on different physical processes, which require the knowledge of different material parameters (carrier mobility for PCD and coefficient of radiative recombination for QSSPL) as a function of photogenerated excess carrier density Δn in the analysis. Accordingly, the good agreement in Fig. 6.1 demonstrates that both τ_{eff} and Δn can be extracted consistently from the experimental data. Based on these results we estimate an uncertainty range of the lifetime measurements of ± 20 %, indicated by the gray dashed lines in Fig. 6.1. For excess carrier densities $\Delta n > 5 \times 10^{14}\,\mathrm{cm}^{-3}$ the measured effective lifetime – and hence necessarily the "true" intrinsic lifetime τ_{intr} – clearly exceeds $\tau_{\mathrm{intr.Kerr}}$ according to Eq. 6.4. The relative deviation is as large as 36 % around $\Delta n \approx 3 \times 10^{15}\,\mathrm{cm}^{-3}$, which cannot be explained by uncertainties in the lifetime measurements. One may expect that $\tau_{\mathrm{intr.Kerr}}$ significantly underestimates the "true" intrinsic lifetime also for lower excess carrier densities, as the reduced measured effective lifetime at lower excess carrier densities is attributed to defect recombination and presumably is not an intrinsic effect.

6.2.3 Effective lifetime as a function of dopant concentration and injection density

Auger recombination over a wide range of dopant concentrations and excess carrier densities in *p*- and *n*-type Si is analyzed based on selected samples showing the highest measured carrier lifetimes. Figure 6.2 shows the measured effective lifetimes as a function of excess carrier density for two representative sets of samples for *p*-type (a) and *n*-type (b) silicon. As expected from the Auger recombination theory, the high-injection effective lifetime decreases drastically with increasing excess carrier density for almost all samples. The only exception is the 0.10 Ωcm *p*-Si sample,

where sufficiently high excess carrier densities could not be realized experimentally due to the low effective lifetime.
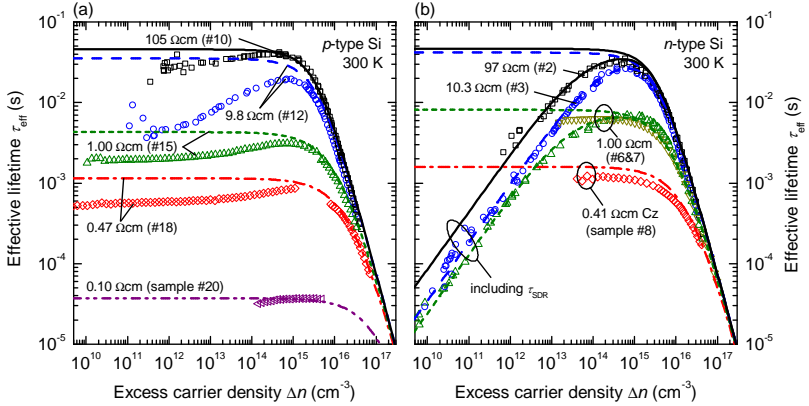

Figure 6.2: Effective lifetime as a function of the excess carrier density for *p*-type (a) and *n*-type (b) c-Si wafers of various bulk resistivities. The bulk resistivity and sample number according to Table 1 are given in the graph for each sample. Lines represent the modeled effective lifetimes according to Eq. 6.6, which includes $\tau_{\text{intr.adv}}$ and $\tau_{\text{SRH}} = 47\,\text{ms}$. For the *n*-type silicon samples, the modeled effective lifetime including recombination in the SCR according to Eq. 6.11 is shown as well. Samples #7 and #8 are passivated with SiN_x, all other samples are passivated with Al_2O_3.

For most samples, the effective lifetime decreases towards low excess carrier densities as well, which is attributed to extrinsic recombination. For the Al_2O_3-passivated *p*-type samples, the effective lifetime saturates in low injection, which can be well described by a SRH defect recombination. For the Al_2O_3-passivated *n*-type samples, on the other hand, the effective lifetime decreases over several orders of magnitude and does not saturate in low injection. This behavior is well described by increased recombination due to surface-near damage within the space charge region (*SCR*) [79, 80], or by lateral hole transport in a hole inversion layer to the recombination-active sample edge [32]. A SCR and an inversion layer

form on *n*-Si due to the fixed negative charge density at the c-Si/Al$_2$O$_3$ interface. This interpretation is supported by lifetime measurements of SiN$_x$-passivated *n*-Si samples, where fixed positive charges prevent the formation of a SCR on *n*-Si, and which, accordingly, do not show a decreasing lifetime in low injection.

Figure 6.3 shows the maximum measured effective lifetime of all *p*- and *n*-type samples as a function of the dopant concentration, in comparison to literature data from Ref. 72, 86, 98–103. In addition, the radiative lifetime according to Altermatt *et al.* [104] and the low-injection free-particle Auger lifetime – with the Auger coefficients according to Dziewior and Schmid [86] – are also given. Three different regimes for different ranges of dopant concentrations can be distinguished in the lifetime data in Fig. 6.3:

1. For dopant concentrations $N_{\mathrm{dop}} > 5 \times 10^{18}\,\mathrm{cm}^{-3}$, all lifetime data agrees well with the free-particle Auger lifetime, as expected due to the screening of the Coulomb interaction for dopant concentrations above the Mott transition around $N_{\mathrm{dop}} \approx 10^{18}\,\mathrm{cm}^{-3}$.

2. For dopant concentrations in the range of $5 \times 10^{15}\,\mathrm{cm}^{-3} - 10^{17}\,\mathrm{cm}^{-3}$, the maximum measured lifetime values stay below the free-particle Auger lifetime and form a straight-line region corresponding to the Coulomb-enhanced Auger-recombination (*CE-AR*).

3. For $N_{\mathrm{dop}} < 2 \times 10^{15}\,\mathrm{cm}^{-3}$, the maximum measured lifetime values stay significantly below the CE-AR line, which we attribute to extrinsic recombination. Accordingly, recombination in this case is dominated by SRH bulk or surface recombination, not by intrinsic recombination.
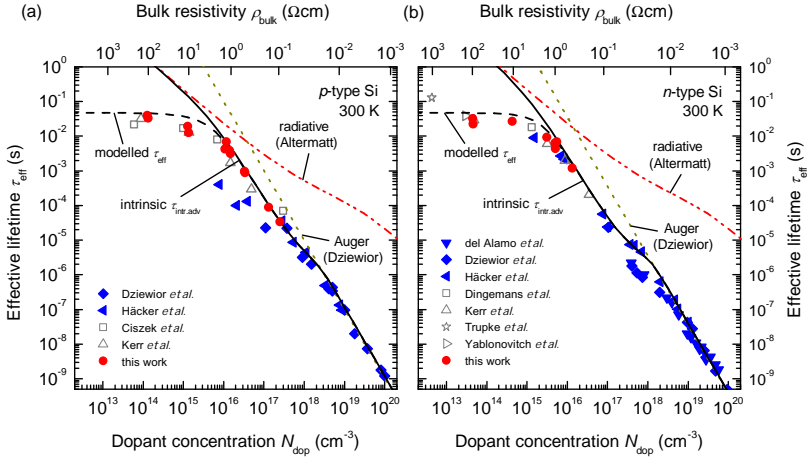
Figure 6.3: Maximum effective lifetime as a function of the dopant concentration, measured at 300 K on p-type (a) and n-type (b) silicon (red circles), together with literature data from Ref. 72, 86, 98–103 (solid symbols: data considered in extracting the Auger recombination rate; open symbols: not considered, given as a reference). The solid black line represents the intrinsic lifetime limit according to Eq. 6.12, the dashed black line additionally includes $\tau_{\mathrm{extr}} = 47$ ms. The radiative lifetime according to Altermatt *et al.* [104] and the low-injection free-particle Auger lifetime with the Auger coefficients according to Dziewior and Schmid [86] are also given.

6.3 Extraction of the Auger recombination rate from measured lifetime data

We model the effective carrier lifetime τ_{eff} by taking into account four different recombination channels: intrinsic radiative recombination (quantified by the corresponding lifetime τ_{rad}), intrinsic Auger recombination (τ_{Auger}), and extrinsic recombination in the bulk ($\tau_{\text{bulk.SRH}}$) and at the wafer surfaces (τ_{surf}). Accordingly, the effective lifetime can be expressed as

$$\frac{1}{\tau_{\text{eff}}} = \frac{1}{\tau_{\text{rad}}} + \frac{1}{\tau_{\text{Auger}}} + \frac{1}{\tau_{\text{bulk.SRH}}} + \frac{1}{\tau_{\text{surf}}} = \frac{1}{\tau_{\text{intr}}} + \frac{1}{\tau_{\text{extr}}}, \quad (6.6)$$

where

$$\frac{1}{\tau_{\text{intr}}} \equiv \frac{1}{\tau_{\text{rad}}} + \frac{1}{\tau_{\text{Auger}}}, \quad \text{and} \quad \frac{1}{\tau_{\text{extr}}} \equiv \frac{1}{\tau_{\text{bulk.SRH}}} + \frac{1}{\tau_{\text{surf}}}. \quad (6.7)$$

The recombination rate U of a given recombination channel, the recombination coefficient C, and the corresponding lifetime τ are related by the following equations:

$$\tau = \frac{\Delta n}{U}, \quad \text{and} \quad U = C\left(np - n_{\text{i.eff}}^2\right). \quad (6.8)$$

The effective intrinsic carrier concentration $n_{\text{i.eff}} = n_{\text{i}} \exp\left(\frac{1}{2}\beta\Delta E_{\text{g}}\right)$ accounts for the bandgap narrowing ΔE_{g} and is calculated according to the random-phase approximation proposed by Schenk [105]. The intrinsic carrier concentration n_{i} is chosen according to the value measured by Misiakos and Tsamakis, which is $n_{\text{i}} = 9.7 \times 10^9 \, \text{cm}^{-3}$ at $300 \, \text{K}$ [106].

6.3.1 Radiative recombination

Kerr's intrinsic lifetime limit according to Eq. 6.4 includes the radiative recombination in silicon according to Schlangenotto *et al.* [91], who have measured a radiative recombination coefficient of $B = 9.5 \times 10^{-15} \, \text{cm}^3/\text{s}$

in silicon at 300 K. In the meantime, the description of radiative recombination has been improved: The radiative recombination coefficient B has been measured for lowly doped silicon by Trupke *et al.* [92], who have obtained a value of $B_{\text{low}} = 4.73 \times 10^{-15}\,\text{cm}^3/\text{s}$ at 300 K. We also take into account Coulomb-enhanced radiative recombination based on a model proposed by Altermatt *et al.* [107], where B_{low} is multiplied by a factor B_{rel}. A parameterization of $B_{\text{rel}}(n, p)$ is given in Ref. [104]. With this data the lifetime of the radiative recombination is described by

$$\frac{1}{\tau_{\text{rad}}} = \frac{\left(np - n_{\text{i.eff}}^2\right)}{\Delta n} B_{\text{low}}\, B_{\text{rel}}(n, p). \tag{6.9}$$

6.3.2 Extrinsic recombination

Figure 6.3 suggests that for dopant concentrations below $\approx 5 \times 10^{15}\,\text{cm}^{-3}$, recombination in the samples analyzed in this study and in the literature is no longer dominated by intrinsic recombination. In this experiment, maximum effective lifetimes up to 32 ms and 40 ms were measured for the lowest-doped n-type ($N_{\text{dop}} = 4.6 \times 10^{13}\,\text{cm}^{-3}$) and p-type ($N_{\text{dop}} = 1.3 \times 10^{14}\,\text{cm}^{-3}$) samples, respectively, as shown in Fig. 6.2 and 6.3. These effective lifetimes correspond to a maximum SRV as low as $S_{\text{max}} = 0.3\,\text{cm/s}$, if bulk recombination was negligible. For samples with higher dopant concentrations a maximum SRV of the order of 1 cm/s or below is feasible as well (compare Sec. 5.3). Hence, the excellent surface passivation quality of Al_2O_3 in most cases allows to neglect surface recombination, and we are able to describe intrinsic bulk recombination very precisely.

For dopant concentrations below $\approx 5 \times 10^{15}\,\text{cm}^{-3}$, extrinsic recombination cannot be neglected. Furthermore, the measured lifetime of the Al_2O_3-passivated n-type Si samples shown in Fig. 6.2 exhibits a strong injection dependence in low injection.

Rather than trying to accurately model the injection-dependent extrinsic

lifetime, we assume a constant extrinsic lifetime τ_{extr} for all samples, independent of dopant concentration N_{dop} or excess carrier density Δn. We discard all low-injection lifetime data of lowly-doped silicon, where recombination is clearly dominated by extrinsic recombination. Accordingly, our model of the extrinsic recombination does not significantly affect the parameterization of intrinsic recombination derived in Section 6.3.3. However, this choice of a constant τ_{extr} is equivalent to the assumption that the low-injection intrinsic lifetime does not significantly vary with excess carrier density. The extrinsic lifetime τ_{extr} is chosen as the highest lifetime value, corrected for radiative recombination, measured for the *p*-Si sample with the highest effective lifetime (sample #10 in Table 1 in the Appendix), i.e.

$$\tau_{\text{extr}} \equiv \max\left[\left(\frac{1}{\tau_{\text{eff.}\#10}} - \frac{1}{\tau_{\text{rad.}}}\right)^{-1}\right] = 47\,\text{ms}. \qquad (6.10)$$

The same maximum lifetime of 47 ms is obtained from the lifetime data of the *n*-Si sample (sample #2) with the highest measured lifetime, if the measured lifetime values are corrected for radiative recombination and recombination in the SCR according to Eq. 6.11. Accordingly, the same value of $\tau_{\text{extr}} = 47$ ms applies to both *p*- and *n*-type Si. The dashed black lines in Fig. 6.3 show that this value is well suited to describe the measured maximum effective lifetime as a function of dopant concentration. It should be mentioned that an even higher lifetime of 130 ms has been reported by Trupke *et al.* [99] for ultra-lowly-doped *n*-type Si. Due to the rare data for $N_{\text{dop}} < 10^{13}\,\text{cm}^{-3}$, this result is not taken into account and the more conservative value of 47 ms is used.

The measured lifetime of the Al_2O_3-passivated *n*-type Si samples shown in Fig. 6.2 exhibits a strong injection dependence in low injection, which is related to the formation of an inversion layer and a space charge region for Al_2O_3-passivated *n*-Si and SiN_x-passivated *p*-Si due to the negative (Al_2O_3) or positive (SiN_x) fixed charge densities, respectively [32, 79, 80]. Rather than solving for the depth-dependent band bending at the c-Si

surface we employ a simplified approach and describe the additional recombination by means of a recombination current density prefactor J_0 and an ideality factor m according to the following equation [79, 108]:

$$\frac{1}{\tau_{\mathrm{SCR}}} = \frac{2J_0}{\Delta n q W} \left[\left(\frac{\Delta n}{n_{0.\mathrm{min}}} + 1 \right)^{\frac{1}{m}} - 1 \right], \qquad (6.11)$$

where $n_{0.\mathrm{min}}$ is the minority carrier concentration in thermal equilibrium. The values of J_0 and m are determined for each Al_2O_3-passivated n-Si sample separately by fitting Eq. 6.11 to the measured low-injection lifetime. The resulting values are summarized in Tab. 2 in the Appendix. The lifetime values according to this model are shown in Fig. 6.2(b) and agree very well with the experimental lifetime data in low-injection.

6.3.3 New parameterization of Auger recombination

We quantitatively describe intrinsic recombination in silicon based on our measurements of the effective lifetime of lowly and moderately doped n- and p-type c-Si, together with literature data for highly doped silicon [86, 101, 102]. All lifetime data is summarized in Figs. 6.2 and 6.3, details of the samples prepared for this study are summarized in Table 1 in the appendix.

Our improved parameterization is based on a polynomial expression similar to that of Kerr and Cuevas (Ref. 13, Eq. 6.4), but includes enhancement factors g_{eeh} and g_{ehh} based on Altermatt's parametrization ([90], Eqs. 6.2 and 6.3). The Coulomb-enhanced radiative recombination is included by the product $B_{\mathrm{low}} B_{\mathrm{rel}}$. Therefore, the resulting parameterization includes all intrinsic recombination channels in silicon.

The parameterization of the intrinsic lifetime in high-injection is based on lifetime data for excess carrier densities $\Delta n \gtrsim 5 \times 10^{15}\,\mathrm{cm}^{-3}$, where recombination is dominated by intrinsic recombination for all investigated samples. In low-injection, the parameterization is based on lifetime data

for dopant concentrations $N_{\text{dop}} \gtrsim 5 \times 10^{15}\,\text{cm}^{-3}$, as the measured effective lifetime for samples with lower dopant concentrations approaches $\tau_{\text{extr}} = 47\,\text{ms}$ and hence is dominated by extrinsic recombination.

The resulting intrinsic recombination lifetime $\tau_{\text{intr.adv}}$ of the charge carriers in silicon at $300\,\text{K}$, as a function of the excess carrier density Δn and the charge carrier densities n_0 and p_0 in thermal equilibrium, is given by the following equation:

$$\tau_{\text{intr.adv}} = \frac{\dfrac{\Delta n}{\left(np - n_{\text{i.eff}}^2\right)}}{\left(2.5 \times 10^{-31} g_{\text{eeh}} n_0 + 8.5 \times 10^{-32} g_{\text{ehh}} p_0 + 3.0 \times 10^{-29} \Delta n^{0.92} + B_{\text{rel}} B_{\text{low}}\right)} \tag{6.12}$$

with the enhancement factors

$$g_{\text{eeh}}(n_0) = 1 + 13 \left\{ 1 - \tanh\left[\left(\frac{n_0}{N_{0.\text{eeh}}}\right)^{0.66}\right] \right\} \tag{6.13}$$

and

$$g_{\text{ehh}}(p_0) = 1 + 7.5 \left\{ 1 - \tanh\left[\left(\frac{p_0}{N_{0.\text{ehh}}}\right)^{0.63}\right] \right\}, \tag{6.14}$$

where $N_{0.\text{eeh}} = 3.3 \times 10^{17}\,\text{cm}^{-3}$ and $N_{0.\text{ehh}} = 7 \times 10^{17}\,\text{cm}^{-3}$. All densities ($n$, p, n_0, p_0, and Δn) are in units of $1\,\text{cm}^{-3}$, B_{low} is in units of $1\,\text{cm}^3/\text{s}$, B_{rel} is dimensionless, and $\tau_{\text{intr.adv}}$ is in units of $1\,\text{s}$. Several simplifications of Eq. 6.12 are discussed in Ref. 81.

6.4 Approximation of intrinsic recombination in Sentaurus Device

The improved parameterization of intrinsic recombination in silicon has not yet been implemented in SENTAURUS DEVICE, which is used for

the numerical simulations presented in Chapter 7. Instead, the intrinsic recombination rate R_{intr} is implemented by the following parametrization [109, p. 366]:

$$R_{\text{intr}} = \left(C_n n + C_p p \right) \cdot \left(np - n_{\text{i.eff}}^2 \right), \qquad (6.15)$$

$$C_n = A_n \left[1 + H_n \exp\left(-\frac{n}{N_0} \right) \right], \quad C_p = A_p \left[1 + H_p \exp\left(-\frac{p}{N_0} \right) \right]. \tag{6.16}$$

The best fit of Eq. 6.15 and 6.16 to our new parameterization of intrinsic recombination, given by Eq. 6.12, is obtained for $A_n = 2.5 \times 10^{-31}\,\text{cm}^6/\text{s}$, $A_p = 8.5 \times 10^{-32}\,\text{cm}^6/\text{s}$, $H_n = 11.4$, $H_p = 7.5$, and $N_0 = 2.95 \times 10^{17}\,\text{cm}^{-3}$. We account for extrinsic bulk recombination assuming a single defect at midgap with lifetime parameters of $\tau_{n0} = \tau_{n0} = 50\,\text{ms}$.

Figure 6.4 shows the relative deviation $\delta = \tau_{\text{approx}}/\tau_{\text{intr}} - 1$ of our approximation implemented in Sentaurus Device, given by Eq. 6.15, and our improved parameterization of intrinsic recombination, given by Eq. 6.12, as a function of dopant concentration N_{dop} for various excess carrier densities Δn for p- and n-type Si. For dopant concentrations below $10^{17}\,\text{cm}^{-3}$ on p-Si and below $10^{15}\,\text{cm}^{-3}$ on n-Si, the intrinsic lifetime for $\Delta n \leq 10^{14}\,\text{cm}^{-3}$ is well described by the approximation. A good agreement is also found for highly doped Si with $N_{\text{dop}} > 5 \times 10^{18}\,\text{cm}^{-3}$. For other parameters, mainly two significant deviations are observed:

1. For lowly and moderately doped p- and n-type Si, the intrinsic lifetime is *underestimated* for excess carrier densities exceeding $\Delta n \approx 10^{14}\,\text{cm}^{-3}$.

2. In the range of $N_{\text{dop}} \approx 5 \times 10^{16} - 5 \times 10^{18}\,\text{cm}^{-3}$ for p-type Si, and to a lesser extend also for n-type Si, the approximation deviates significantly from the intrinsic lifetime for all excess carrier densities. As these dopant concentrations are typically found in emitters

or "surface fields", the surface recombination velocity can be varied to yield the desired saturation current density, thereby partly balancing the incorrect bulk lifetime.
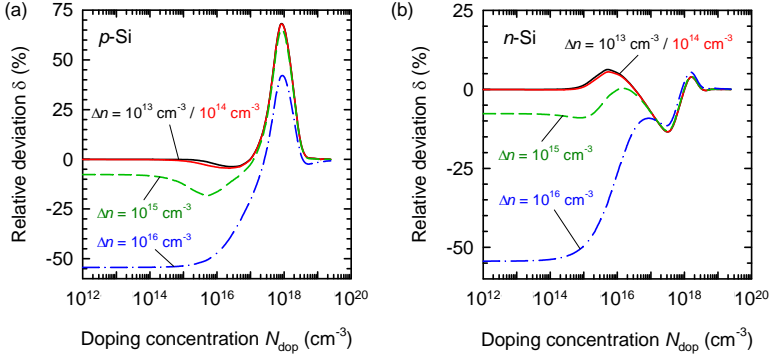

Figure 6.4: Relative deviation $\delta = \tau_{\mathrm{approx}}/\tau_{\mathrm{intr}} - 1$ of the approximation implemented in SENTAURUS DEVICE, given by Eq. 6.15, and the improved parameterization of intrinsic recombination, given by Eq. 6.12, as a function of dopant concentration N_{dop} for (a) p-type Si and (b) n-type Si. Values of $\delta < 0$ indicate that the intrinsic lifetime is underestimated by the approximation. The values of the excess carrier density are $\Delta n = 10^{13}\,\mathrm{cm}^{-3}$ and $10^{14}\,\mathrm{cm}^{-3}$ (black and red solid lines), $10^{15}\,\mathrm{cm}^{-3}$ (green dashed lines), and $10^{16}\,\mathrm{cm}^{-3}$ (blue dash-dotted lines), respectively.

For the simulations of inversion layer emitter solar cells presented in Sec. 7.3, where a $4.6\,\Omega\mathrm{cm}$ n-type Si base ($N_{\mathrm{dop}} = 10^{15}\,\mathrm{cm}^{-3}$) is considered, these parameters result in a maximum relative deviation of $\delta = \left|\tau_{\mathrm{approx}}/\tau_{\mathrm{intr}} - 1\right| < 1\%$ for $\Delta p < 3\times10^{14}\,\mathrm{cm}^{-3}$. For larger excess carrier densities the intrinsic lifetime is underestimated and the relative deviation increases up to 10% at $\Delta p = 10^{15}\,\mathrm{cm}^{-3}$ and 50% at $\Delta p = 10^{16}\,\mathrm{cm}^{-3}$. For open-circuit voltages of approximately $730-750\,\mathrm{mV}$, this corresponds to an underestimation of the open-circuit voltage by 2% relative. Hence, the efficiency is underestimated as well by 2% relative, or approximately $0.4 - 0.5\%$ absolute.

7 Inversion layer solar cells on *n*-type c-Si

The presence of a sufficiently high charge density at the surface of a silicon wafer of opposite polarity (negative charges on *n*-type Si, or positive charge on *p*-type Si) induces an inversion layer (*IL*) near the silicon surface, which can form the emitter of an inversion layer solar cell.

In the past, inversion layer solar cells on *p*-type silicon have been intensively studied [110–113]. These devices were most successfully implemented based on an MIS tunneling contact in the metalized areas, and an inversion layer based on the positive fixed charges contained in a silicon nitride (SiN_x) film in the un-metalized areas. Inversion at the silicon surface was further enhanced by the incorporation of cesium (Cs). On *n*-type silicon the negative fixed charges at the c-Si/Al_2O_3 interface induce a hole inversion layer (p^+-IL) close to the surface, which can be used as an emitter in inversion layer solar cells made on *n*-type silicon wafers. This allows combining the advantages of *n*-type Si wafers, such as very high carrier lifetimes and excellent stability, with a simple and cost efficient process for emitter formation and the excellent surface passivation provided by Al_2O_3.

7.1 Aluminum-doped laser contacts

An isolating Al_2O_3 layer deposited on top of a Si wafer needs to be opened at least locally in order to contact the Si base or the p^+ inversion layer near the surface of the *n*-Si wafer. As the IL will be interrupted in the contact openings, it is important to ensure type inversion underneath the metal contacts by suitable means. We achieve this by applying a single-

pulse laser-doping process [114–116], which serves to locally ablate the Al_2O_3 layer and – at the same time – creates an aligned local Al-doped p^+ region (Al-p^+) underneath the contact in a single process step. The Al_2O_3 layer is locally ablated using a frequency-doubled Nd:YVO$_4$ laser with a wavelength of 355 nm, a pulse length of 30 ns, and a repetition rate of 50 kHz. During the laser ablation process, the silicon underneath the laser spot melts and then recrystallizes. Local Al-p^+ regions extending $0.5 - 1 \, \mu m$ into the silicon are formed in the laser spot [116], whereby aluminum from the Al_2O_3 layer acts as dopant source. The samples are cleaned in boiling $NH_4OH/H_2O/H_2O_2$ and $HCl/H_2O/H_2O_2$ for 30 s each, in order to remove residues from the contact openings, which significantly reduces the contact resistance. The cleaning sequence needs to be kept short to preserve the Al_2O_3 layer, which exhibits etching rates of up to $10 \, nm/min$ in ammonia. Al front contacts are then evaporated with an electron gun using a Ni shadow mask. No post-metalization anneal is required in order to achieve a good ohmic electrical contact.
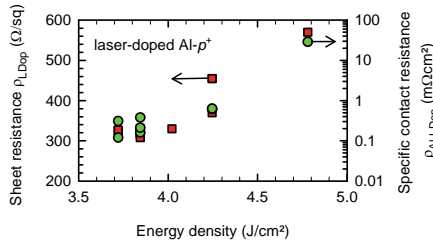

Figure 7.1: Sheet resistance ϱ_{LDop} (red squares, left axis) and specific contact resistance $\varrho_{Al\text{-}LDop}$ (green circles, right axis) of a laser-doped Al-p^+ region as a function of the energy density of the laser pulse. The sample is contacted with evaporated Al. No post-metalization anneal is performed.

Figure 7.1 shows the sheet resistance of the laser-doped Al-p^+ region and the specific contact resistance between laser-doped region and aluminum contact as a function of energy density of the laser pulse. Both sheet resistance and contact resistance increase significantly with increasing

energy density beyond $4.1\,\mathrm{J/cm^2}$. Using a laser energy density below $4.1\,\mathrm{J/cm^2}$, we obtain a sheet resistance of $\varrho_{\mathrm{LDop}} = (330 \pm 10)\,\Omega/\mathrm{sq}$ and a specific contact resistance of $\varrho_{\mathrm{Al\text{-}LDop}} < 0.5\,\mathrm{m\Omega cm^2}$, which is well suitable for contact formation on our test devices. It is noteworthy that the sheet resistance of the laser-doped Al-p^+ regions can be significantly reduced if a SiN_x capping layer is deposited on top of the $\mathrm{Al_2O_3}$ prior to the laser process [116].

7.2 Lateral current transport in the hole inversion layer

We investigate charge transport in the p^+ inversion layer using electrical current-voltage measurements. All samples are fabricated on $1.5 - 1.6\,\Omega\mathrm{cm}$ Czochralski n-type c-Si wafers with a thickness of $300\,\mathrm{\mu m}$ and a sample size of $2.5 \times 2.5\,\mathrm{cm^2}$. A $20\,\mathrm{nm}$ thick $\mathrm{Al_2O_3}$ layer is deposited on the front side of the RCA-cleaned samples by plasma-assisted ALD. After deposition the samples were annealed for 15 min at $425\,^\circ\mathrm{C}$ in a nitrogen ambient. Figure 7.2 shows a sketch of the fabricated test structure, which allows transmission line measurements (*TLM*) of the inversion channel (A) and of laser-doped Al-p^+ regions (C), as well as mobility measurements (B) in a metal-oxide-silicon field-effect transistor (*MOSFET*) geometry, all on the same sample. This guarantees that the sample preparation is identical for different types of measurement.

7.2.1 IL sheet resistance in the dark

For the TLM structure (A) in Fig. 7.2 the laser-doped Al-p^+ regions have a width of $800\,\mathrm{\mu m}$, compared to an aluminum finger width of $480\,\mathrm{\mu m}$, to allow for slight misalignments between sample and shadow mask during aluminum evaporation. Accordingly, during an $I - V$ measurement between two contacts with a spacing d, the current has to pass two Al/Al-
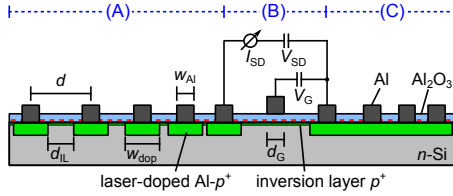
Figure 7.2: Sketch of the sample structure used for electrical measurements (not to scale). (A) and (C) are TLM structures used to characterize (A) the p^+ inversion layer and (C) the laser-doped Al-p^+ region. (B) forms a metal-oxide-semiconductor field effect transistor (*MOSFET*) for measurements of the inversion layer hole mobility.

p^+ contacts with a contact resistance $R_{\text{Al-LDop}}$ each, a total of $320\,\mu\text{m}$ through the laser-doped Al-p^+ regions with a sheet resistance of ϱ_{LDop}, two Al-p^+/IL contacts with a contact resistance $R_{\text{LDop-IL}}$, and the inversion layer itself over a distance of $d_{\text{IL}} = d - 800\,\mu\text{m}$. Accordingly, the total resistance R_Σ between two contacts is given by

$$R_\Sigma \;=\; 2R_{\text{c}} + \frac{d_{\text{IL}}}{l}\varrho_{\text{IL}} \;=\; 2R_{\text{Al-LDop}} + \frac{320\,\mu\text{m}}{l}\varrho_{\text{LDop}} + 2R_{\text{LDop-IL}} + \frac{d_{\text{IL}}}{l}\varrho_{\text{IL}}, \tag{7.1}$$

where R_{c} is the total contact resistance between Al and the inversion layer, ϱ_{IL} is the sheet resistance of the inversion layer, and $l = 2\,\text{cm}$ is the length of the Al contacts. Equation 7.1 assumes that parasitic currents through the *n*-type silicon base are negligible. On a test sample without Al_2O_3 deposition we measure currents $I < 10\,\mu\text{A}$ for voltages up to $10\,\text{V}$, corroborating that parasitic currents through the *n*-type substrate are several orders of magnitude smaller than the current flow through the inversion layer. The contact resistance R_{c} in Eq. 7.1 is independent of the contact spacing d. Hence, the inversion layer sheet resistance ϱ_{IL} is obtained from the slope of a linear fit to the measured resistance values R_Σ as a function of d_{IL}. Figure 7.3(a) shows the current I flowing between two contacts as a function of applied voltage V in the dark for four different pairs of contacts corresponding to $d_{\text{IL}} = 300,\,400,$

500, and 600 μm. Directly after the laser-doping process we observe only small currents with non-ohmic *I-V* characteristics and without distinct dependence on contact spacing [open symbols in Fig. 7.3(a)]. No such effect was observed for sheet resistance measurements on laser-doped Al-p^+ regions, which suggests a poor contact between the laser-doped Al-p^+ region and the inversion layer, presumably due to laser damage to the peripheral Al_2O_3 passivation layer surrounding the laser spots. This contact can be improved by a short annealing step at 400 °C for 1 min in ambient atmosphere, as shown by the solid symbols in Fig. 7.3(a). The corresponding *I-V* characteristics show an ohmic behavior. The solid lines in Fig. 7.3(a) are linear fits to the data. The corresponding total resistance values R_Σ are shown in the inset as a function of d_{IL}. Using Eq. 7.1 we obtain a sheet resistance of the p^+ inversion layer of $\varrho_{IL} = (15 - 18)\,k\Omega/sq$ for an Al_2O_3 thickness of 20 nm and a negative fixed charge density of $Q_f = -4 \times 10^{12}\,cm^{-2}$, in good agreement with results published by others authors [117] for a slightly higher fixed charge density. We obtain similar results for different sample preparations, e.g. if the Al_2O_3 is removed after laser-doping and subsequently another Al_2O_3 layer is deposited, showing that the post-laser annealing indeed fully recovers the laser damage.

Figure 7.3(b) shows the IL sheet resistance ϱ_{IL} for 10 nm of Al_2O_3 as a function of surface charge density $Q_\Sigma = Q_f + Q_c$, which has been varied by depositing corona charges onto the Al_2O_3 layer. Thus, the IL sheet resistance ϱ_{IL} can be significantly reduced from 15 kΩ/sq for $Q_\Sigma = Q_f = -3.8 \times 10^{12}\,cm^{-2}$, comparable to the value for 20 nm of Al_2O_3, down to 6 kΩ/sq for $Q_\Sigma = -2 \times 10^{13}\,cm^{-2}$.

The transmission line method allows an investigation of the fixed charge density in ultra-thin AlO_x layers below 1 nm, which is extremely challenging using capacitance-voltage or corona charge techniques, as the films are typically no longer perfectly insulating. Although the TLM analysis is in principle possible for any desired thickness of the dielectric film, it should be kept in mind that ultra-thin AlO_x layers might be
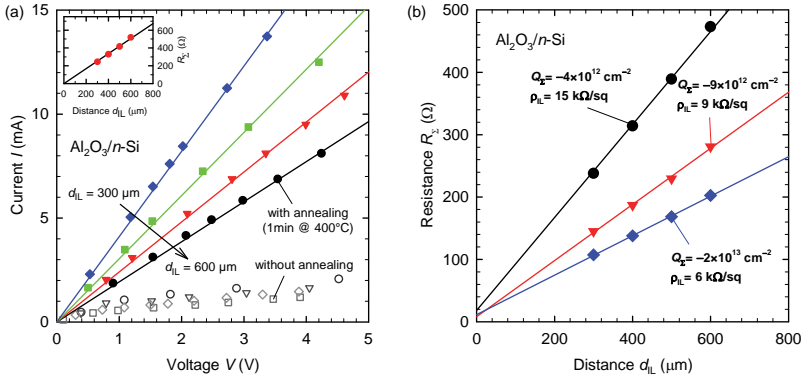
Figure 7.3: (a) Inversion channel current-voltage characteristics in the dark over a length of $d_{IL} = 300, 400, 500,$ and $600\,\mu m$, respectively, after annealing for 1 min at $400\,^{\circ}C$ (solid symbols). The corresponding total resistance values R_{Σ} are shown in the inset as a function of d_{IL}. Solid lines are linear fits to the data. No good contact is achieved directly after laser-doping without additional annealing (open symbols). (b) Total resistance R_{Σ} as a function of d_{IL} for different total surface charge densities Q_{Σ} achieved by the deposition of corona charges. Lines are linear fits to the data.

altered, e.g. by further oxidation, between deposition and measurement. Figure 7.4 shows the IL sheet resistance obtained by TLM as a function of annealing time at 425 °C for ultra-thin AlO_x layers deposited with 2, 4, 6, and 8 ALD cycles, corresponding to nominal thickness values of 0.24 nm, 0.48 nm, 0.73 nm, and 0.97 nm, respectively. The nominal thickness is calculated from the number of ALD cycles and the growth per cycle of 0.121 nm/cycle determined for thicker layers [see Fig. 2.4(b)], and might be inaccurate for such thin layers. Although the obtainable sheet resistances are generally higher than in the case of the 20 nm reference sample, a pronounced p^+ inversion layer is formed already with 4 monolayers of AlO_x. This effect might provide a convenient alternative to the laser-doping process to contact an Al_2O_3-induced inversion layer by means of a thin AlO_x tunneling layer. Such ultra-thin AlO_x tunneling layers have recently been used for contact passivation in highly efficient silicon solar cells [118].
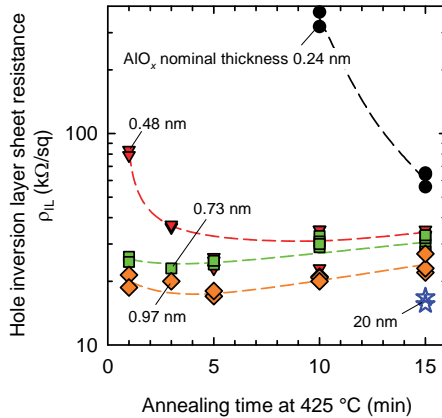

Figure 7.4: Hole inversion layer sheet resistance as a function of annealing time at 425 °C for ultra-thin AlO_x layers deposited by plasma-assisted ALD with a nominal thickness of 0.24 nm (2 ALD cycles), 0.48 nm (4 cycles), 0.73 nm (6 cycles), and 0.97 nm (8 cycles), respectively. The values for 20 nm of Al_2O_3 are given as a reference. The dashed lines are guides to the eye.

133

7.2.2 IL sheet resistance under illumination

The inversion layer sheet resistance is a critical parameter for the application of an Al_2O_3-induced inversion layer as emitter in an n-type inversion layer solar cell. Assuming that lateral current flow of photo-generated minority carriers is confined to the (two-dimensional) emitter with a constant sheet resistance ϱ_{sh}, the resistive power loss in the emitter can be analytically integrated [119], yielding a series resistance contribution of

$$R_s = \frac{\varrho_{IL}(p - w_{cont})^3}{12p},$$ (7.2)

where p and w_{cont} are the pitch and the width of the contacts, respectively. Accordingly, a pitch of $p = 1\,\mathrm{mm}$ and a sheet resistance of $\varrho_{IL} = 16\,\mathrm{k\Omega/sq}$ for an Al_2O_3-induced inversion layer result in a series resistance contribution exceeding $10\,\Omega\mathrm{cm}^2$ for a contact width below $90\,\mathrm{\mu m}$, severely limiting the solar cell efficiency. However, in an operating photovoltaic device, the inversion layer is illuminated and sheet resistance values determined in the dark might not be applicable. We use a halogen lamp to illuminate a $300\,\mathrm{\mu m}$ thick $1.6\,\Omega\mathrm{cm}$ n-type silicon TLM sample coated with $10\,\mathrm{nm}$ of Al_2O_3 at the front, and unpassivated at the rear. A calibrated photo-diode placed besides the sample is used to measure the illumination intensity.

Under illumination the *I-V* characteristics of the sample are no longer ohmic; we measure an excess current compared to the dark, which increases with applied voltage for small voltages below a few $100\,\mathrm{mV}$, depending on contact separation, and saturates for larger voltages. For typical solar cells, where the design of the emitter contacts allows a lateral voltage drop across the emitter smaller than $100\,\mathrm{mV}$, the former mechanism can be expected to dominate the resistive behavior of the IL emitter. The IL sheet resistance under illumination cannot be properly defined due to the non-linear dependence of resistance R vs. distance d_{IL}. Figure 7.5 shows the effective resistance $R = dV/dI$, determined over a voltage range of $V \approx 10 - 50\,\mathrm{mV}$ and for a contact length of $l = 2\,\mathrm{cm}$, as a function of the distance d_{IL} along the inversion layer for

illumination intensities of 0, 7, 22, and $86\,\text{mW/cm}^2$. The contact resistance of $2R_\text{c} = 3.4\,\Omega$, determined in the dark, has been subtracted from the experimental data. We observe a significant decrease of the effective resistance R with increasing illumination intensity, especially for a large contact separation.
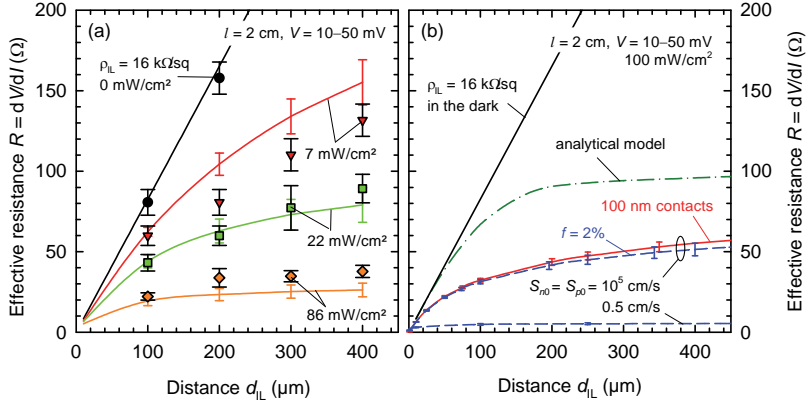

Figure 7.5: (a) Effective resistance R under illumination for small applied voltages $V \approx 10 - 50\,\text{mV}$, determined experimentally (symbols) and from device simulations (lines), as a function of d_IL for a $300\,\mu\text{m}$ thick $1.6\,\Omega\text{cm}$ n-Si wafer coated with $10\,\text{nm}$ Al_2O_3 on the front and unpassivated at the rear. The corresponding illumination intensities are given in the graph. (b) Simulated effective resistance for one sun illumination ($100\,\text{mW/cm}^2$) for line contacts with a metalization fraction of $f = 2\,\%$ (blue dashed line) or with a width of $100\,\text{nm}$ (red solid line). Two different rear side passivation schemes of $S_{n0} = S_{p0} = 10^5\,\text{cm/s}$ and $0.5\,\text{cm/s}$, respectively, are applied. An analytical prediction according to Kuhlmann [120] is given by the dash-dotted green line, the resistance in the dark is given by the black line as a reference.

We employ two-dimensional device simulations using SENTAURUS DEVICE [121], where the inversion layer is represented by a fixed charge density of $Q_\text{f} = -4 \times 10^{12}\,\text{cm}^{-2}$ and a hole mobility of $\mu_p = 100\,\frac{\text{cm}^2}{\text{Vs}}$ (see Table 3), and the contact geometries are chosen according to Fig. 7.2(A). The photogeneration current density for the planar samples is assumed to be $30\,\text{mA/cm}^2$, which was estimated from a comparison of transient

and quasi-static photoconductance measurements of Al_2O_3-passivated lifetime samples using a SINTON INSTRUMENTS WCT 120 lifetime tester. The unpassivated rear side with $S_{n0} = S_{p0} = 10^5$ cm/s is a worst-case scenario for solar cells with an unpassivated rear side, and the illumination intensities of 7, 22, and 86 mW/cm^2 then corresponds to excess carrier densities at the edge of the space charge region of $\Delta p = 2.5 \times 10^{13}$ cm^{-3}, 7.3×10^{13} cm^{-3}, and 2.9×10^{14} cm^{-3}, respectively. The simulations agree well with the experimental results, as shown by the solid lines in Fig. 7.5(a). According to our simulations, the lateral hole current density within the IL is largest near the contacts and decreases towards the center between two contacts, indicating that two-dimensional current flow due to a coupling of the IL to the n-type base is responsible for the increased lateral conductivity.

A real highly efficient solar cell device is more realistically described by a passivated rear side, better light trapping properties, and smaller contact area than the fairly wide Al-p^+ contact regions of the planar TLM test structures. Furthermore, the sheet resistance of illuminated inversion layers has been described analytically by Kuhlmann [120], who assumed two parallel conductive channels of inversion layer and base, both with a constant sheet resistance, connected by a p/n diode and a photo-generated current source. Figure 7.5(b) shows the calculated effective resistance for one sun illumination (100 mW/cm^2, with a photogeneration current density of 44 mA/cm^2 assuming Lambertian light trapping) according to Kuhlmann's model (dash-dotted green line), assuming an ideality factor of $n = 1$, and our Sentaurus device simulations for line contacts with a metalization fraction of $f = 2\%$ (blue dashed line) and negligibly small line contacts with a constant width of 100 nm (black solid line, $f < 0.1\%$ for a practical contact separation with $d_{IL} > 100\,\mu$m in a solar cell). Two different rear side passivation schemes of $S_{n0} = S_{p0} = 10^5$ cm/s and 0.5 cm/s, respectively, are applied, which correspond to excess carrier densities of $\Delta p = 6 \times 10^{14}$ cm^{-3} and 1×10^{16} cm^{-3}, respectively. The effective resistance under illumination decreases with increasing metallization fraction, indicating that the contact regions couple to the n-type

base as well. However, even for the smallest contacts we observe a significant reduction of the effective resistance under illumination, compared to the dark. It is noteworthy that Kuhlmann's model does not account for the non-linear *I-V* characteristics and overestimated the IL resistance under illumination, even if a fairly large photogenerated current density of $44\,\text{mA/cm}^2$ is assumed.

The IL sheet resistance under illumination cannot be properly defined due to the non-linear dependence of resistance R vs. distance d_{IL}. However, an effective sheet resistance $\varrho_{\text{sh.eff}}$ can be defined by the ratio of effective normalized resistance $R \times l$ over distance d_{IL}. In the case of an unpassivated rear side, and for typical operating conditions of solar cells, i.e. one sun illumination and a small metallization fraction of $f = 2\,\%$, we obtain $\varrho_{\text{sh.eff}} = 3600\,\Omega/\text{sq}$ for a contact separation of $250\,\mu\text{m}$, which drops to $1300\,\Omega/\text{sq}$ for a contact separation of $1\,\text{mm}$. Furthermore, in the case of a passivated rear side ($S_{n0} = S_{p0} = 0.5\,\text{cm/s}$), the effective sheet resistance drops significantly to values of $\varrho_{\text{sh.eff}} = 420\,\Omega/\text{sq}$ and $120\,\Omega/\text{sq}$ for contact separations of $250\,\mu\text{m}$ and $1\,\text{mm}$, respectively, due to the increased excess carrier density. As a consequence, the requirement for small contact separation for highly resistive IL emitters is less strict than suggested by the simple calculations according to Eq. 7.2, where one-dimensional current flow through the IL and a dark sheet resistance of $16\,\text{k}\Omega/\text{sq}$ is assumed.

7.2.3 IL hole mobility

The inversion layer induced by the negative fixed charges at the *n*-Si/Al$_2$O$_3$ interface typically has a depth of a few hundred nanometers. Due to this confinement of charge carriers near the surface one may expect a pronounced degradation of transport properties due to surface scattering. The electron concentration in the inversion channel is many orders of magnitude lower than the hole concentration. Accordingly, the contribution of electron transport to the total inversion channel conduc-

tivity is negligible, and the electric current can solely be attributed to the drift of free holes.

Under strong inversion conditions, the source–drain current of a metal/oxide/semi-conductor field-effect transistor (*MOSFET*) is given by [25, pp. 438-442]

$$I_{SD} = \frac{V_{SD}}{R_p} + \begin{cases} \frac{1}{2}\beta(2V_{eff} - V_{SD})V_{SD} & \text{if } V_{SD} \leq V_{eff} \\ \frac{1}{2}\beta V_{eff}^2 & \text{if } V_{SD} \geq V_{eff} \end{cases}, \qquad (7.3)$$

where R_p is an ohmic resistance accounting for parasitic currents, V_{SD} is the voltage applied between source and drain, and $V_{eff} = V_G - V_T$ is the effective gate voltage relative to the threshold voltage V_T. The factor β is related to the hole mobility μ_p by [25, pp. 438-442]

$$\beta = \frac{l}{d_G}\mu_p C_{ox}, \qquad (7.4)$$

where l is the length of the Al contacts, d_G is the width of the gate contact shown in Fig. 7.2(B), and C_{ox} is the capacitance of the Al_2O_3 gate insulator per unit area.

The gate contact on our samples does not overlap with the laser-doped Al-p^+ regions around source and drain [see Fig. 7.2(B)], which have a rough surface texture due to the laser processing, as this might provoke shunts through the gate oxide. As a consequence, we observe a significant voltage drop over the highly-resistive parts of the inversion layer which are not modulated by the voltage applied to the gate contact. However, as the sheet resistance of the inversion layer is known, a corrected source-drain voltage V_{SD}^* across the gated region of width d_G can easily be calculated, which yields

$$V_{SD}^* = V_{SD} - \left[2R_c + \frac{d_{IL} - d_G}{l}\varrho_{IL}\right]I_{SD}, \qquad (7.5)$$

where R_c is the contact resistance between Al and inversion layer. It should be kept in mind, however, that the effective gate voltage V_{eff} is

affected as well. Therefore, V_{eff} is not constant for all the data measured for a fixed applied gate voltage V_G and, accordingly, Eq. 7.3 only strictly applies around the saturation region, where the voltage drop over the inversion layer is independent of applied voltage.
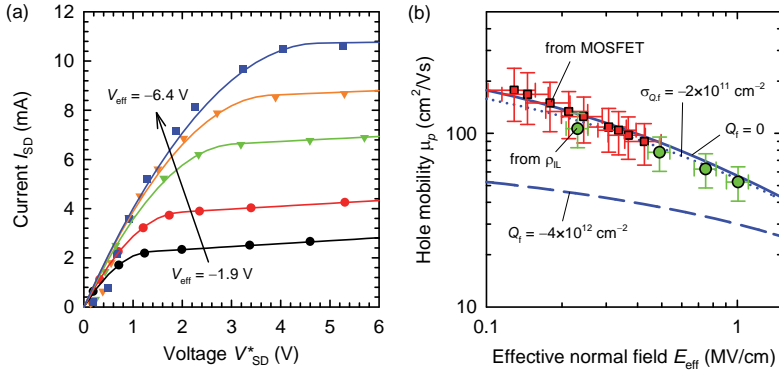

Figure 7.6: (a) Source-drain current I_{SD} of an $Al/Al_2O_3/n$-Si field effect transistor as a function of corrected voltage V_{SD}^* across the gated inversion channel for different effective gate voltages V_{eff}. Solid lines are fits of Eq. 7.3 to the data. (b) IL hole mobility μ_p as a function of transverse effective field E_{eff}, obtained from MOSFET measurements (red squares) and calculated from the sheet resistance for various surface charge densities deposited by corona charging (green circles). Blue lines are calculated according to a parameterization by Agostinelli [122] assuming fixed charge densities of 0 (solid line), $-2 \times 10^{11}\,cm^{-2}$ (dotted line), and $-4 \times 10^{12}\,cm^{-2}$ (dashed line).

Figure 7.6(a) shows the measured source-drain current I_{SD} of the Al/ Al_2O_3/n-Si field effect transistor as a function of corrected voltage V_{SD}^* across the gated inversion channel for different effective gate voltages V_{eff}, the solid lines are fits of Eq. 7.3 to the data. The current I_{SD} increases linearly with increasing V_{SD}^* in the saturation regime for high voltages $V_{SD}^* > V_{eff}$, which justifies the inclusion of an ohmic parasitic resistance R_p in Eq. 7.3. We attribute this parasitic resistance to current flow around the gated region, as the gate contact length is only 20 mm, compared to the sample size of 25 mm. From the dependence of the saturation current

$I_{\text{SD.sat}}$ on the applied gate voltage V_G we deduce a threshold voltage of $V_T = V_G - V_{\text{eff}} = (0.9 \pm 0.2)\,\text{V}$, which corresponds to a fixed charge density of $Q_f = -(4.0 \pm 0.4) \times 10^{12}\,\text{cm}^{-2}$ underneath the metal gate contact. This is in good agreement with values of $Q_f = -(4 \pm 1) \times 10^{12}\,\text{cm}^{-2}$ for comparable Al_2O_3 layers without metal deposition, as shown in Fig. 5.1.

For the c-Si/SiO_2 interface it has previously been shown [123] that the electron and hole inversion layer mobilities as a function of effective transverse field follow a universal curve over a wide range of effective fields if the transverse effective field E_{eff} is defined as

$$E_{\text{eff}} = \frac{1}{\varepsilon_{\text{Si}}} \left(Q_{\text{Depl}} + \eta Q_{\text{IL}} \right), \qquad (7.6)$$

where ε_{Si} is the silicon dielectric constant, Q_{Depl} is the depleted bulk charge density, Q_{IL} is the inversion layer charge density, $\eta = 1/3$ for holes, and $\eta = 1/2$ for electrons. We determine the charge densities Q_{Depl} and Q_{IL} for a given gate voltage V_G by means of numerical simulations based on the iterative numerical model described in Sec. 3.1.3, where we employ Fermi-Dirac statistics based on the analytical approximation of the Fermi integral given by Eq. 3.7. Figure 7.6(b) shows hole mobility values, which are obtained from the fits in Fig. 7.6(a) using Eq. 7.4, as a function of effective transverse field E_{eff} (red squares). In addition, the hole mobility is calculated from measured sheet resistance values and simulated hole concentration profiles for various surface charge densities deposited by corona charging [green circles in Fig. 7.6(b)]. The blue lines are calculations based on an empirical parameterization of the IL hole mobility for the c-Si/SiO_2 interface proposed by Agostinelli et al. [122]. This parameterization accounts for bulk and surface phonon scattering, screened Coulomb scattering, and scattering due to surface roughness. The different curves in Fig. 7.6(b) correspond to fixed charge densities of $Q_f = 0$ (solid line), $-2 \times 10^{11}\,\text{cm}^{-2}$ (dotted line), and $-4 \times 10^{12}\,\text{cm}^{-2}$ (dashed line), respectively. The chemical and electrical properties of the c-Si/Al_2O_3 interface are dominated by a thin interfacial layer of SiO_x (compare Sec. 4.2 and Ref. 4, 18). Hence, it is a reasonable assump-

tion that the parameterization of the IL hole mobility at the c-Si/SiO$_2$ interface may also be valid for the c-Si/Al$_2$O$_3$ interface.

Our mobility data, however, clearly exceed the predicted values corresponding to $Q_f = -4 \times 10^{12}$ cm^{-2}, and a good agreement is only found for much smaller fixed charge densities $|Q_f|$. In Sec. 3.3.2 it has been shown that the spatial surface potential fluctuations at the c-Si/Al$_2$O$_3$ interface are smaller than 60 meV. Assuming a random charge distribution at the c-Si/Al$_2$O$_3$ interface this corresponds to a standard deviation of the fixed charge density of $\sigma_{Q.f} < 2 \times 10^{11}$ cm^{-2}, for which the mobility data agrees reasonably well with the predictions. This implies that the mean distance between neighboring negative fixed charges at the c-Si/Al$_2$O$_3$ interface is much smaller than a Debye length, and, accordingly, the fixed charges at the c-Si/Al$_2$O$_3$ interface form an extended two-dimensional charge density rather than acting as individual isolated point charges. Accordingly, the fixed charges do not act as individual scattering centers, and the number of surface scattering centers is small due to the homogeneous distribution of fixed charges. Hence, the inversion layer hole mobility is not significantly reduced by scattering caused by the high negative fixed charge density at the c-Si/Al$_2$O$_3$ interface.

7.3 Efficiency potential of IL solar cells on *n*-type Si

7.3.1 Surface passivation of IL emitters

Al$_2$O$_3$-induced inversion layer emitters are promising candidates for emitters in highly efficient *n*-type silicon solar cells due to the low surface recombination as well as low bulk recombination within the emitter, as defects introduced by the dopant diffusion are avoided. We use the method proposed by Kane and Swanson [125] to extract the emitter saturation current density J_{0e} of an Al$_2$O$_3$-induced IL p^+ emitter from the quasi-
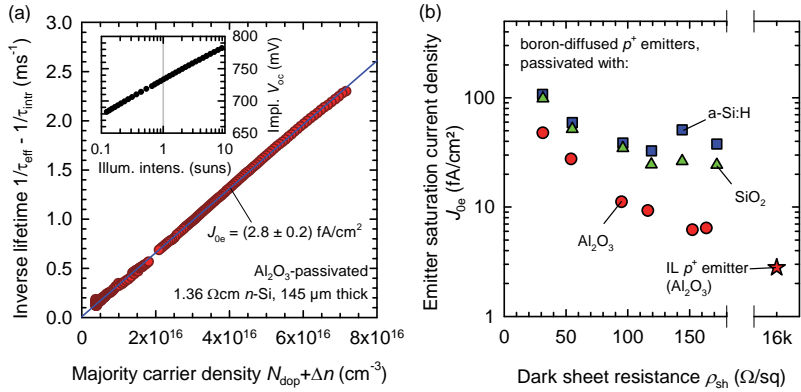
Figure 7.7: (a) Inverse effective lifetime corrected for intrinsic recombination $(1/\tau_{\mathrm{eff}} - 1/\tau_{\mathrm{intr}})$ as a function of majority carrier density $(N_{\mathrm{dop}} + \Delta n)$ for an Al_2O_3-passivated $145\,\mu$m thick $1.36\,\Omega$cm n-Si wafer. The intrinsic carrier concentration is assumed to be $n_{\mathrm{i}} = 8.6 \times 10^9\,\mathrm{cm}^{-3}$. The inset shows the implied open-circuit voltage $V_{\mathrm{oc.impl}}$ as a function of illumination intensity. The one-sun V_{oc} is 733 mV. (b) Emitter saturation current density $J_{0\mathrm{e}}$ of the IL emitter in graph (a), compared to literature data of boron-diffused p^+ emitters passivated with different layers (Ref. 6, 124) for various emitter sheet resistances ϱ_{sh}.

steady-state effective lifetime of Al_2O_3-passivated lifetime samples. We use a quarter of a $1.35\,\Omega$cm n-Si wafer with a diameter of 6 inch, which has been etched in an aqueous KOH solution to a thickness of $145\,\mu$m in order to remove any surface damage and reduce the impact of bulk recombination on the effective lifetime. Figure 7.7(a) shows the inverse effective lifetime $1/\tau_{\mathrm{eff}}$, corrected for intrinsic (radiative and Auger) recombination using our parameterization according to Eq. 6.12, as a function of majority carrier density in the bulk ($N_{\mathrm{dop}} + \Delta n$). A linear fit to the data yields a value of $J_{0\mathrm{e}}/n_i^2 = (3.8 \pm 0.1) \times 10^{-35}\,\mathrm{Acm}^4$. Assuming an intrinsic carrier concentration of $n_i = 8.6 \times 10^9\,\mathrm{cm}^{-3}$, this corresponds to an emitter saturation current density of $J_{0\mathrm{e}} = (2.8 \pm 0.1)\,\mathrm{fA/cm}^2$. Figure 7.7(b) shows the emitter saturation current density $J_{0\mathrm{e}}$ of the IL emitter compared to literature data of boron-diffused emitters [6, 124] with various sheet resistances ϱ_{sh}, passivated with amorphous hydrogenated silicon (*a-Si:H*), thermally grown SiO_2, and Al_2O_3, respectively. The lowest value of $J_{0\mathrm{e}}$ is obtained for our IL emitter.

The inset in Fig. 7.7(a) shows the implied open-circuit voltage $V_{\mathrm{oc.impl}}$, extracted from the same lifetime measurements using the so-called Suns–V_{oc} method described by Sinton et al. [126], as a function of the illumination intensity. At an illumination intensity of one sun we measure an implied open-circuit voltage of $V_{\mathrm{oc.impl}} = 733\,\mathrm{mV}$ on the investigated sample.

7.3.2 Sentaurus Device simulations

We investigate the ultimate efficiency potential of IL solar cells on n-Si in more detail by means of two-dimensional device simulations using Sentaurus Device based on experimentally determined input parameters.

The wafer temperature is set at $25\,^{\circ}$C in our simulations. We implement intrinsic recombination in the bulk silicon according to the approximation given in Eq. 6.15 and 6.16, which are based on the improved parameterization of Auger recombination presented in Chapter 6. For the IL emitter we assume a fixed charge density of $Q_{\mathrm{f}} = -4 \times 10^{12}\,\mathrm{cm}^{-2}$ [see

Fig. 5.1(b)] and a hole mobility of $\mu_p = 100 \frac{\text{cm}^2}{\text{Vs}}$ [see Fig. 7.6(b)]. For the Al_2O_3-passivated surfaces we use the surface recombination velocity parameters derived in Sec. 5.3.3, i.e. $S_{n0} = 5200\,\text{cm/s}$ and $S_{p0} = 1300\,\text{cm/s}$ for the Al_2O_3-passivated IL, and $S_{n0} = S_{p0} = 0.5\,\text{cm/s}$ and $Q_\text{f} = 0$ for the n-type base. The effect of "parasitic shunting" [79], and hence the impact of the actual density and polarity of the fixed charges, is considered to be negligible due to the heavy doping underneath the contacts. Accordingly, the results of the simulations can be applied both to all-Al_2O_3-passivated solar cells and to solar cells where the n-type base is well passivated by other means, e.g. by thermally grown SiO_2 or SiN_x deposited by plasma-enhanced chemical vapor deposition (*PECVD*).

The base and emitter contacts are modeled as locally highly-doped n^+ and p^+ regions, respectively, with a sheet resistance of $30\,\Omega/\text{sq}$. The width of the contacts is adjusted to yield a metalization fraction of $f = 2\,\%$, independent of the contact spacing. The effective SRV on unpassivated highly phosphorus- or boron-doped silicon surfaces has previously been determined to be around $S_\text{eff} = 2 \times 10^5\,\text{cm/s}$ on bare silicon and up to $S_\text{eff} = 3 \times 10^6\,\text{cm/s}$ at metallized surfaces [127–129]. We use SRV parameters of $S_{n0} = S_{p0} = 10^5\,\text{cm/s}$ for the metallized contacts, which could reasonably be obtained by a moderate contact passivation, which yields emitter saturation current densities of $J_\text{0e} = (330 - 340)\,\text{fA/cm}^2$ for the n^+ and p^+ regions used in the simulations.
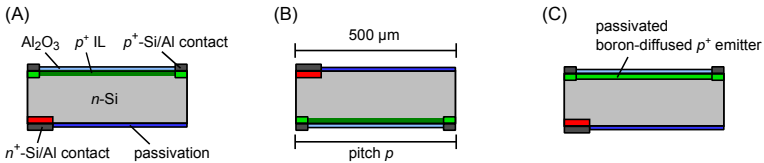

Figure 7.8: Sketch of the three different emitter designs (not to scale) investigated in our Sentaurus simulations: (A) front IL emitter, (B) rear IL emitter, and (C) boron-diffused selective emitter.

We compare three different emitter configurations in our simulations, as shown in Fig. 7.8: (A) An IL hole emitter on the front side, (B) an IL hole

emitter on the rear side, and (C), as a reference, a $160\,\Omega/\text{sq}$ boron-diffused selective p^+ emitter on the front side. For the boron emitter, passivated with Al_2O_3, we use $S_{n0} = S_{p0} = 5\,\text{cm/s}$ in order to reproduce the minimum emitter saturation current density of $J_{0e} = 7\,\text{fA/cm}^2$ measured in Ref. [6] for this emitter. The silicon wafer is $4.6\,\Omega\text{cm}$ n-Si, corresponding to a doping density of $N_{\text{dop}} = 10^{15}\,\text{cm}^{-3}$. We vary the pitch p of the emitter contacts ($p = 250\,\mu\text{m}$, $500\,\mu\text{m}$, or $1\,\text{mm}$), while the base contact pitch is kept constant at $1\,\text{mm}$. Series resistance contributions from the metallization are neglected in these simulations. For the photogeneration we assume perfect Lambertian light trapping and an optical shading of $2\,\%$, matching the front metallization fraction. This results in a maximum photogenerated current density of $42.8\,\text{mA/cm}^2$ for a solar cell with a thickness of $160\,\mu\text{m}$. The input parameters used in our simulations are summarized in Table 3 in the appendix.

Figures 7.9(a)–(d) show the solar cell parameters (open-circuit voltage V_{oc}, short-circuit current density J_{sc}, fill factor FF, and efficiency η) for $p = 500\,\mu\text{m}$ as a function of wafer thickness W for a front or rear IL hole emitter (red squares) and a $160\,\Omega/\text{sq}$ boron-diffused p^+ emitter (green diamonds). The open blue circles represent the V_{oc} limit for Al_2O_3-induced IL emitter solar cells, where all recombination currents associated with the contact regions have been neglected, as described below. Both the front and rear IL emitters yield virtually identical results [accordingly, only one set of data is shown in Fig. 7.9(a)–(d)] and outperform the conventional boron-diffused emitter over a wide range of wafer thicknesses. The IL emitters yield a maximum V_{oc} of $735\,\text{mV}$ for a wafer thickness of $20\,\mu\text{m}$, compared to a maximum V_{oc} of $731\,\text{mV}$ for the boron emitter. The maximum solar cell efficiencies η are obtained for a wafer thickness around $160-320\,\mu\text{m}$, mainly due to a reduced short-circuit current density J_{sc} and fill factor FF for thinner wafers, and reduced V_{oc} and fill factor FF for thicker wafers. For the IL emitter solar cells with $p = 500\,\mu\text{m}$ this corresponds to a maximum efficiency of $\eta_{\text{max}} = 26.2\,\%$ including contact recombination, and $\eta_{\text{max}} = 27.8\,\%$ if all contact recombination and optical shading is neglected. Figure 7.10 shows the calculated recom-
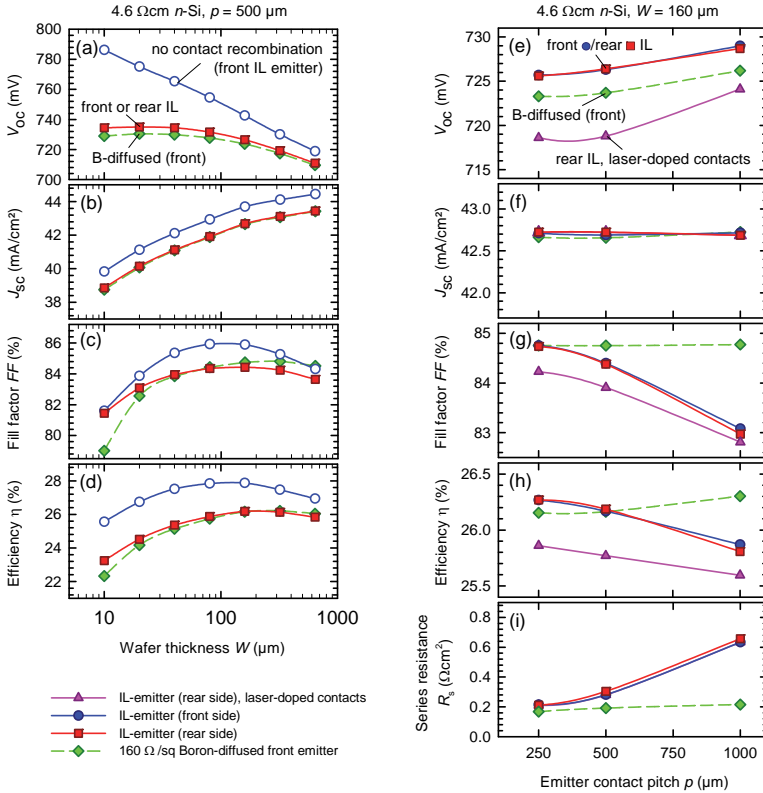
Figure 7.9: Simulated solar cell parameters under one sun illumination (open-circuit voltage V_{oc}, short-circuit current density J_{sc}, fill factor FF, efficiency η, and series resistance R_s) as a function of wafer thickness W (a)–(d) and emitter contact pitch p (e)–(i) for $4.6\,\Omega\mathrm{cm}$ n-type solar cells with a $160\,\Omega/\mathrm{sq}$ boron-diffused p^+ emitter at the front (green diamonds), an $\mathrm{Al_2O_3}$-induced IL hole emitter at the front (blue circles) or rear (red squares) with highly boron-doped contact regions, and a rear IL hole emitter with local Al-p^+ contact regions formed by laser-doping (pink triangles). The open blue circles in (a)–(d) show the performance limit for $\mathrm{Al_2O_3}$-induced IL emitter solar cells, where all recombination currents associated with the contact regions have been neglected. The emitter metalization fraction is $f = 2\%$ (solid symbols) or $f = 0\%$ (open symbols). Lines are guides to the eye.

146

bination current density in different parts of the solar cell as a function of cell voltage for a rear IL emitter solar cell with a thickness of $160\,\mu\text{m}$ and $p = 500\,\mu\text{m}$. The same qualitative behavior is found for front IL emitter solar cells. Below the maximum power point ($V_{\text{mpp}} = 642\,\text{mV}$ in Fig. 7.10) recombination is clearly dominated by recombination at the contacts at the front of the solar cell, i.e. the n-type base contacts in the case of the rear IL emitter solar cell and the p-type emitter contacts in the case of the front IL emitter solar cell. For larger voltages recombination currents in the bulk and both the base and emitter contacts become comparable. It is noteworthy that the recombination current over the full voltage range is dominated by bulk and contact recombination, and not by surface recombination at the Al_2O_3-passivated surfaces. We calculate the ultimate efficiency potential of Al_2O_3-based IL solar cells, which is only limited by bulk recombination and surface recombination at the undiffused surfaces, by subtracting recombination currents related to the n^+ and p^+ contacts from simulated illuminated current-voltage characteristics, and neglecting any optical shading losses. For the device shown in Fig. 7.10 this increases the open-circuit voltage limit from $V_{\text{oc}} = 726\,\text{mV}$ to $743\,\text{mV}$, and increases the efficiency potential from $\eta = 26.2\,\%$ to $27.8\,\%$. The open-circuit limit obtained in this way for a front IL emitter with $p = 500\,\mu\text{m}$ is shown in Fig. 7.9(a) as a function of wafer thickness W by the open blue circles.

Figures 7.9(e)–(i) show the solar cell parameters V_{oc}, J_{sc}, η, and *FF*, as well as the series resistance R_{s}, for a wafer thickness of $160\,\mu\text{m}$ as a function of emitter contact pitch p for a front IL emitter (blue circles), rear IL emitter (red squares), and $160\,\Omega/\text{sq}$ boron emitter (green diamonds) including all recombination channels. We obtain the highest efficiency of $\eta = 26.3\,\%$ for a front or rear IL emitter for a contact pitch of $p = 250\,\mu\text{m}$. Both front and rear IL emitters yield virtually identical results. Differences in efficiency between front and rear IL emitters only start to play a role for $p = 1\,\text{mm}$, but remain below $0.1\,\%_{\text{abs.}}$ absolute in our simulations. Compared to the IL emitters, the boron-diffused front emitter suffers from a slightly reduced V_{oc} ($\Delta V_{\text{oc}} = 2 - 3\,\text{mV}$), but yields
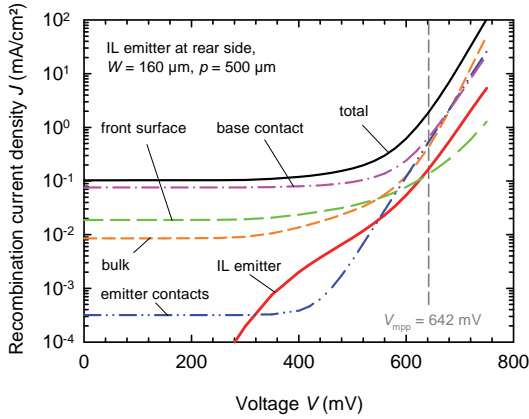
Figure 7.10: Recombination current density J as a function of cell voltage V for a rear IL hole emitter solar cell on n-type silicon with a thickness of $160\,\mu m$ and an emitter contact pitch of $p = 500\,\mu m$. Different lines correspond to recombination in different parts of the solar cell. Contact recombination includes recombination at the Si/metal interface and in the locally-doped contact regions.

a comparable maximum efficiency of $\eta = 26.3\,\%$ for a contact pitch of $p = 1\,\text{mm}$. With increasing contact pitch p the fill factor, and hence the efficiency, drops significantly for the solar cells with IL emitter, while cell performance improves slightly for the boron-diffused emitter. This drop in efficiency for the IL emitter solar cells can be attributed to the high sheet resistance of the IL emitter. Although the effective resistance of the IL emitter decreases significantly [see Fig. 7.5(b)] under illumination, it remains more than one order of magnitude larger than the sheet resistance of $160\,\Omega/\text{sq}$ of the boron emitter for all investigated cell geometries. Figure 7.9(i) shows the series resistance R_s at the maximum power point, determined from Sentaurus simulations for two different illumination intensities employing the double-light-level method [130]. Indeed, the series resistance of the simulated rear IL emitter solar cell – without any series resistance contributions from the metallization – increases from $0.21\,\Omega\text{cm}^2$ for $p = 250\,\mu m$ to $0.30\,\Omega\text{cm}^2$ for $p = 500\,\mu m$ and $0.64\,\Omega\text{cm}^2$

for $p = 1\,\text{mm}$, while the series resistance of the boron-diffused front emitter solar cell only increases slightly from $0.17\,\Omega\text{cm}^2$ for $p = 250\,\mu\text{m}$ to $0.22\,\Omega\text{cm}^2$ for $p = 1\,\text{mm}$, as shown in Fig. 7.9(i). Note that the series resistance R_s shows a pronounced dependence on the voltage in our case, leading to relatively high fill factors despite a non-negligible series resistance. Hence, excellent solar cell efficiencies can still be obtained for a pitch of the order of $1\,\text{mm}$ despite the high nominal sheet resistance of the inversion layer in the dark.[†]

In order to explore the potential of completely avoiding any boron diffusions in the fabrication of n-type solar cells, Fig. 7.9(e)–(i) includes simulation results for a rear IL emitter (pink triangles), where the highly boron-doped p^+-regions underneath the contacts have been replaced by laser-doped Al-p^+ regions. The saturation current density of the Al-p^+ is $J_{0\text{e}} = 1130\,\text{fA/cm}^2$, which results from the choice of $S_{n0} = S_{p0} = 10^5\,\text{cm/s}$ and a doping profile from Ref. [116] for an $\text{Al}_2\text{O}_3/\text{SiN}_x$ stack with $10\,\text{nm}$ of Al_2O_3. The increased contact recombination results in a reduced open-circuit voltage V_oc and a lower fill factor *FF*, which leads to an efficiency loss of $(0.2 - 0.4)\,\%_\text{abs.}$ absolute compared to highly boron-diffused contact regions. It is noteworthy, however, that the laser-doped Al-p^+ regions do not significantly reduce the excellent short-circuit current density of $J_\text{sc} = 42.7\,\text{mA/cm}^2$, which in conclusion enables excellent efficiencies up to $\eta = 25.9\,\%$.

[†]Please note that the benefit of an inversion layer, as opposed to a well-passivated surface without induced junction, depends on the quality and resistivity of the bulk material, as the current in the solar cell flows along different paths in both scenarios. While this benefit is negligible for defect-free, lowly doped float-zone Si (bulk resistivity $> 5\,\Omega\text{cm}$), the presence of a hole conducting p^+ inversion layer becomes crucial for n-type solar cells on highly doped or defect-rich Si.

7.4 Experimental realization of IL hole emitter solar cells on *n*-type silicon
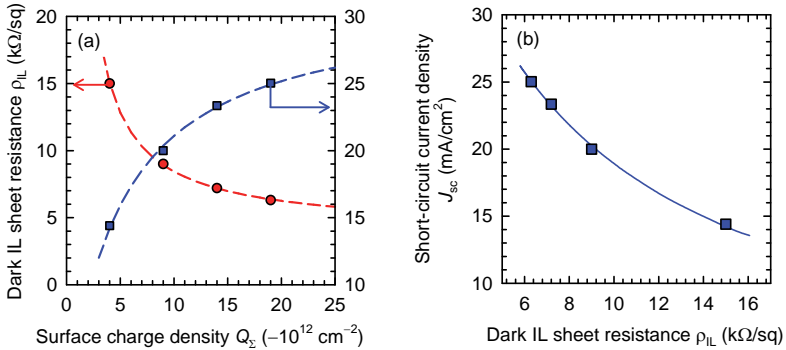
7.4.1 Surface charge dependence of current collection

Figure 7.11: (a) Short-circuit current density J_{sc} (blue squares, right axis) and IL sheet resistance ϱ_{IL} in the dark (red circles, left axis) as a function of total surface charge density $Q_\Sigma = Q_f + Q_c$, which has been varied by corona charging. The lines are guides to the eye. (b) Corresponding dependence of $J_{sc}(\varrho_{IL})$ calculated from the data shown in (a).

For an IL at the front side of the solar cell the dependence of the short-circuit current density on the sheet resistance of the inversion layer is handily analyzed by depositing corona charges onto the solar cell. Al front contacts with a finger spacing of 280 µm are directly evaporated using a Ni shadow mask onto a textured 1 Ωcm *n*-type Cz-Si wafer, which is contacted at the rear by local phosphorus-diffused n^+ regions and full-area Al evaporation. A sketch of the sample geometry is shown in Fig. 7.12(A). Please note that, while it is simple to fabricate, this contact design is not well suited for a solar cell, as it relies on the small lateral overlap of Al contact and IL of around a few tens of nanometers. Figure 7.11(a) shows the measured short-circuit current density J_{sc} (blue squares, right axis) under standard testing conditions (AM1.5G spectrum,

$100\,\text{mW/cm}^2$, $25\,^\circ\text{C}$) as a function of the total surface charge density $Q_\Sigma = Q_\text{f} + Q_\text{c}$, which has been varied by depositing corona charges onto the Al_2O_3 layer at the front of the solar cell. The IL sheet resistance ϱ_IL in the dark according to Fig. 7.3(b) is shown as red circles (left axis) as a reference. The lines are guides to the eye. Figure 7.11(b) shows the corresponding dependence of the short-circuit current density J_sc on the IL sheet resistance ϱ_IL in the dark. The pronounced dependence of J_sc on Q_Σ, and accordingly on ϱ_IL, is strong evidence that the inversion layer is indeed acting as charge collecting emitter in the solar cell.

7.4.2 Rear emitter IL solar cells on *n*-type Si

The measured short-circuit current density in Fig. 7.11 experimentally demonstrates that the p^+ inversion layer on n-Si can indeed be utilized as charge collecting emitter in an n-type inversion layer solar cell. However, the simple front contacts according to Fig. 7.12(A) are unsuitable for an efficient solar cell device, and would need to be replaced by a rather complex contact design. Recently, this cell concept was also investigated by Erickson et al. [131], who improved the front contact to the inversion layer by implementing a conductive transparent polymer layer, which allowed efficiencies of up to $8.4\,\%$. However, our numerical simulations predict the same efficiency potential for front and rear IL emitters, which favors an IL emitter on the rear side due to a significantly simplified fabrication of the emitter contacts, which do not require the introduction of a polymer film [131] or complex alignment procedures when using a laser-based process.

We hence introduce an inversion layer solar cell on n-type Si with a rear-side emitter contacted by laser-doping and full-area metal evaporation. Alternatively, the rear contacts to the inversion layer emitter could also be formed by laser contact openings (*LCO*) and conventional screen-printing of an aluminum paste, creating local Al-p^+ back surface regions. In both cases the contacts to the inversion layer can be fabricated by simple
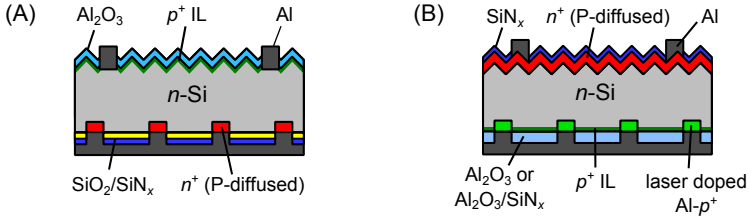
Figure 7.12: (A) Sketch of a front IL emitter test device with non-optimized contacts to the IL emitter. (B) Sketch of the rear contacted n-type inversion layer solar cell processed as proof-of-principle device, where contacts to the inversion layer emitter at the rear side are formed by an Al_2O_3 laser-doping process.

laser processes, and do not require any alignment or are restricted by shading considerations. A sketch of the rear IL emitter solar cell design is shown in Fig. 7.12(B). We fabricate a proof-of-principle device with an active area of $2 \times 2\,cm^2$ on $160\,\mu m$ thick $5\,\Omega cm$ phosphorus-doped n-type Cz-Si. The front side of the solar cell features a random-pyramid-textured, homogeneously phosphorus-diffused front surface region with a nominal sheet resistance of $100\,\Omega/sq$. The rear side is passivated either with a single Al_2O_3 layer or an Al_2O_3/SiN_x stack, which induces a p^+ IL rear emitter in the n-Si base. Line contacts to the rear IL emitter with a width of $16\,\mu m$ and a pitch of $250\,\mu m$ and $500\,\mu m$ are formed by laser-doping, as described in Sec. 7.1, using a laser energy density of $4.0\,J/cm^2$. Contacts on the front and rear are formed by electron gun evaporation of aluminum, using a Ni shadow mask for the front side. We have applied thin tunneling layers, formed by depositing 2 ALD cycles of AlO_x, underneath the front contacts, and – on a subset of samples – underneath the rear contacts. After evaporation of the Al contacts the front side is passivated with a SiN_x passivation/anti-reflection double layer deposited by plasma-enhanced chemical vapor deposition (*PECVD*) at a deposition temperature of $300\,°C$.

Reference cells have been processed on $160\,\mu m$ thick $5\,\Omega cm$ boron-doped p-type Cz-Si using exactly the same process sequence.
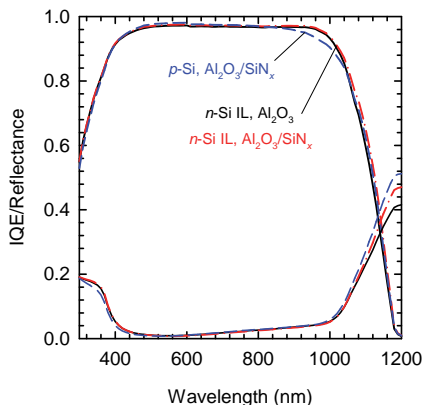
Figure 7.13: Internal quantum efficiency (*IQE*) and reflectance of the best *n*-type IL solar cells with a single Al_2O_3 layer (solid black line) and an Al_2O_3/SiN_x stack (dash-dotted red line) as rear surface passivation, as well as a *p*-type reference cell passivated with an Al_2O_3/SiN_x stack (dashed blue line).

Figure 7.13 shows the internal quantum efficiency (*IQE*) and reflectance of the best *n*-type IL emitter solar cells with a single Al_2O_3 layer (solid black line) and an Al_2O_3/SiN_x stack (dash-dotted red line) as rear surface passivation, compared to the best *p*-type reference cell (blue dashed line) passivated with an Al_2O_3/SiN_x stack. The best IL solar cells have a rear contact pitch of $p = 250\,\mu m$, corresponding to a rear metallization fraction of $f = 6.4\,\%$, while the *p*-type reference cell has an optimal pitch of $p = 500\,\mu m$, corresponding to $f = 3.2\,\%$. The IL solar cells clearly show an improved current generation in the long wavelength range above $\lambda = 800\,nm$ (gain in current $\Delta J_{sc} = +0.43\,mA/cm^2$ for the Al_2O_3/SiN_x stack), while current generation below $\lambda = 800\,nm$ is slightly lower than for the *p*-type reference cell ($\Delta J_{sc} = -0.07\,mA/cm^2$ for the Al_2O_3/SiN_x stack). Despite the larger metallization fraction, and accordingly lower optical quality of the dielectric back reflector, this results in a gain in photocurrent of $+0.36\,mA/cm^2$ for the IL solar cells compared to the *p*-type reference cell. It should be kept in mind, however, that these

differences are smaller than typical uncertainties in the measurement and analysis of the illuminated $I - V$ characteristics.

Device	RS passivation	V_{oc} (mV)	J_{sc} (mA/cm^2)	FF (%)	η (%)
IL n-Si,	Al$_2$O$_3$	634*	39.7*	72.0*	18.1*
IL n-Si,	Al$_2$O$_3$/SiN$_x$	622	40.2	71.7	17.9
p-Si,	Al$_2$O$_3$	639	39.7	77.1	19.5
p-Si,	Al$_2$O$_3$/SiN$_x$	651	39.9	76.1	19.8
IL Simulation n-Si		663	40.2	76.2	20.3

Table 7.1: Measured solar cell parameters for the best rear IL solar cells on n-Si and reference cells on p-Si, as well as simulated solar cell parameters for the n-type IL solar cells.
* independently confirmed at Fraunhofer ISE CalLab.

The solar cell parameters measured under standard testing conditions (AM1.5G spectrum, $100\,\text{mW/cm}^2$, 25 °C) of the best n-type IL and p-type reference solar cells, as well as the results of the numerical simulation, are summarized in Table 7.1. For the best IL solar cell we achieve an independently confirmed short-circuit current density of $J_{sc} = 39.7\,\text{mA/cm}^2$, an open-circuit voltage of $V_{oc} = 634\,\text{mV}$, and a fill factor of $FF = 72.0\,\%$, resulting in a cell efficiency of $\eta = 18.1\,\%$. The relatively low fill factor of $FF = 72.0\,\%$ and pseudo fill factor of $pFF = 80.3\,\%$ of this cell show that the proof-of-principle devices are largely technologically limited by a high series resistance and a low shunt resistance.

We have adapted the numerical simulations presented in Sec. 7.3 to represent the fabricated n-type IL solar cells. We have adapted the contact geometry to account for the limited resolution of the laser system, added a full-area $100\,\Omega/\text{sq}$ phosphorus-doped front surface field between and underneath the base contacts, and included an assumed series resistance contribution of the front and rear metallization of $R_{s.\text{front}} = R_{s.\text{rear}} = 0.5\,\Omega\text{cm}^2$. The results of the simulation are shown in Table 7.1 as well. Compared to the numerical simulation the open-circuit voltage V_{oc} of

the experimental n- and p-type solar cells is reduced by approximately $10 - 40\,$mV. Recombination in the simulated solar cell is dominated by recombination in the full-area phosphorus-diffused front surface field, where we have assumed SRV parameters of $S_{n0} = S_{p0} = 10\,$cm/s. Accordingly, the low V_{oc} can most likely be attributed to the low-temperature SiN$_x$ deposition, which results in a reduced surface passivation quality. The main reason for the low temperature of the SiN$_x$ deposition was to prevent diffusion of Al into the solar cell. The fabricated solar cells were found to be stable – and in fact even improve – after several minutes at $400\,°$C. Hence, the solar cell concept presented here might improve significantly in a future experiment if the deposition temperature of the SiN$_x$ is raised to $400\,°$C.

Despite these technological limitations in our n-type IL cells, the achieved efficiency of $\eta = 18.1\,\%$ is to our knowledge the highest efficiency reported to date for IL emitter solar cells on n-type Si.

8 Summary

In the present thesis, we have investigated the application of atomic layer deposition (ALD) of amorphous Al_2O_3 dielectric layers to silicon solar cells. Fundamental studies on the chemical and electrical properties of the c-Si/Al_2O_3 interface were conducted, and the intrinsic recombination in silicon was re-evaluated based on the excellent level of surface passivation provided by ALD-Al_2O_3. Furthermore, a novel Al_2O_3-based inversion layer solar cell on n-type silicon was introduced and first proof-of-principle devices were presented.

The key issue in applying Al_2O_3 passivation layers to silicon solar cells on an industrial scale is the low deposition rate of approximately $2\,\mathrm{nm/min}$ in conventional (sequential) ALD reactors. In this thesis, the passivation quality of Al_2O_3 layers deposited by a novel spatial ALD process, which allows a wafer throughput compatible with industry demands, was investigated for the first time. We have demonstrated a maximum effective surface recombination velocity of $S_{\mathrm{max}} = 1.1 - 2.9\,\mathrm{cm/s}$ at an excess carrier density of $\Delta n = 10^{15}\,\mathrm{cm^{-3}}$ for $10\,\mathrm{nm}$ of Al_2O_3 on $4\,\Omega\mathrm{cm}$ n-type Czochralski-grown Si wafers with a size of $15.6 \times 15.6\,\mathrm{cm^2}$, which is comparable to values of $S_{\mathrm{max}} = 0.9 - 2.2\,\mathrm{cm/s}$ achieved by conventional plasma-assisted ALD. The Al_2O_3 layers deposited by spatial ALD do not degrade significantly after a typical contact firing process in a belt furnace, after which we still obtained $S_{\mathrm{max}} < 20\,\mathrm{cm/s}$. The excellent firing stability of the Al_2O_3 layers and the weak injection dependence of the effective lifetime, which promises an excellent solar cell performance also under weak-light conditions, make the studied Al_2O_3 layers deposited by high-throughput spatial ALD well suited for future generations of industrial high-efficiency silicon solar cells.

For sequential ALD reactors, the low deposition rate is mitigated by reducing the thickness of the deposited layer. We have investigated the

physical mechanisms responsible for the excellent level of surface passivation provided by Al_2O_3 deposited by ALD as a function of the thickness of the deposited Al_2O_3 layers. A high density of negative fixed charges and a moderate interface state density had previously been reported for ALD-Al_2O_3. Indeed, for an Al_2O_3 thickness above 5 nm (plasma-assisted ALD) or 10 nm (thermal ALD) we have identified both field-effect passivation due to a high negative fixed charge density of $Q_f = -(4 \pm 1) \times 10^{12}$ cm^{-2} and chemical passivation due to a low interface state density at midgap of $D_{it.midgap} = (1 - 3) \times 10^{11}$ eV^{-1}cm^{-2}. We have demonstrated that the negative charges responsible for the strong field-effect passivation are located within 1 nm of the Si/Al_2O_3 interface, which is an important result also for the application of thin tunneling layers to passivate the metal contacts of a solar cell. The interface state density, on the other hand, was shown to increase significantly for ultra-thin Al_2O_3 films below $5 - 10$ nm, depending on deposition technique, and no significant level of chemical passivation was observed for films thinner than 3 nm. However, due to the high fixed charge density responsible for the excellent level of field-effect passivation, low effective surface recombination velocities of $S_{eff} < 100$ cm/s at $\Delta n = 10^{15}$ cm^{-3} were measured on 1.5 Ωcm p-type FZ-Si samples passivated by Al_2O_3 films of only 1 nm thickness.

In the present thesis, a comprehensive model of the c-Si/Al_2O_3 interface was developed for the first time, which describes the chemical composition of the deposited film and the recombination at the c-Si/Al_2O_3 interface. We have identified a high concentration of excess oxygen and, as a consequence, a significant deviation from stoichiometry in the Al_2O_3 films near the interface. Furthermore, no aluminum was detected after the first cycle, presumably due to an incomplete reaction of the trimethyl-aluminum (*TMA*) precursor molecules during the first few cycles of the ALD process, where the functional groups at the silicon surface are not optimal for an adsorption of the TMA precursor molecules. The resulting island growth of the deposited film explains very well the degradation of the interface state density for ultra-thin Al_2O_3 films. We have proposed that the high oxygen-to-aluminum atomic ratio near the interface is a likely candidate

for the origin of the high negative fixed charge density. The fixed charge density was demonstrated for the first time to be tunable by applying an external bias voltage and to be partly unstable under annealing, in good agreement with the proposed model that oxygen-related defects in the Al_2O_3 near the interface are responsible for the high negative fixed charge density.

The electrical properties of the c-Si/Al_2O_3 interface were shown to be largely dominated by a thin interfacial layer of SiO_x in combination with a transition region between SiO_x and Al_2O_3, which extends over a depth of several nanometers. As a consequence, the effective relative dielectric permittivity decreases from $\varepsilon_r = 8.1 \pm 0.2$ for bulk-like Al_2O_3 to $\varepsilon_r = 4.3 \pm 0.3$ for AlO_x layers with a thickness of $1\,nm$.

We have presented a detailed analysis of recombination at Al_2O_3-passivated p- and n-type Si surfaces. Capture cross sections of $\sigma_p = (4 \pm 3) \times 10^{-16}\,cm^2$ for holes and $\sigma_n = (7 \pm 4) \times 10^{-15}\,cm^2$ for electrons were measured near midgap. The capture cross section ratio at midgap was found to be highly asymmetric with $\sigma_n/\sigma_p = 5 - 70$. The capture cross sections were found to be similar to values reported for the silicon/SiO_2 interface, suggesting a strong influence of the interfacial SiO_x layer on the chemical passivation properties. We have identified three distinct defect peaks and their respective recombination parameters. A fourth type of defect was considered negligible concerning interface recombination due to its very low capture cross section below $10^{-19}\,cm^2$ near the valence band edge. A combination of the three dominant defect types was shown to describe the energy dependence of the measured capture cross sections very well and accounts for the different interface state distributions observed for plasma-assisted, thermal, and spatial ALD, respectively. The presented defect model is also consistent with experimental results where we have identified a degradation of the interface quality upon applying an external bias voltage of several volts.

Based on our defect model we have compared calculated and measured injection-level-dependent effective surface recombination velocities at dif-

ferent surface charge densities. The numerical simulations showed an excellent agreement with the experimental data for both *n*- and *p*-type Si and for a wide range of excess carrier densities and surface charge densities. For small surface charge densities close to zero the surface recombination velocity showed a strong dependence on excess carrier density. For large surface charge densities of $|Q_\Sigma| > 10^{12}\,\mathrm{cm}^{-2}$, which are typical for annealed Al_2O_3 layers on Si, interface recombination was shown to be effectively suppressed and virtually independent of excess carrier density for both *n*- and *p*-type Si.

The excellent surface passivation quality provided by ALD-Al_2O_3 allowed us to investigate intrinsic bulk recombination in crystalline silicon with greatly improved accuracy. Particularly, effective lifetimes exceeding the previously established parameterization of intrinsic lifetimes in silicon were measured. Based on these lifetime measurements, an improved parameterization of the intrinsic lifetime of *n*- and *p*-type crystalline silicon at 300 K was derived, which accounts for Coulomb-enhanced Auger recombination as well as Coulomb-enhanced radiative recombination.

On *n*-type silicon, the negative fixed charges at the c-Si/Al_2O_3 interface induce a hole inversion layer (IL) close to the surface. In this thesis, we have applied such an Al_2O_3-induced IL for the first time as hole-collecting emitter in IL solar cells made on *n*-type silicon. Importantly, the field-dependent IL hole mobility near the silicon surface was shown to be comparable to values previously measured at the c-Si/SiO_2 interface. Due to the highly homogeneous deposition method, the high density of fixed charges in the Al_2O_3 layers only leads to a minor increase in the surface scattering rate, and the detrimental impact on the mobility expected for high charge densities is in fact negligible. The IL layer hole mobility for an Al_2O_3 passivation layer without externally applied electric field is $\mu_p = (110 \pm 30)\,\frac{\mathrm{cm}^2}{\mathrm{Vs}}$.

We have measured a sheet resistance of the Al_2O_3-induced inversion layer on *n*-type Si of $15 - 18\,\mathrm{k\Omega/sq}$ in the dark for 20 nm of Al_2O_3. For ultra-thin AlO_x layers below 1 nm thickness the sheet resistance of the

inversion layer was shown to increase with decreasing layer thickness. However, a sheet resistance below $35\,\mathrm{k\Omega/sq}$ in the dark was still achieved for layers thinner than $0.5\,\mathrm{nm}$. A key result of our experiments is that under illumination or carrier injection, the current flow is no longer confined to the inversion layer, resulting in a significantly reduced effective resistance for small lateral voltages. Under typical solar cell operating conditions, the effective sheet resistance is below $4\,\mathrm{k\Omega/sq}$ and is hence well suited for the implementation as emitter in n-type silicon IL solar cells.

A novel, easily fabricable rear-emitter inversion layer solar cell concept on n-type silicon was introduced based on the high density of negative fixed charges in an Al_2O_3 surface passivation layer. A $4\,\mathrm{cm}^2$ proof-of-principle device reached an independently confirmed short-circuit current density of $J_{sc} = 39.7\,\mathrm{mA/cm}^2$, an open-circuit voltage of $V_{oc} = 634\,\mathrm{mV}$, and a fill-factor of $FF = 72.0\,\%$, resulting in a solar cell efficiency of $\eta = 18.1\,\%$. The major limitations were shown to be due to technological problems in our current process sequence and are not of fundamental nature. The efficiency potential of the n-type silicon IL solar cells was investigated by two-dimensional Sentaurus device simulations. The simulations showed that for small contact pitches up to $500\,\mathrm{\mu m}$ the IL solar cells outperform high-efficiency solar cells based on a selective boron-diffused emitter and allow efficiencies up to $26.3\,\%$ and open-circuit voltages up to $735\,\mathrm{mV}$, including contact recombination. Recombination in these IL solar cells was shown to be dominated by recombination at the locally-doped base and emitter contacts. Neglecting optical shading and recombination losses at the contacts increased the efficiency limit further to $\eta_{max} = 27.8\,\%$ and the open-circuit voltage limit to above $780\,\mathrm{mV}$.

Appendix

Details of the wafers prepared for the reassessment of intrinsic recombination in silicon

Sample No.	type	ϱ_{bulk} (Ωcm)	N_{dop} (cm^{-3})	W (μm)	Passivation layer	$\tau_{\text{eff.max}}$ (ms)	S_{max} cm/s	Measurement method
1	n-FZ	95	4.7×10^{13}	203	Al$_2$O$_3$ [a]	22	0.5	QSSPL
2	n-FZ	97	4.6×10^{13}	203	Al$_2$O$_3$ [a]	32	0.3	SSPL
3	n-FZ	10.3	4.4×10^{14}	204	Al$_2$O$_3$ [a]	27	0.4	SSPL
4	n-FZ	1.56	3.1×10^{15}	239	Al$_2$O$_3$ [b]	9.3	1.3	PCD
5	n-FZ	0.96	5.2×10^{15}	203	Al$_2$O$_3$ [a]	4.3	2.4	QSSPL
6	n-FZ	1.00	4.9×10^{15}	181	Al$_2$O$_3$ [a]	6.8	1.3	SSPL
7	n-FZ	1.00	4.9×10^{15}	200	SiN$_x$ [c]	6.3	1.6	QSSPL
8	n-CZ	0.41	1.3×10^{16}	197	SiN$_x$ [c]	1.2	8.6	PCD
9	p-FZ	100	1.3×10^{14}	254	Al$_2$O$_3$ [a]	33	0.4	QSSPL
10	p-FZ	105	1.3×10^{14}	253	Al$_2$O$_3$ [a]	40	0.3	SSPL
11	p-FZ	9.7	1.4×10^{15}	256	Al$_2$O$_3$ [a]	13	1.0	QSSPL
12	p-FZ	9.8	1.4×10^{15}	253	Al$_2$O$_3$ [a]	19	0.7	SSPL
13	p-FZ	1.34	1.1×10^{16}	303	Al$_2$O$_3$ [b]	3.7	4.1	QSSPL PCD
14	p-FZ	1.26	1.2×10^{16}	300	Al$_2$O$_3$ [b]	6.8	2.2	PCD
15	p-FZ	1.00	1.5×10^{16}	250	Al$_2$O$_3$ [a]	3.1	4.0	QSSPL
16	p-FZ	1.05	1.4×10^{16}	250	Al$_2$O$_3$ [a]	3.9	3.2	PCD
17	p-FZ	0.49	3.3×10^{16}	297	Al$_2$O$_3$ [b]	0.95	15.6	PCD
18	p-FZ	0.47	3.4×10^{16}	251	Al$_2$O$_3$ [a]	0.87	14.5	QSSPL
19	p-FZ	0.16	1.3×10^{17}	259	Al$_2$O$_3$ [b]	0.088	147	PCD
20	p-FZ	0.10	2.5×10^{17}	255	Al$_2$O$_3$ [a]	0.037	346	QSSPC

Table 1: Sample number, wafer type, bulk resistivity ϱ_{bulk}, dopant concentration N_{dop}, wafer thickness W, type of passivation layer, maximum measured lifetime $\tau_{\text{eff.max}}$ and corresponding maximum SRV S_{max}, as well as measurement method for selected samples processed for the reassessment of Auger recombination in silicon.
Deposition by (a) PA-ALD in OPAL reactor, (b) PA-ALD in FLEXAL reactor, and (c) PECVD.

Sample No.:	1	2	3	5	6
$J_0/(\mathrm{nA/cm^2})$	46	23	30	76	20
m	4.0	3.8	3.8	4.0	3.8

Table 2: Fit parameters for the SCR recombination on n-Si according to Eq. 6.11.

Input parameters used in Sentaurus Device simulations

Parameter	Value	Reference
Width of simulation domain:	500 µm	
Wafer temperature:	25 °C	
Photogeneration:	Lambertian light trapping	
Base substrate doping:	4.6 Ωcm n-Si, $N_\mathrm{dop} = 10^{15}\,\mathrm{cm^{-3}}$	
Bulk recombination:	intrinsic + $\tau_{n0} = \tau_{p0} = 50\,\mathrm{ms}$	
Metallization fraction:	2 %, line contacts	
Mesh in the inversion layer:	1 nm per mesh point	
Hole Mobility in the IL:	$100\,\frac{\mathrm{cm^2}}{\mathrm{Vs}}$	this work
Fixed charges Q_f Al$_2$O$_3$:	$-4 \times 10^{12}\,\mathrm{cm^{-2}}$	this work

	S_{n0}	S_{p0}	
Doped contact regions:	$10^5\,\mathrm{cm/s}$	$10^5\,\mathrm{cm/s}$	adapted from [127–129]
Al$_2$O$_3$ with band bending:	$5200\,\mathrm{cm/s}$	$1300\,\mathrm{cm/s}$	this work
Surface passivation of base: (no band bending)	$0.5\,\mathrm{cm/s}$	$0.5\,\mathrm{cm/s}$	this work
Boron emitter:	$5\,\mathrm{cm/s}$	$5\,\mathrm{cm/s}$	$J_{0e} = 7\,\mathrm{fA/cm^2}$ from [6]

	Peak concentration	Junction Depth [@$10^{15}\,\mathrm{cm^{-3}}$]	
$30\,\Omega/\mathrm{sq}$ P-n^+ under contact	$8.8 \times 10^{19}\,\mathrm{cm^{-3}}$	$1.05\,\mathrm{µm}$	Gaussian
$31\,\Omega/\mathrm{sq}$ B-p^+ under contact	$3.3 \times 10^{19}\,\mathrm{cm^{-3}}$	$2.10\,\mathrm{µm}$	[6]
$163\,\Omega/\mathrm{sq}$ B-p^+ emitter	$7.8 \times 10^{18}\,\mathrm{cm^{-3}}$	$1.32\,\mathrm{µm}$	[6]
$280\,\Omega/\mathrm{sq}$ laser-doped Al-p^+	$4.0 \times 10^{20}\,\mathrm{cm^{-3}}$	$0.80\,\mathrm{µm}$	[116]
$100\,\Omega/\mathrm{sq}$ P-n^+ contact/FSF	$4.2 \times 10^{19}\,\mathrm{cm^{-3}}$	$0.47\,\mathrm{µm}$	ECV data

Table 3: Input parameters for our Sentaurus Device simulations of inversion layer hole emitter solar cells on n-type Si.

Bibliography

[1] K. Jaeger and R. Hezel, A novel thin silicon solar cell with Al_2O_3 as surface passivation, *Proceedings ot the 18th IEEE Photovoltaic Specialists Conference*, 1752–1753 (1985).

[2] G. Agostinelli, A. Delabie, P. Vitanov, Z. Alexieva, H. F. W. Dekkers, S. D. Wolf, and G. Beaucarne, Very low surface recombination velocities on p-type silicon wafers passivated with a dielectric with fixed negative charge, *Solar Energy Materials & Solar Cells* **90**, 3438–3443 (2006).

[3] B. Hoex, S. B. S. Heil, E. Langereis, M. C. M. van de Sanden, and W. M. M. Kessels, Ultralow surface recombination of c-Si substrates passivated by plasma-assisted atomic layer deposited Al_2O_3, *Applied Physics Letters* **89**, 042112 (2006).

[4] B. Hoex, J. J. H. Gielis, M. C. M. van de Sanden, and W. M. M. Kessels, On the c-Si surface passivation mechanism by the negative-charge-dielectric Al_2O_3, *Journal of Applied Physics* **104**(11), 113703 (2008).

[5] B. Hoex, J. Schmidt, P. Pohl, M. C. M. van de Sanden, and W. M. M. Kessels, Silicon surface passivation by atomic layer deposited Al_2O_3, *Journal of Applied Physics* **104**(4), 044903 (2008).

[6] B. Hoex, J. Schmidt, R. Bock, P. P. Altermatt, M. C. M. van de Sanden, and W. M. M. Kessels, Excellent passivation of highly doped p-type Si surfaces by the negative-charge-dielectric Al_2O_3, *Applied Physics Letters* **91**(11), 112107 (2007).

[7] J. Schmidt, A. Merkle, R. Brendel, B. Hoex, M. C. M. van de Sanden, and W. M. M. Kessels, Surface passivation of high-efficiency silicon solar cells by atomic-layer-deposited Al_2O_3, *Progress in Photovoltaics: Research and Applications* **16**, 461–466 (2008).

[8] J. Benick, B. Hoex, M. C. M. van de Sanden, W. M. M. Kessels, O. Schultz, and S. W. Glunz, High efficiency n-type Si solar cells on Al_2O_3-passivated boron emitters, *Applied Physics Letters* **92**(25), 253504 (2008).

[9] J. Schmidt, B. Veith, and R. Brendel, Effective surface passivation of crystalline silicon using ultrathin Al_2O_3 films and Al_2O_3/SiN_x stacks, *Physica Status Solidi – Rapid Research Letters* **3**(9), 287–289 (2009).

[10] G. Dingemans, M. C. M. van de Sanden, and W. M. M. Kessels, Influence of the deposition temperature on the c-Si surface passivation by Al_2O_3 films synthesized by ALD and PECVD, *Electrochemical and Solid-State Letters* **13**(3), H76–H79 (2010).

[11] P. Saint-Cast, D. Kania, M. Hofmann, J. Benick, J. Rentsch, and R. Preu, Very low surface recombination velocity on p-type c-Si by high-rate plasma-deposited aluminum oxide, *Applied Physics Letters* **95**(15), 151502 (2009).

[12] T.-T. Li and A. Cuevas, Effective surface passivation of crystalline silicon by rf sputtered aluminum oxide, *Physica Status Solidi – Rapid Research Letters* **3**(5), 160–162 (2009).

[13] M. J. Kerr and A. Cuevas, General parameterization of Auger recombination in crystalline silicon, *Journal of Applied Physics* **91**(4), 2473–2480 (2002).

[14] T. Suntola and J. Antson. Method for producing compound thin films. US Patent No. 4058430, (1977).

[15] S. B. S. Heil, J. L. van Hemmen, M. C. M. van de Sanden, and W. M. M. Kessels, Reaction mechanisms during plasma-assisted atomic layer deposition of metal oxides: A case study for Al_2O_3, *Journal of Applied Physics* **103**(10), 103302 (2008).

[16] W. Kern and D. A. Puotinen, Cleaning solutions based on hydrogen peroxide for use in silicon semiconductor technology, *RCA Review* **31**, 187–206 (1970).

[17] G. Dingemans and W. M. M. Kessels, Status and prospects of Al_2O_3-based surface passivation schemes for silicon solar cells, *Journal of Vacuum Science and Technology A* **30**(4), 040802 (2012).

[18] G. Dingemans, N. M. Terlinden, D. Pierreux, H. B. Profijt, M. C. M. van de Sanden, and W. M. M. Kessels, Influence of the oxidant on the chemical and field-effect passivation of Si by ALD Al_2O_3, *Electrochemical and Solid-State Letters* **14**(1), H1–H4 (2011).

[19] P. Poodt, A. Lankhorst, F. Roozeboom, K. Spee, D. Maas, and A. Vermeer, High-speed spatial atomic-layer deposition of aluminum oxide layers for solar cell passivation, *Advanced Materials* **22**(32), 3564–3567 (2010).

[20] B. Veith, Oberflächenpassivierung von Silicium mit atomlagenabgeschiedenem Aluminiumoxid, Diploma thesis (in German), Leibniz Universität Hannover / Institute for Solar Energy Research Hamelin (ISFH) (2009).

[21] D. Zielke, Rückseitenpassivierung von kristallinen Siliciumsolarzellen mit Aluminiumoxid, Diploma thesis (in German), Leibniz Universität Hannover / Institute for Solar Energy Research Hamelin (ISFH) (2010).

[22] C. M. Herzinger, B. Johs, W. A. McGahan, J. A. Woollam, and W. Paulson, Ellipsometric determination of optical constants for silicon and thermally grown silicon dioxide via a multi-sample, multi-wavelength, multi-angle investigation, *Journal of Applied Physics* **83**(6), 3323 (1998).

[23] M. M. Mandoc, M. L. C. Adams, G. Dingemans, N. M. Terlinden, M. C. M. van de Sanden, and W. M. M. Kessels, Corona charging and optical second-harmonic generation studies of the field-effect passivation of c-Si by Al_2O_3 films, *Proceedings of the 35th IEEE Photovoltaic Specialists Conference*, 3200–3204 (2010).

[24] B. Veith, F. Werner, D. Zielke, R. Brendel, and J. Schmidt, Comparison of the thermal stability of single Al_2O_3 layers and Al_2O_3/SiN_x stacks for the surface passiviation of silicon, *Energy Procedia* **8**, 307 (2011).

[25] S. M. Sze, *Physics of Semiconductor Devices*, Wiley, New York, 2nd Edition (1981).

[26] D. H. Levy, S. F. Nelson, and D. Freeman, Oxide electronics by spatial atomic layer deposition, *Journal of Display Technology* **5**(12), 484–494 (2009).

[27] A. Vermeer, F. Roozeboom, P. Poodt, and R. Görtzen, High throughput, low cost deposition of alumina passivation layers by spatial atomic layer deposition, *MRS Proceedings*, volume 1323, C04–04 (2011).

[28] I. Cesar, E. Granneman, P. Vermont, E. Tois, P. Manshanden, L. J. Geerligs, E. E. Bende, A. R. Burgers, A. A. Mewe, Y. Komatsu, and A. W. Weeber, Excellent rear side passivation on multi-crystalline silicon solar cells with 20 nm uncapped Al_2O_3 layer: Industrialization of ALD for solar cell applications, *Proceedings of the 35th IEEE Photovoltaic Specialists Conference*, 44–49 (2010).

[29] Solaytec product brochure. www.solaytec.com, (2013).

[30] A. B. Sproul, Dimensionless solution of the equation describing the effect of surface recombination on carrier decay in semiconductors, *Journal of Applied Physics* **76**(5), 2851 (1994).

[31] K. Ramspeck, S. Reissenweber, J. Schmidt, K. Bothe, and R. Brendel, Dynamic carrier lifetime imaging of silicon wafers using an infrared-camera-based approach, *Applied Physics Letters* **93**, 102104 (2008).

[32] B. Veith, T. Ohrdes, F. Werner, R. Brendel, P. P. Altermatt, N.-P. Harder, and J. Schmidt, Injection dependence of the effective lifetime of *n*-type Si passivated by Al_2O_3: An edge effect?, *Solar Energy Materials & Solar Cells* **120**, 436–440 (2013).

[33] E. H. Nicollian and J. R. Brews, *MOS (Metal Oxide Semiconductor) Physics and Technology*, Wiley, New York (1982).

[34] W. B. Joyce and R. W. Dixon, Analytic approximations for the Fermi energy of an ideal Fermi gas, *Applied Physics Letters* **31**, 354–356 (1977).

[35] R. M. Corless, G. H. Gonnet, D. E. G. Hare, D. J. Jeffrey, and D. E. Knuth, On the Lambert W function, *Advances in Computational Mathematics* **5**, 329–359 (1996).

[36] R. Girisch, R. Mertens, and R. de Keersmaecker, Determination of the Si-SiO$_2$ interface recombination parameters using a gate-controlled point-junction diode under illumination, *IEEE Transactions on Electron Devices* **35**(2), 203 (1988).

[37] S. Steingrube, R. Brendel, and P. P. Altermatt, Limits to model amphoteric defect recombination via SRH statistics, *Physica Status Solidi A* **209**(2), 390–400 (2012).

[38] W. Shockley and W. T. Read, Statistics of the recombination of holes and electrons, *Physical Review* **87**(5), 835 (1952).

[39] C. N. Berglund, Surface states at steam-grown silicon - silicon dioxide interfaces, *IEEE Transactions on Electron Devices* **ED-13**(10), 701 (1966).

[40] R. Lindner, Semiconductor surface varactor, *The Bell System Technical Journal* **41**(3), 803–831 (1962).

[41] J. R. Brews, A simplified high-frequency MOS capacitance formula, *Solid State Electronics* **20**(7), 607–608 (1977).

[42] Keithley, *Model 595 Quasistatic CV Meter Instruction Manual.*

[43] E. Nicollian and A. Goetzberger, The Si-SiO$_2$ interface - Electrical properties as determined by the metal-insulator-silicon conductance technique, *The Bell System Technical Journal* **46**(6), 1055 (1967).

[44] J. W. Elam, D. Routkevitch, and S. M. George, Properties of ZnO / Al$_2$O$_3$ alloy films grown using atomic layer deposition techniques, *Journal of The Electrochemical Society* **150**(6), G339 (2003).

[45] S. Dauwe, J. Schmidt, A. Metz, and R. Hezel, Fixed charge density in silicon nitride films on crystalline silicon surfaces under illumination, *Proceedings of the 29th IEEE Photovoltaic Specialists Conference*, 162–165 (2002).

[46] L. Kelvin, Contact electricity of metals, *Philosophical Magazine* **46**, 82–120 (1898).

[47] Trek, Inc., *Operator's manual model 320C electrostatic voltmeter*, rev. a3 Edition.

[48] Y. J. Chabal, G. S. Higashi, K. Raghavachari, and V. A. Burrows, Infrared spectroscopy of Si(111) and Si(100) surfaces after HF treatment: Hydrogen termination and surface morphology, *Journal of Vacuum Science & Technology, A* **7**(3), 2104–2109 (1989).

[49] M. Seibt, Georg-August Universität Göttingen, *Personal communication.*

[50] S. Tanuma, C. J. Powell, and D. R. Penn, Calculations of electron inelastic mean free paths, *Surface and Interface Analysis* **17**, 927–939 (1991).

[51] S. Tanuma, C. J. Powell, and D. R. Penn, Calculations of electron inelastic mean free paths. IX. data for 41 elemental solids over the 50 eV to 30 keV range, *Surface and Interface Analysis* **43**, 689–713 (2011).

[52] S. H. Pandya, B. G. Vaishnav, and K. N. Joshipura, Electron inelastic mean free paths in solids: A theoretical approach, *Chinese Physics B* **21**(9), 093402 (2012).

[53] F. Reinert and S. Hüfner, Photoemission spectroscopy—from early days to recent applications, *New Journal of Physics* **7**(1), 97 (2005).

[54] C. D. Wagner, W. M. Riggs, L. E. Davis, and J. F. Moulder, *Handbook of x-ray photoelectron spectroscopy: a reference book of standard data for use in x-ray photoelectron spectroscopy*, Physical Electronics Division, Perkin-Elmer Corp. (1979).

[55] V. Naumann, M. Otto, R. B. Wehrspohn, and C. Hagendorf, Chemical and structural study of electrically passivating Al_2O_3/Si interfaces prepared by atomic layer deposition, *Journal of Vacuum Science & Technology A* **30**(4), 04D106 (2012).

[56] K. Y. Gao, F. Speck, K. Emtsev, T. Seyller, L. Ley, M. Oswald, and W. Hansch, Interface of atomic layer deposited Al_2O_3 on H-terminated silicon, *Physica Status Solidi A* **203**(9), 2194–2199 (2006).

[57] K. Y. Gao, F. Speck, K. Emtsev, T. Seyller, and L. Ley, Thermal stability of surface and interface structure of atomic layer deposited Al_2O_3 on H-terminated silicon, *Journal of Applied Physics* **102**, 094503 (2007).

[58] C. Krug, E. B. O. da Rosa, R. M. C. de Almeida, J. Morais, I. J. R. Baumvol, T. D. M. Salgado, and F. C. Stedile, Atomic transport and chemical stability during annealing of ultrathin Al_2O_3 films on Si, *Physical Review Letters* **85**(19), 4120 (2000).

[59] M. D. Groner, J. W. Elam, F. H. Fabreguette, and S. M. George, Electrical characterization of thin Al_2O_3 films grown by atomic layer deposition on silicon and various metal substrates, *Thin solid films* **413**(1–2), 186–197 (2002).

[60] G. Lucovsky, A chemical bonding model for the native oxides of the III-V compound semiconductors, *Journal of Vacuum Science & Technology* **19**, 456 (1981).

[61] K. Kimoto, Y. Matsui, T. Nabatame, T. Yasuda, T. Mizoguchi, I. Tanaka, and A. Toriumi, Coordination and interface analysis of atomic-layer-deposition Al_2O_3 on Si(001) using energy-loss near-edge structures, *Applied Physics Letters* **83**(21), 4306 (2003).

[62] B. Shin, J. R. Weber, R. D. Long, P. K. Hurley, C. G. V. de Walle, and P. C. McIntyre, Origin and passivation of fixed charge in atomic layer deposited aluminum oxide gate insulators on chemically treated InGaAs substrates, *Applied Physics Letters* **96**(15), 152908 (2010).

[63] K. Matsunaga, T. Tanaka, T. Yamamoto, and Y. Ikuhara, First-principles calculations of intrinsic defects in Al_2O_3, *Physical Review B* **68**, 085110 (2003).

[64] J. R. Weber, A. Janotti, and C. G. Van de Walle, Native defects in Al_2O_3 and their impact on III-V/Al_2O_3 metal-oxide-semiconductor-based devices, *Journal of Applied Physics* **109**(3), 033715 (2011).

[65] J. J. H. Gielis, B. Hoex, M. C. M. van de Sanden, and W. M. M. Kessels, Negative charge and charging dynamics in Al_2O_3 films on Si characterized by second-harmonic generation, *Journal of Applied Physics* **104**(7), 073701 (2008).

[66] B. Liao, R. Stangl, T. Mueller, F. Lin, C. S. Bhatia, and B. Hoex, The effect of light soaking on crystalline silicon surface passivation by atomic layer deposited Al_2O_3, *Journal of Applied Physics* **113**, 024509 (2013).

[67] V. V. Afanasev, M. Houssa, A. Stesmans, and M. M. Heyns, Electron energy barriers between (100)Si and ultrathin stacks of SiO_2, Al_2O_3, and ZrO_2 insulators, *Applied Physics Letters* **78**(20), 3073–3075 (2001).

[68] J. Robertson, Interfaces and defects of high-k oxides on silicon, *Solid-State Electronics* **49**(3), 283–293 (2005).

[69] J. Price, G. Bersuker, and P. S. Lysaght, Identification of interfacial defects in high-k gate stack films by spectroscopic ellipsometry, *Journal of Vacuum Science & Technology B* **27**(1), 310–312 (2009).

[70] Y. Schiele, G. Hahn, and B. Terheiden, Investigation of radiation damage to the Al_2O_3/Si wafer interface during electron beam evaporation by means of C-V and lifetime measurements, *Proceedings of the 26th European Photovoltaic Solar Energy Conference*, 1068–1072 (2011).

[71] A. Rothschild, B. Vermang, X. Loozen, B. OSullivan, J. John, and J. Poortmans, ALD-Al_2O_3 passivation for solar cells: Charge investigation, *Proceedings of the 25th European Photovoltaic Solar Energy Conference*, 1382–1385 (2010).

[72] G. Dingemans, R. Seguin, P. Engelhart, M. C. M. van de Sanden, and W. M. M. Kessels, Silicon surface passivation by ultrathin

Al$_2$O$_3$ films synthesized by thermal and plasma atomic layer deposition, *Physica Status Solidi – Rapid Research Letters* **4**(1), 10–12 (2010).

[73] L. Black and K. McIntosh, Modeling recombination at the Si–Al$_2$O$_3$ interface, *IEEE Journal of Photovoltaics* **3**(3), 936–943 (2013).

[74] A. G. Aberle, S. W. Glunz, A. W. Stephens, and M. A. Green, High-efficiency silicon solar cells: Si/SiO$_2$ interface parameters and their impact on device performance, *Progress in Photovoltaics: Research and Applications* **2**(4), 265–273 (1994).

[75] W. Füssel, M. Schmidt, H. Angermann, G. Mende, and H. Flietner, Defects at the Si/SiO$_2$ interface: their nature and behavior in technological processes and stress, *Nuclear Instruments and Methods in Physics Research A* **377**(2-3), 177 – 183 (1996).

[76] P. Saint-Cast, Y.-H. Heo, E. Billot, P. Olwal, M. Hofmann, J. Rentsch, S. W. Glunz, and R. Preu, Variation of the layer thickness to study the electrical property of PECVD Al$_2$O$_3$ / c-Si interface, *Energy Procedia* **8**, 642–647 (2011).

[77] R. N. Hall, Electron-hole recombination in germanium, *Physical Review* **87**(2), 387 (1952).

[78] M. J. Stocks, *High efficiency multicrystalline silicon solar cells*, PhD thesis, Australian National University (1998).

[79] S. Dauwe, L. Mittelstädt, A. Metz, and R. Hezel, Experimental evidence of parasitic shunting in silicon nitride rear surface passivated solar cells, *Progress in Photovoltaics: Research and Applications* **10**(4), 271–278 (2002).

[80] S. Steingrube, P. P. Altermatt, D. Steingrube, J. Schmidt, and R. Brendel, Interpretation of recombination at c-Si/SiN$_x$ interfaces by surface damage, *Journal of Applied Physics* **108**(1), 014506 (2010).

[81] A. Richter, S. W. Glunz, F. Werner, J. Schmidt, and A. Cuevas, Improved quantitative description of Auger recombination in crystalline silicon, *Physical Review B* **86**, 165202 (2012).

[82] L. Meitner, Über die Entstehung der β-Strahl-Spektren radioaktiver Substanzen, *Zeitschrift für Physik* **9**(1), 131–144 (1922).

[83] P. Auger, Sur les rayons β secondaires produits dans un gaz par des rayons x, *Proceedings of the Academy of Sciences* **T. 177**(3), 169–171 (1923).

[84] P. Auger, Sur l'effet photoélectrique composé, *Journal de Physique et le Radium* **6**(6), 205–208 (1925).

[85] M. S. Tyagi and R. van Overstraeten, Minority carrier recombination in heavily-doped silicon, *Solid-State Electronics* **26**, 577 (1983).

[86] J. Dziewior and W. Schmid, Auger coefficients for highly doped and highly excited silicon, *Applied Physics Letters* **31**(5), 346–348 (1977).

[87] R. A. Sinton and R. M. Swanson, Recombination in highly injected silicon, *IEEE Transactions on Electron Devices* **ED-34**(6), 1380–1389 (1987).

[88] A. Hangleiter and R. Häcker, Enhancement of band-to-band Auger recombination by electron-hole correlations, *Physical Review Letters* **65**(2), 215–218 (1990).

[89] N. F. Mott, *Metal-Insulator Transitions*, Taylor & Francis, London (1974).

[90] P. P. Altermatt, J. Schmidt, G. Heiser, and A. G. Aberle, Assessment and parameterisation of Coulomb-enhanced Auger recombination coefficients in lowly injected crystalline silicon, *Journal of Applied Physics* **82**(10), 4938–4944 (1997).

[91] H. Schlangenotto, H. Maeder, and W. Gerlach, Temperature dependence of the radiative recombination coefficient in silicon, *Physica Status Solidi (a)* **21**(1), 357–367 (1974).

[92] T. Trupke, M. A. Green, P. Würfel, P. P. Altermatt, A. Wang, J. Zhao, and R. Corkish, Temperature dependence of the radiative recombination coefficient of intrinsic crystalline silicon, *Journal of Applied Physics* **94**(8), 4930–4937 (2003).

[93] J. Benick, A. Richter, M. Hermle, and S. W. Glunz, Thermal stability of the Al_2O_3 passivation on p-type silicon surfaces for solar cell applications, *Physica Status Solidi – Rapid Research Letters* **3**(7–8), 233–235 (2009).

[94] D. Suwito, T. Roth, D. Pysch, L. Korte, A. Richter, S. Janz, and S. W. Glunz, Detailed study of the passivation mechanism of a-Si_xC_{1-x} for the solar cell rear side, *Proceedings of the 23rd European Photovoltaic Solar Energy Conference* (2008).

[95] T. Lüder, G. Hahn, and B. Terheiden, Passivation of Si wafers by ALD-Al_2O_3 films with different surface conditioning, *Energy Procedia* **8**, 660–665 (2011).

[96] A. Richter, F. M. M. Souren, D. Schuldis, R. M. W. Görtzen, J. Benick, M. Hermle, and S. W. Glunz, Thermal stability of spatial ALD deposited Al_2O_3 capped by PECVD SiN_x for the passivation of lowly- and highly-doped *p*-type silicon surfaces, *Proceedings of the 27th European Photovoltaic Solar Energy Conference*, 1133–1137 (2012).

[97] D. B. M. Klaassen, A unified mobility model for device simulation–i. model equations and concentration dependence, *Solid-State Electronics* **35**(7), 953–959 (1992).

[98] T. F. Ciszek and T. H. Wang, Silicon defect and impurity studies using controlled samples, *Proceedings of the 14th European Photovoltaic Solar Energy Conference*, 396–399 (1997).

[99] T. Trupke, R. Bardos, F. Hudert, P. Würfel, J. Zhao, A. Wang, and M. Green, Effective excess carrier lifetimes exceeding 100 milliseconds in float zone silicon determined from photoluminescence, *Proceedings of the 19th European Photovoltaic Solar Energy Conference*, 758–761 (2004).

[100] E. Yablonovitch, D. L. Allara, C. C. Chang, T. Gmitter, and T. B. Bright, Unusually low surface-recombination velocity on silicon and germanium surfaces, *Physical Review Letters* **57**(2), 249–252 (1986).

[101] J. del Alamo, S. Swirhun, and R. M. Swanson, Simultaneous measurement of hole lifetime, hole mobility, and bandgap narrowing in heavily doped *n*-type silicon, *Technical Digest for the International Electron Devices Meeting* **85**, 290–293 (1985).

[102] R. Häcker and A. Hangleiter, Intrinsic upper limits of the carrier lifetime in silicon, *Journal of Applied Physics* **75**(11), 7570–7572 (1994).

[103] M. J. Kerr and A. Cuevas, Very low bulk and surface recombination in oxidized silicon wafers, *Semiconductor Science and Technology* **17**(1), 35 (2002).

[104] P. P. Altermatt, F. Geelhaar, T. Trupke, X. Dai, A. Neisser, and E. Daub, Injection dependence of spontaneous radiative recombination in c-Si: experiment, theoretical analysis, and simulation, *Proc. 5th International Conference on Numerical Simulation of Optoelectronic Devices*, 47–48 (2005).

[105] A. Schenk, Finite-temperature full random-phase approximation model of band gap narrowing for silicon device simulation, *Journal of Applied Physics* **84**(7), 3684 (1998).

[106] K. Misiakos and D. Tsamakis, Accurate measurement of the silicon intrinsic carrier density from 78 to 340 K, *Journal of Applied Physics* **74**(5), 3293 (1993).

[107] P. P. Altermatt, F. Geelhaar, T. Trupke, X. Dai, A. Neisser, and E. Daub, Injection dependence of spontaneous radiative recombination in crystalline silicon: Experimental verification and theoretical analysis, *Applied Physics Letters* **88**(26), 261901 (2006).

[108] S. W. Glunz, D. Biro, S. Rein, and W. Warta, Field-effect passivation of the SiO_2–Si interface, *Journal of Applied Physics* **86**(1), 683–691 (1999).

[109] Synopsys, *Sentaurus Device User Guide*, Version F-2011.09.

[110] R. B. Godfrey and M. A. Green, High-efficiency silicon minMIS solar cells – Design and experimental results, *IEEE Transactions on Electron Devices* **27**(4), 737–745 (1980).

[111] R. Hezel, Recent progress in MIS solar cells, *Progress in Photovoltaics: Research and Applications* **5**(2), 109–120 (1997).

[112] B. Kuhlmann, A. G. Aberle, R. Hezel, and G. Heiser, Simulation and optimization of metal-insulator-semiconductor inversion-layer silicon solar cells, *IEEE Transactions on Electron Devices* **47**(11), 2167 – 2178 (2000).

[113] I. G. Martin, R. Lövblom, and R. Alcubilla, High-efficiency solar cells based on inversion layer emitters, *Proceedings of the 24th European Photovoltaic Solar Energy Conference*, 1985–1991 (2009).

[114] M. Colina, I. Martin, C. Voz, A. Morales-Vilches, P. Ortega, G. Lopez, A. Orpella, R. Alcubilla, I. Sanchez-Aniorte, and C. Molpeceres, Optimization of laser doping processes for the creation of p^+ regions from solid dopant sources, *Proceedings of the 27th European Photovoltaic Solar Energy Conference*, 1885–1889 (2012).

[115] P. Ortega, I. Martin, G. Lopez, M. Colina, A. Orpella, C. Voz, and R. Alcubilla, p-type c-Si solar cells based on rear side laser processing of Al_2O_3/SiC_x stacks, *Solar Energy Materials & Solar Cells* **106**, 80–83 (2012).

[116] N.-P. Harder, Y. Larionova, and R. Brendel, Al^+-doping of Si by laser ablation of Al_2O_3/SiN passivation, *Physica Status Solidi A* **210**(9), 1871–1873 (2013).

[117] R. Sidhu, M. Bennett, J. Zahler, and D. Carlson, Direct measurement of induced inversion layer sheet resistance by transmission line method, *Proceedings of the 37th IEEE Photovoltaic Specialists Conference*, 002937–002939 (2011).

[118] D. Zielke, J. H. Petermann, F. Werner, B. Veith, R. Brendel, and J. Schmidt, Contact passivation in silicon solar cells using atomic-layer-deposited aluminum oxide layers, *Physica Status Solidi – Rapid Research Letters* **5**(8), 298–300 (2011).

[119] M. A. Green, *Solar cells*, University of New South Wales, Kensington (1992).

[120] B. Kuhlmann, *Charakterisierung und mehrdimensionale Simulation von MIS-Inversionsschichtsolarzellen*, PhD thesis, Leibniz Universität Hannover (1998).

[121] Sentaurus Device, available from http://www.synopsys.com/Tools/TCAD, Synopsys Inc., Mountain View, CA., ().

[122] V. M. Agostinelli, H. Shin, and A. F. Tasch, A comprehensive model for inversion layer hole mobility for simulation of submicrometer MOSFET's, *IEEE Transaction on Electron Devices* **38**(1), 151–159 (1991).

[123] J. T. Watt and J. D. Plummer, Universal mobility-field curves for electrons and holes in MOS inversion layers, *Symposium on VLSI Technology, Digest of Technical Papers*, 81–82 (1987).

[124] P. Altermatt, H. Plagwitz, R. Bock, J. Schmidt, R. Brendel, M. Kerr, and A. Cuevas, The surface recombination velocity at boron-doped emitters: Comparison between various passivation techniques, *Proceedings of the 21st European Photovoltaic Solar Energy Conference*, 647–650 (2006).

[125] D. E. Kane and R. M. Swanson, Measurement of the emitter saturation current by a contactless photoconductivity decay method, *Proceedings of the 18th IEEE Photovoltaic Specialists Conference* (1985).

[126] R. Sinton, A. Cuevas, and M. Stuckings, Quasi-steady-state photoconductance, a new method for solar cell material and device characterization, *Proceedings of the 25th IEEE Photovoltaic Specialists Conference*, p. 457 (1996).

[127] A. Cuevas, P. A. Basore, G. Giroult-Matlakowski, and C. Dubois, Surface recombination velocity of higly doped *n*-type silicon, *Journal of Applied Physics* **80**(6), 3370 (1996).

[128] R. R. King and R. M. Swanson, Studies of diffused boron emitters: Saturation current, bandgap narrowing, and surface recombination velocity, *IEEE Transactions on Electron Devices* **38**(6), 1399 (1991).

[129] A. Cuevas, M. Stuckings, J. Lau, and M. Petravic, The recombination velocity of boron diffused surfaces, *Proceedings of the 14th European Photovoltaic Solar Energy Conference*, p. 2416 (1997).

[130] M. Wolf and H. Rauschenbach, Series resistance effects on solar cell measurements, *Advanced Energy Conversion* **3**, 455–479 (1963).

[131] A. S. Erickson, N. K. Kedem, A. E. Haj-Yahia, and D. Cahen, Aluminum oxide – n-Si field effect inversion layer solar cells with organic top contact, *Applied Physics Letters* **101**, 233901 (2012).

Publications

Parts of this thesis have previously been published in several of the following publications:

Publications in refereed journals:

- F. Werner, B. Veith, V. Tiba, P. Poodt, F. Roozeboom, R. Brendel, and J. Schmidt, Very low surface recombination velocities on p- and n-type c-Si by ultrafast spatial atomic layer deposition of aluminum oxide, *Applied Physics Letters* **97**(16), 162103 (2010).

- F. Werner, B. Veith, D. Zielke, L. Kühnemund, C. Tegenkamp, M. Seibt, R. Brendel, and J. Schmidt, Electric and chemical properties of the c-Si/Al$_2$O$_3$ interface, *Journal of Applied Physics* **109**(11), 113701 (2011).

- F. Werner, A. Cosceev, and J. Schmidt, Interface recombination parameters of atomic-layer-deposited Al$_2$O$_3$ on crystalline silicon, *Journal of Applied Physics* **111**(7), 073710 (2012).

- F. Werner, Y. Larionova, D. Zielke, T. Ohrdes, and J. Schmidt, Aluminum-oxide-based inversion layer solar cells on n-type crystalline silicon: fundamental properties and efficiency potential, *Journal of Applied Physics* **115**(7), 073702 (2014).

- F. Werner and J. Schmidt, Manipulating the negative fixed charge density at the c-Si/Al$_2$O$_3$ interface, *Applied Physics Letters* **104**(9), 091604 (2014).

- S. Gatz, H. Hannebauer, R. Hesse, F. Werner, A. Schmidt, T. Dullweber, J. Schmidt, K. Bothe, and R. Brendel, 19.4 %-efficient large-area fully screen-printed silicon solar cells, *Physica Status*

Solidi – Rapid Research Letters **5**(4), 147 (2011).

- D. Zielke, J. H. Petermann, F. Werner, B. Veith, R. Brendel, and J. Schmidt, Contact passivation in silicon solar cells using atomic-layer-deposited aluminum oxide layers, *Physica Status Solidi – Rapid Research Letters* **5**(8), 298 (2011).

- P. Poodt, V. Tiba, F. Werner, J. Schmidt, A. Vermeer, and F. Roozeboom, Ultrafast atomic layer deposition of alumina layers for solar cell passivation, *Journal of the Electrochemical Society* **158**(9), H937 (2011).

- A. Richter, S. W. Glunz, F. Werner, J. Schmidt, and A. Cuevas, Improved quantitative description of Auger recombination in crystalline silicon, *Physical Review B* **86**, 165202 (2012).

- F.-J. Ma, G. G. Samudra, M. Peters, A. G. Aberle, F. Werner, J. Schmidt, and B. Hoex, Advanced modelling of the effective minority carrier lifetime of passivated crystalline silicon wafers, *Journal of Applied Physics* **112**(5), 054508 (2012).

- M. Algasinger, J. Paye, F. Werner, J. Schmidt, M. S. Brandt, M. Stutzmann, and S. Koynov, Improved black silicon for photovoltaic application, *Advanced Energy Materials* **3**(8), 1068 (2013).

- B. Veith, T. Ohrdes, F. Werner, R. Brendel, P. P. Altermatt, N.-P. Harder, and J. Schmidt, Injection dependence of the effective lifetime of n-type Si passivated by Al_2O_3: An edge effect?, *Solar Energy Materials & Solar Cells* **120**(A), 436 (2014).
  SiliconPV Award 2013

- D. Zielke, V. Titova, F. Werner, and J. Schmidt, Organic-silicon heterojunction solar cells on n-type silicon wafers: the BackPEDOT concept, *Solar Energy Materials & Solar Cells*, in press (2014).
  SiliconPV Award 2014

PUBLICATIONS IN CONFERENCE PROCEEDINGS:

- F. Werner, B. Veith, D. Zielke, L. Kühnemund, C. Tegenkamp, M. Seibt, J. Schmidt, and R. Brendel, Improved understanding of recombination at the Si/Al_2O_3 interface, *Proceedings of the 25th European Photovoltaic Solar Energy Conference*, 1121 (Valencia, Spain, 2010).

- F. Werner, W. Stals, R. Görtzen, B. Veith, R. Brendel, and J. Schmidt, High-rate atomic layer deposition of Al_2O_3 for the surface passivation of Si solar cells, *Energy Procedia* **8**, 301 (2011).

- F. Werner, A. Cosceev, and J. Schmidt, Silicon surface passivation by Al_2O_3: Recombination parameters and inversion layer solar cells, *Energy Procedia* **27**, 319 (2012).

- F. Werner, Y. Larionova, D. Zielke, T. Ohrdes, and J. Schmidt, Aluminum-oxide-based inversion layer solar cells on n-type c-Si, *Proceedings of the 28th European Photovoltaic Solar Energy Conference*, 947 (Paris, France, 2013).
  EU PVSEC Student Award 2013

- J. Schmidt, B. Veith, F. Werner, D. Zielke, and R. Brendel, Silicon surface passivation by ultrathin Al_2O_3 films and Al_2O_3/SiN_x stacks, *Proceedings of the 35th IEEE Photovoltaic Specialists Conference*, 885 (Honolulu, HI, 2010).

- J. Schmidt, F. Werner, B. Veith, D. Zielke, R. Bock, V. Tiba, P. Poodt, F. Roozeboom, A. Li, A. Cuevas, and R. Brendel, Industrially relevant Al_2O_3 deposition techniques for the surface passivation of Si solar cells, *Proceedings of the 25th European Photovoltaic Solar Energy Conference*, 1130 (Valencia, Spain, 2010).

- S. Steingrube, P. P. Altermatt, D. Zielke, F. Werner, J. Schmidt, and R. Brendel, Reduced passivation of silicon surfaces at low injection densities caused by H-induced defects, *Proceedings of the*

25th *European Photovoltaic Solar Energy Conference*, 1748 (Valencia, Spain, 2010).

- B. Veith, F. Werner, D. Zielke, R. Brendel, and J. Schmidt, Comparison of the thermal stability of single Al_2O_3 layers and Al_2O_3/SiN_x stacks for the surface passivation of silicon, *Energy Procedia* **8**, 307 (2011).

- D. Zielke, J. H. Petermann, F. Werner, B. Veith, R. Brendel, and J. Schmidt, 21.7 % efficient PERC solar cells with AlO_x tunneling layer, *Proceedings of the 26th European Photovoltaic Solar Energy Conference*, 1115 (Hamburg, Germany, 2011).

- B. Vermang, F. Werner, W. Stals, A. Lorenz, A. Rothschild, J. John, J. Poortmans, R. Mertens, R. Gortzen, F. Roozeboom, and J. Schmidt, Spatially-separated atomic layer deposition of Al_2O_3, a new option for high-throughput Si solar cell passivation, *Proceedings of the 37th IEEE Photovoltaic Specialists Conference*, 1144 (Seattle, USA, 2011).

- J. Schmidt, F. Werner, B. Veith, D. Zielke, S. Steingrube, P.P. Altermatt, S. Gatz, T. Dullweber, and R. Brendel, Advances in the surface passivation of silicon solar cells, *Energy Procedia* **15**, 30 (2012).

- A. Richter, F. Werner, A. Cuevas, J. Schmidt, and S. W. Glunz, Improved parameterization of Auger recombination in silicon, *Energy Procedia* **27**, 88 (2012).
  SiliconPV Award 2012

- B. Veith, T. Dullweber, M. Siebert, C. Kranz, F. Werner, N.-P. Harder, J. Schmidt, B.F.P. Roos, T. Dippell, and R. Brendel, Comparison of ICP-AlO_x and ALD-Al_2O_3 layers for the rear surface passivation of c-Si solar cells, *Energy Procedia* **27**, 379 (2012).

Poster:

- F. Werner, B. Veith, D. Zielke, L. Kühnemund, C. Tegenkamp, M. Seibt, J. Schmidt, and R. Brendel, Atomic layer deposition of Al_2O_3 for the surface passivation of Si solar cells, presented at the LNQE NanoDay 2010 (Hanover, Germany, 2010).
  NanoDay 2010 Poster Award

Other publications:

- F. Werner, B. Veith, and J. Schmidt, Homogeneous surface: Recombination at the c-Si/Al_2O_3 interface, *Photovoltaic Production* **4**, 48 (2011).

- J. Schmidt, F. Werner, B. Veith, D. Zielke, R. Bock, R. Brendel, V. Tiba, P. Poodt, F. Roozeboom, A. Li, and A. Cuevas, Surface passivation of silicon solar cells using industrially relevant Al_2O_3 deposition techniques, *Photovoltaics International* **10**, 52 (2010).

Acknowledgments
Danksagung

Curriculum Vitae

Name:	Dipl.-Phys. Florian Werner
Date of birth:	27.02.1983
Place of birth:	Konstanz, Germany
Family status:	married to Elena Werner, daughter Diana Werner

1989 – 1993	Elementary school, Grundschule Allensbach.
1993 – 2002	Secondary school, Heinrich-Suso-Gymnasium Konstanz.
25.05.2002	General qualification for university entrance (Abitur).
2002 – 2003	Civil service as medical technician at the Klinikum Konstanz.
2003 – 2009	Studies in physics, Georg-August-Universität Göttingen.
21.10.2005	Intermediate examination (Vordiplom).
2007	Summer school at the European Organization for Nuclear Research (CERN) in Geneva, Switzerland.
2007 – 2008	Research semester with Prof. Dr. Hideo Ohno at Tohoku University in Sendai, Japan "Gate control of nuclear spin coherence in GaAs quantum wells".
2008 – 2009	Diplom thesis with Prof. Dr. Angela Rizzi at the Institute for Semiconductor Physics, Georg-August-Universität Göttingen "Electrical characterization of single InN nanowires".
23.07.2009	University degree in physics (Diplom).
2009 – 2014	Research associate and doctoral candidate with Prof. Dr. Jan Schmidt at the Institute for Solar Energy Research Hamelin (ISFH).